Design of Offshore Wind Turbine Support Structures: Selected topics in the field of geotechnical engineering

Bakmar, Christian LeBlanc

Publication date:
2009

Document Version
Publisher's PDF, also known as Version of record

Design of Offshore Wind Turbine Support Structures

Selected topics in the field of geotechnical engineering

Christian LeBlanc
M.Sc. (Civil Engineering)
Technical University of Denmark, 2004

A thesis submitted in partial fulfilment of the requirements for the degree of

Doctor of Philosophy

in Civil Engineering at the Department of Civil Engineering, Aalborg University, Denmark, and the Industrial Ph.D. Fellowship Programme Certificate, Ministry of Science, Technology and Innovation, Denmark

2009

Ministry of Science
Technology and Innovation

AALBORG UNIVERSITY

ISSN 1901-7294
DCE Thesis No. 18

Title of the Ph.D. thesis
Design of Offshore Wind Turbine Support Structures - Selected topics in the field of geotechnical engineering

Legal name
Christian LeBlanc Bakmar (“Bakmar” is omitted in publications)

Project duration
1st December 2005 – 1st December 2008

Supervisors
Principal supervisor
Dr. Lars Bo Ibsen, Professor
Department of Civil Engineering
Aalborg University
Aalborg, Denmark

Co-supervisor
Dr. Ole Hededal, Associate Professor
Department of Civil Engineering
Technical University of Denmark
Kgs. Lyngby, Denmark

Co-supervisor
Dr. Morten Liingaard, Geotechnical Engineer
Department of Offshore Technology
DONG Energy
Copenhagen, Denmark

Assessment committee members
Dr. Martin Achmus, Professor
Institute of Soil Mechanics
Leibniz Universität Hannover
Hannover, Germany

Dr. Tove Feld, Director
DNV Wind Energy
Det Norske Veritas
Hellerup, Denmark

Dr. Peter Frigaard, Head of Department
Department of Civil Engineering
Aalborg University
Aalborg, Denmark

Published by
Department of Civil Engineering, Faculty of Engineering, Aalborg University
Sohngårdsholmsvej 57, DK-9000 Aalborg, Denmark
Telephone +45 99 40 99 40, Fax +45 98 14 25 55 / +45 98 14 82 43, E-mail: civil@civil.aau.dk

Printed by
Aalborg University, DK-9000 Aalborg, Denmark

ISSN
1901-7294 (DCE Thesis No. 18)

Dedicated to the memory of my mother,

Marie Jeannette Berthe LeBlanc

TABLE OF CONTENTS

PREFACE

The present Ph.D. research project was initiated in summer 2005 by the former Danish energy company, Energy E2, where I held a position as a developer of offshore wind farms. DONG Energy was established in July 2006 as a result of the merger of six Danish energy companies, including Energy E2. Today, DONG Energy is a major player in the sector of offshore wind energy, operating 50% of all offshore wind farms worldwide.

I was granted a fellowship for my Ph.D. studies under the Industrial Ph.D. Fellowship Programme of the Ministry of Science, Technology and Innovation, Denmark in December 2005. The financial support for my Ph.D. studies was provided by DONG Energy and the Ministry of Science, Technology and Innovation.

For the duration of my Ph.D. studies, my primary location was DONG Energy in Copenhagen, with stays at different universities. As a staff member of the Department of Offshore Technology, DONG Energy, I got a deep insight in the development of the emerging offshore wind energy sector and, more importantly, in the challenging engineering problems faced by the industry. DONG Energy has formed the core of the offshore wind energy sector, which is evolving rapidly; new problems arise and others become less important. Therefore, there were shifts in the formulation of my Ph.D. project several times, to ensure that the research work was focused on the most important and pressing issues.

The major part of the Ph.D. project was carried out in cooperation with the Department of Civil Engineering, Aalborg University, Denmark, under the supervision of Dr. Lars Bo Ibsen. Dr. Ibsen has vast experience in the field of offshore wind energy due to his enthusiastic engagement in the development of the bucket foundation as a novel support structure for offshore wind turbines. I spent much of my time at Aalborg University during the first year of my Ph.D. studies. Here, I met Dr. Morten Liingaard who was completing his Ph.D. project. Dr. Liingaard was later employed by DONG Energy and became my co-supervisor.

Dr. Ole Hededal, Department of Civil Engineering, Technical University of Denmark, was co-supervisor of my Ph.D. studies. During the first two years of my studies, we frequently met to discuss issues relating to numerical modelling; a technical field in which Dr. Hededal has large insight and experience.

During the second year of my Ph.D. studies, I spent several months at the Department of Civil Engineering, University of Oxford, United Kingdom, under the supervision of Dr. Guy T. Houlsby and Dr. Byron W. Byrne. Arriving in Oxford, I brought the knowledge of the issues faced by the industry, but intentionally, no pre-defined scope of work. This was a successful strategy, as it later became evident that experimental equipment, well-suited for investigation of important issues relating to the long-term behaviour of monopiles, was available at the university. I resided at Keble College, which allowed me to have the optimal environment to concentrate on my research work. In the third year of my Ph.D. studies, I returned to the University of Oxford, residing at Balliol College. I continued research work on the issues relating to long-term behaviour of monopiles.

After my first stay at the University of Oxford, I spent three months at the Centre for Offshore Foundation Systems (COFS), University of Western Australia, Perth, Australia, under the supervision of Dr. Mark Randolph. COFS is a world leading research institution within the design of offshore foundation structures. At COFS, my work concentrated on a concrete and limited problem within one of the technical fields in which Dr. Randolph has a strong expertise.

During my Ph.D. studies, I undertook course work at the Technical University of Denmark, Denmark; Delft GeoAcademy of Deltares, Netherlands; Building Research Establishment, United Kingdom, and Norwegian University of Science and Technology, Norway.

Christian LeBlanc
Copenhagen, 2009

Successful installation of the first monopod bucket foundation offshore in Denmark

First and second from the right: Lars Bo Ibsen and Christian LeBlanc

ACKNOWLEDGEMENTS

I am indebted to many people; supervisors, sponsors, friends and family members for their interest, assistance and support, and therefore, I wish to acknowledge and thank them.

I will like to express my gratitude to DONG Energy, especially Dr. Lars Storm Pedersen, Director, for believing in me and making this research project possible. I also wish to acknowledge the financial support of the Ministry of Science, Technology and Innovation, Denmark. I wish to thank Mr. Kim Ahle, Head of Department of Offshore Technology, DONG Energy, for supporting me and providing an excellent working environment. Special thanks are directed to Dr. Morten Liingaard, Department of Offshore Technology, DONG Energy, for his assistance and advice as my co-supervisor and friend.

I wish to express my appreciation to my supervisor, Dr. Lars Bo Ibsen, Professor, Department of Civil Engineering, Aalborg University, Denmark, who guided and supported me during the course of my studies. I wish to acknowledge my co-supervisor, Dr. Ole Hededal, Associate Professor, Department of Civil Engineering, Technical University of Denmark, for his assistance and enlightening discussions.

The times I spent at the University of Oxford, United Kingdom have been truly inspiring and rewarding. I wish to express my gratitude to Dr. Guy T. Houlsby, Professor and Head, Department of Civil Engineering, for his generous assistance, valuable suggestions and supervision. I am very thankful to Dr. Byron W. Byrne, University Lecturer, Department of Civil Engineering, University of Oxford, for his thorough guidance, helpfulness and great commitment to my research.

I wish to express my appreciation for Dr. Mark Randolph, Professor and Head, Centre for Offshore Foundations Systems, University of Western Australia, for his extensive insight and constructive advice during the time I spent at the University of Western Australia.

I wish to express my deepest gratitude to Dr. Shakuntala Haraksingh Thilsted, my mother-in-law (to be). Throughout my Ph.D. studies, Shakuntala has given me valuable guidance concerning the planning and structure of my work and has meticulously corrected my English. For this, I am very grateful.

Most of all, I wish to thank you, Sita, my wonderful fiancée, for your indispensable love, patience, encouragement, and for always supporting me.

ORGANISATION OF THE PH.D. THESIS

This Ph.D. thesis includes five scientific papers, originating from the Ph.D. research project; three are submitted for publication in scientific journals, one is published in the proceedings of an international conference, and one is published as a DCE technical memorandum of the Department of Civil Engineering, Aalborg University, Denmark. The introductory chapters of this thesis include background information of the offshore wind energy sector, the overall aim and specific objectives of the research project as well as a presentation of the selected topics of the research project. In addition, the conclusions and recommendations for future research in relation to the topics presented and discussed in the five scientific papers are included. A list of literature cited in the chapters is given, as well as references in each scientific paper.

LIST OF SCIENTIFIC PAPERS

Paper I

LeBlanc, C., Houlsby, G. T. & Byrne, B. W. *Response of stiff piles in sand to long-term cyclic lateral loading.* Geotechniqué, October 2008. Accepted.

Paper II

LeBlanc, C., Byrne, B. W. & Houlsby, G. T. *Response of stiff piles to random two-way lateral loading.* Submitted for publication.

Paper III

LeBlanc, C., Hededal, O. & Ibsen, L. B. *A modified critical state plasticity model for sands - theory and implementation.* Dept. of Civil Engineering, Aalborg University, Aalborg, DCE Technical Memorandum No. 8, 2008.

Paper IV

LeBlanc, C. & Randolph, M. F. *Interpretation of piezocones in silt, using cavity expansion and critical state methods.* Proceedings of the 12th International Conference of International Association for Computer Methods and Advances in Geomechanics (IACMAG), 1st - 6th October 2008, Goa, India. 822-829.

Paper V

LeBlanc, C., Ibsen, L. B. & Liingaard, M. *Buckling of large diameter bucket foundations during installation in sand.* Submitted for publication.

SUMMARY IN ENGLISH

Breaking the dependence on fossil fuels offers many opportunities for strengthened competitiveness, technological development and progress. Offshore wind power is a domestic, sustainable and largely untapped energy resource that provides an alternative to fossil fuels, reduces carbon emissions, and decreases the economic and supply risks associated with reliance on imported fuels. Today, the modern offshore wind turbine offers competitive production prices for renewable energy and is therefore a key technology in achieving the energy and climate goals of the future.

The overall aim of this Ph.D. thesis was to enable low-cost and low-risk support structures to be designed in order to improve the economic feasibility of future offshore wind farms. The research work was divided in the following four selected research topics in the field of geotechnical engineering, relating to the monopile and the bucket foundation concepts:

1. **Long-term response of monopiles:** Offshore wind turbine support structures are subjected to strong cyclic loading, originating from wind and wave loads. This can lead to accumulated rotation of the wind turbine tower, adversely affecting the ultimate strength and fatigue life of the wind turbine, including the support structure, machine components and blades. Thus, a safe design must address issues of accumulated rotation and changes in stiffness. Design guidance on this issue is limited.

   The aim of the research work was to improve the current design guidelines for prediction of the accumulated rotation of an offshore wind turbine in response to cyclic loading. A novel engineering methodology, capable of incorporating effects of continuous or random two-way cyclic loading on the response of monopiles in a simple manner, is presented. The validity of the model is supported by 1-g laboratory tests in which a stiff pile, installed in drained sand, was subjected to series of 10-10000 load cycles with varying amplitude and mean load. A complete non-dimensional framework for stiff piles in sand is presented and applied to interpret the test results. The accumulated rotation was found to be dependent on relative density and was strongly affected by the characteristics of the applied cyclic load. The results indicate that accumulated pile rotation during the life of the turbine is dominated by the worst expected load.

2. **Modelling of advanced geotechnical problems:** Numerical methods, such as finite element of finite difference, provide an important tool for investigating soil-structure interaction and optimizing the design of support structures. However, advanced three-dimensional constitutive models, not readily available, are required to accurately capture the response of soils, in particular, the response to cyclic loading.

   The aim of the research work was to develop a practical engineering tool for exploring the responses of offshore support structures subjected to cyclic loading, in order to benchmark and improve design guidelines and address risks of failure due cyclic liquefaction/mobility. An advanced constitutive model, based on a former model, capable of simulating the response of soils, in particular, the response to cyclic loading and related observations, such as accumulation of pore pressure, cyclic mobility and cyclic liquefaction, is presented. The model was implemented as a user-subroutine in a commercial finite difference code using an integration scheme based on the general return mapping method. A suitable implementation strategy was developed to ensure robustness and address convergence problems. The model was proven capable of accurately simulating triaxial test data of silt sediments from the North Sea.

3. **Interpretation of piezocones in silt:** Piezocone data give important information on the soil parameters required for the design of offshore wind turbine support structures. However, interpretation of piezocone data in silt sediments is conceptually difficult, as the measured response is affected by the degree of pore pressure dissipation during cone penetration. This is particularly problematic if the soil parameters determined from the piezocone data differ significantly from those obtained by investigating intact samples in a triaxial apparatus.

   The aim of the research work was to establish a methodology for interpreting piezocone data in silt sediments. A numerical methodology for generating a site-specific correlation between triaxial test data and the *in-situ* state of silt sediments is presented. The process of cone penetration was simulated as an expanding cylindrical cavity using a plasticity model formulated within the framework of critical state soil mechanics, while accounting for effects of drainage conditions in saturated soil. The method was successfully applied in a case study of silt sediments originating from the North Sea. The results readily explained the low cone tip resistance measured in silt

sediments; a derived effect of the silt having a large slope of the critical state line, resulting in rather weak and compressible behaviour at high mean effective stresses.

4. **Buckling loads of bucket foundations:** Bucket foundations have the potential to be the cost-effective option for future offshore wind farms, if suction assisted penetration is employed. The geometry of bucket foundations falls into the category of thin shell structures as the ratio between the bucket diameter and wall thickness is very large. Therefore, the structure is particularly exposed to structural buckling due predominantly to the hydrostatic loading during installation.

   The aim of the research work was to reduce the risk of buckling failure during installation of future bucket foundations. Guidelines and recommendations for design of bucket foundations against structural buckling were derived. These were supported by series of three-dimensional, non-linear finite element analyses, while accounting for material plasticity, geometric imperfections, residual stresses, embedment depth and derived effects of adding suction, such as the presence of hydraulic gradients in the soil. Furthermore, observations of a full-scale bucket foundation, which failed due to buckling, confirmed the numerical findings. The results and conclusions presented were used to design the first bucket foundation, the Mobile Met Mast, which was successfully installed offshore in Denmark, in February 2009.

The outcomes of each of the four research topics contribute, either directly or indirectly, to enable low-cost and low-risk support structures to be put into use. Overall, these outcomes are an important contribution to increase the economic feasibility of future offshore wind farms.

SUMMARY IN DANISH (SAMMENDRAG)

Ved at bryde afhængigheden af fossile brændstoffer skabes der mange muligheder for at styrke konkurrenceevnen, den teknologiske udvikling og fremskridtet. Havvindmølleenergi er en lokal, bæredygtig og stort set uudnyttet energikilde, som udgør et alternativ til fossile brændstoffer. Det er en vedvarende energiform, som bidrager til at reducere udledningen af drivhusgasser og til at minimere de økonomiske og forsyningsmæssige risici forbundet med afhængigheden af importerede fossile brændstoffer. I dag leverer den moderne havvindmølle vedvarende energi til konkurrence-dygtige produktionspriser og er dermed en nøgleteknologi til opnåelse af fremtidens energi- og klimamål.

Det overordnede mål for forskningsarbejdet, der præsenteres i denne Ph.D.-afhandling, er at forbedre det eksisterende normgrundlag for dimensionering af havvindmøllefundamenter, direkte eller indirekte, og dermed reducere risici og omkostninger knyttet til fremtidens fundamenter. Forskningsarbejdet er opdelt i fire forskningsemner, udvalgt indenfor det geotekniske fagområde, som relaterer til monopæl- eller bøttefundamentet:

1. **Langtids deformationer af monopælfundamenter:** Havvindmøllefundamenter er udsat for stærke cykliske påvirkninger fra vind- og bølger. Påvirkningerne kan medføre en blivende deformation (hældning) af vindmølletårnet. Dette har en negativ effekt på vindmøllens udmattelsesstyrke og holdbarhed, herunder fundamentet, maskin-komponenterne og møllevingerne. Et forsvarligt design må derfor tage højde for blivende deformationer og stivhedsændringer, men normgrundlaget indenfor dette område er meget begrænset.

   Formålet med forskningsarbejdet er at forbedre det eksisterende normgrundlag for bestemmelse af havvindmøllers blivende deformationer, som følge af cykliske belastninger. En ny beregningsmetode, som på en enkel måde kan bestemme en monopæls respons til vilkårlige cykliske tovejs belastninger, er udviklet. Grundlaget for metoden er understøttet af laboratorietests (1-g) udført ved brug af en stiv pæl nedrammet i drænet sand. Denne blev påsat belastningsserier af 10-10000 cyklusser af varierende amplitude og middelbelastning. Regningsmæssige størrelser for monopæle i sand er præsenteret og anvendt til at tolke testresultaterne. Resultaterne viste at blivende deformationer afhænger af sandets relative densitet, og at deformationerne er stærkt påvirket af karakteristikken af den påførte cykliske belastning. Resultaterne

indikerer desuden, at de blivende deformationer, som opstår i løbet af havvindmøllers levetid, er domineret af de højst forventede belastninger.

2. **Modellering af avancerede geotekniske problemer:** Numeriske metoder, så som ”finite element” og ”finite difference”, er vigtige værktøjer for at kunne analysere jord-struktur interaktion og dermed for at kunne optimere dimensionerne af havvindmøllefundamenter. De numeriske metoder kræver dog avancerede, tredimensionelle konstitutive modeller for præcist at simulere havbundens opførsel under cykliske belastninger . Disse avancerede modeller er ikke let tilgængelige.

   Formålet med forskningsarbejdet er at udvikle et numerisk værktøj, som kan bruges til at analysere responset af havvindmøllefundamenter under påvirkning af cykliske belastninger - et værktøj, som kan anvendes til at vurdere og forbedre eksisterende normgrundlag samt imødegå risikoen for svigt forårsaget af liquefaction/mobilitet. Der præsenteres en avanceret konstitutiv model, som er udviklet på baggrund af en tidligere model. Modellen er i stand til at simulere kornet materiale under påvirkning af cykliske belastninger samt relaterede fænomener, såsom akkumulering af poretryk og liquefaction/mobilitet. Modellen blev implementeret som en bruger-subrutine i et kommercielt finite difference program, ved brug at en integrations algoritme baseret på ”general return mapping”-metoden. En passende implementeringsstrategi er udviklet for at sikre robusthed og imødegå konvergensproblemer. Modellen er i stand til præcist at simulere triaxial-forsøg udført på siltsedimenter fra Nordsøen.

3. **Tolkning af CPTu målinger i siltsedimenter:** CPTu målinger giver vigtige oplysninger om de jordparametre, som er nødvendige for dimensionering af havvindmøllefundamenter. Dog er tolkning af CPTu målinger i siltsedimenter konceptuelt vanskeligt, da målingerne er påvirket af graden af poretryksdissipation. Dette er især problematisk, såfremt parametrene bestemt på baggrund af CPTu målingerne afviger væsentligt fra dem, der er bestemt på baggrund af triaxial-forsøg på intakte prøver.

   Målet for forskningsarbejdet er at etablere en metodik til at tolke CPTu målinger i siltsedimenter. En numerisk metode blev udviklet til at generere stedspecifikke korrelationer, mellem triaxial-forsøgs data og *in-situ* tilstanden af siltsedimenter. CPTu penetrations-processen blev simuleret som et ekspanderende cylindrisk hulrum under

hensyntagen til drænforhold. Siltens materialeegenskaber blev simuleret ved brug af en plasticitetsmodel baseret på CSSM (Critical state soil mechanics). Den udviklede metode blev med succes anvendt i et casestudie baseret på siltsedimenter fra Nordsøen og var i stand til at forklare den lave spidsmodstand målt i siltsedimenterne – dette var en følge af en stejl hældning af critical state linjen, hvilket resulterede i en svag og kompressibel opførsel ved høje effektive spændinger.

4. **Pladefoldning af bøttefundamenters:** Bøttefundamentet har potentiale til at blive en konkurrencedygtig fundamentsløsning til fremtidige havvindmølleparker, såfremt bøttefundamentet kan installeres vha. nedsugning. Et bøttefundament klassificeres som en tynd skalkonstruktion, da forholdet mellem bøttediameteren og vægtykkelsen er meget stor. Konstruktionen er derfor særligt udsat overfor pladefoldning - primært på grund af de hydrostatiske laster under installationen.

   Formålet med forskningsarbejdet er at reducere risikoen for svigt pga. pladefoldning under installation af fremtidige bøttefundamenter. Vejledning, i at dimensionere bøttefundamenter mod pladefoldning, er udviklet på baggrund af tredimensionelle, ikke-lineære finite element analyser. I analyserne blev der taget højde for materialeplasticitet, geometriske ujævnheder, residual spændinger, penetrationsdybde og afledte effekter af påsat sug, såsom hydrauliske gradienter i jorden. Observationer af et fuldskala bøttefundament, som svigtede grundet pladefoldning, bekræfter de udledte konklusioner. Resultaterne og konklusionerne er anvendt til at designe ”Mobile Met Mast” - det første bøttefundament som er installeret på havet med succes. Bøttefundamentet blev installeret ud for den danske kyst i februar 2009.

Resultaterne af hvert af de fire forskningsemner bidrager, enten direkte eller indirekte, til at fundamenter med lavere omkostninger og risici kan tages i brug. På et overordnet plan udgør resultaterne et vigtigt bidrag til at gøre fremtidens havvindmølleparker mere økonomisk attraktive.

1. GENERAL INTRODUCTION

The world is now aware that the problems due to the dependence on oil and increasing carbon emissions must be solved. Breaking the dependence on fossil fuels offers many opportunities for strengthened competitiveness, technological development and progress. Offshore wind power is a domestic, sustainable and largely untapped energy resource that provides an alternative to fossil fuels, helps reduce carbon emissions, and decreases the economic and supply risks associated with reliance on imported fuels. Today, the modern offshore wind turbine offers competitive production prices for renewable energy and is therefore a key technology in achieving the energy and climate goals of the future. Therefore, there are strong political and industrial forces, especially in northern Europe, which support the development of the offshore wind industry. Offshore wind energy has a promising future globally, as the population centres throughout the world are located near or along coastlines, close to offshore wind resources.

1.1 Offshore wind farms

For years, Denmark has been the pioneer in offshore wind power. In 2002, the first large-scale offshore wind farm was installed in Denmark, and in 2008, Denmark generated more than 20% of its electricity using wind turbines (Fig. 1). Currently, there are political strategies to enlarge the Danish offshore wind energy sector in order to limit the dependence on oil, gas and coal by 2050. In the United Kingdom, several offshore wind farms have recently been installed and the government has unveiled plans to generate a large amount of offshore wind energy, 33 GW, by 2020. Other countries investing in offshore wind energy include Belgium, Germany, Ireland, Netherlands and Sweden.

Presently, the majority of wind turbines are located onshore, as the construction costs onshore are lower than offshore. However, limitations of suitable locations on land due to dense populations and existing built-up areas enforce the development of offshore wind farms. The efficiency of wind turbines has increased significantly during the past decades as wind turbines became bigger. However, for onshore wind turbines, it may be difficult to achieve further increases of efficiency, as the size of the wind turbines is close to the limit for logistic problems during transportation of large wind turbine components, such as tower sections,

Fig. 1. Nysted Offshore Wind Farm, erected in 2003.

nacelles, and blades. These limitations do not exist for transporting offshore wind turbines, as ships and barges easily accommodate large structures.

The offshore wind energy industry has not developed as rapidly as was expected a few years ago, despite strong political and industrial forces. An important factor for this is the high cost of the offshore wind turbine support structures, about 25-30% of the total cost of an offshore wind farm. Depending on the type of the turbine and location, a single support structure can cost EUR 1-4 million. New, innovative, low-cost and low-risk concepts need to be developed in order to increase the economic feasibility of future offshore wind farms.

Several concepts for offshore wind turbines support structures exist. Each concept has its advantages and limitations, and the cost-effectiveness of a particular support structure type depends to a large extent on the site conditions. Geotechnical site conditions and water depth are the primary design drivers. Transportation, logistics and installation are also important design drivers as costs of these components can be higher than the manufacture cost. Furthermore, elimination of underwater maintenance is essential due to the difficult access and high cost involved with operations offshore.

Future offshore wind farms will be located in more exposed sites, with deeper water and larger waves. In order to develop cost-effective support structures, concepts which result in

minimum offshore work and low-cost manufacturing must be put into use. Due to the variety of soil conditions, ranging from soft clays to very dense sands, and the variety of weather windows available for installation vessels, cost-effective support structures will not rely on a single concept; various concepts must be put into use to cover the wide range of site conditions.

The research work presented in this Ph.D. thesis addresses selected research topics in the field of geotechnical engineering, focusing on improving the design of future offshore wind turbine support structures. The outcomes of the research work may directly or indirectly increase the economic feasibility of future offshore wind farms by reducing risks and costs associated with offshore wind turbine support structures. This chapter gives a broad introduction to the engineering aspects of designing offshore wind turbines, an outline of the current state-of-the-art support structures concepts, as well as the challenges faced in making future support structures more cost-effective.

1.2 Loads in the offshore environment

There is much experience in designing offshore support structures within the oil and gas sector. These structures are large and unique, and are built "fit for purpose" with respect to their particular sites. The loading of oil and gas installations is often dominated by the huge self-weight. The structures are therefore less exposed to dynamic excitation. The loading of an offshore wind turbine is principally different. It is characteristic for an offshore wind turbine that the support structure is subjected to large moments at seabed and strong cyclic loading, originating from wind and wave loads on the structure.

The resulting loading of a support structure is primarily governed by a large moment at seabed level while the horizontal and vertical loads are

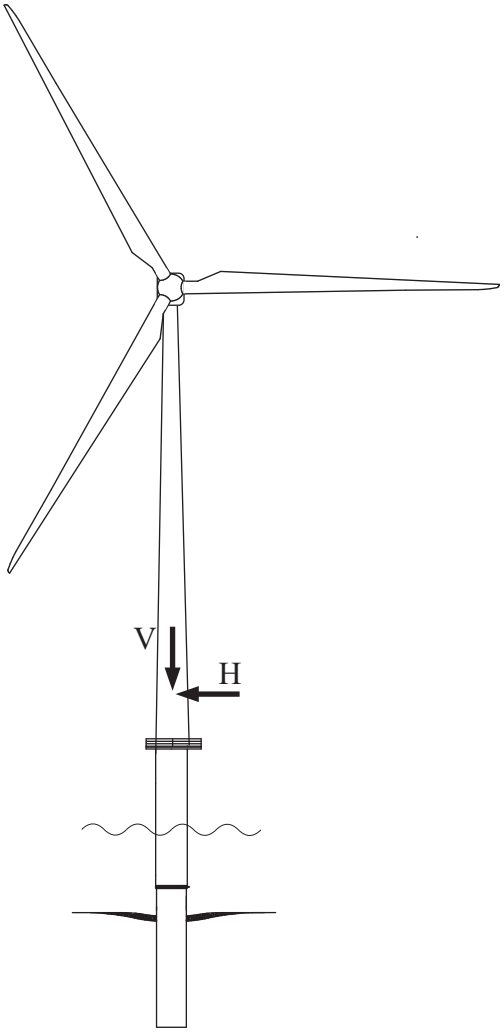

Fig. 2. Resulting loads on an offshore wind turbine.

comparably small. Contributions from wind and wave loading can be roughly estimated. For a modern offshore wind turbine, located in 20 m water depth, the resulting force of wind and wave can be approximated by a horizontal force H acting on the tower, approximately 30 m above seabed level. The vertical load is determined from the self-weight of the turbine, tower and foundation, V, as shown in Fig. 2.

Tidal currents and wind induced waves are very important in European coastal waters. Swells and waves travelling over long distances are less significant due to the topography of the North Sea. The frequency range of energy rich waves is typically in the range 0.05-0.5 Hz, and extreme waves typically occur in the range 0.07-0.14 Hz. Relevant wind-induced wave power spectra for engineering purposes are described by the JONSWAP (Joint European North Sea Wave Project) spectrum or the Pierson-Moskowitz spectrum.

The effective wind load exciting the wind turbine is determined by a complex interaction between the structural dynamics of the turbine and a wind field containing turbulent gusts caused by eddies in the flow. The turbulent wind field originates from atmospheric turbulence with contributions from nearby turbines disturbing the flow. The turbulent wind field is, for engineering purposes, usually modelled in two spatial dimensions, using a power spectrum in connection with a coherence function describing the spatial correlation of the turbulence. The von-Karman spectrum or the Kaimal spectrum is often applied to represent the wind power spectrum. The energy rich wind turbulence lies below 0.1 Hz.

Modern offshore wind turbines, producing power in the range 2.0-3.6 MW, are installed with either pitch regulated blades or variable rotational speed systems to enable optimization of the power production under a wide range of wind speeds. The rotational speed is typically in the range 10-20 revolutions per minute, and the first excitation frequency (1Ω), corresponding to a full revolution, in the range 0.17-0.33 Hz. In general, the 1Ω-frequency should only be lightly excited. A large excitation is likely caused by unwanted mass or aerodynamic imbalances. The blade passing frequency, 0.5-1 Hz, is denoted the 3Ω-frequency on a three-bladed wind turbine. This frequency is heavily excited, primarily due to the impulse-like excitation from blades passing the tower.

Site-specific spectral densities for wind and waves can be derived from available measured data, met-ocean databases or numerical models. The excitation ranges, 1Ω and 3Ω, and the realistic normalized power spectra representing aerodynamic and hydrodynamic excitation are illustrated in Fig. 3.

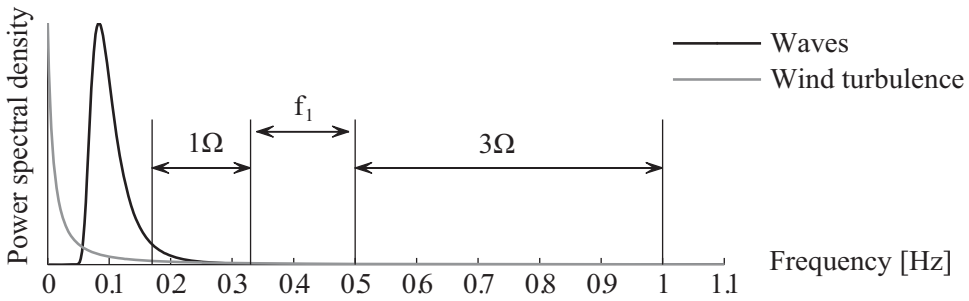

Fig. 3. Typical excitation ranges of a modern offshore wind turbine.

Today, offshore wind turbines are designed with the 1st natural frequency, f_1, in the range between 1Ω and 3Ω; in the wind industry sector this is referred to as a "soft-stiff" structure. However, it is possible to design a "soft-soft" structure with the 1st natural frequency below 1Ω, or a "stiff-stiff" structure with the 1st natural frequency above 3Ω. The choice of frequency range for f_1 sets criteria for the stiffness of the foundation; in general, less steel is required for a soft structure. Also, a softer structure requires a smaller diameter of the body which reduces the hydrodynamic loads. However, issues of fatigue or ultimate capacity may become the dominant design drivers.

The tendency to build larger turbines will continue in the future, and as turbines grow larger, the rotation frequency will decrease. Thus, the soft-soft range between 1Ω and the hydrodynamic excitation range are likely to disappear in the future. An even softer range exists below the wave excitation frequency range. If a wind turbine structure can be designed below the wave excitation frequencies, only inertia-induced responses will dominate. In the oil and gas industry, these types of structures are applied in the Mexican Gulf in deep waters (400-600 m), for example the Petronius Platform. These are referred to as "Compliant towers".

A detailed outline of the aerodynamic and hydrodynamic interaction with the structural dynamics of a wind turbine placed in an offshore environment is given by Kühn (2001).

1.3 Soil conditions

Soil at seabed consists of two components, water and solids. The solids are particles ranging in size from clay to giant boulders, depending on the geological history of the soil. The size and types of soil particles affect the properties of the soil and thus its load carrying abilities. The soil particles are arranged in a complex structure affecting water movement and erosion

resistance. A wide range of soil conditions, ranging from soft clay to boulder sand and hard rock, are found in the coastal waters of Northern Europe.

Ground investigation is the major means of obtaining soil information which affects the planning, design and construction of an offshore wind turbine project. Geotechnical site investigations are carried out before construction and typically include surface investigations (topographic surveys), and sub-surface investigations, using seismic surveys, cone penetration testing, vibrocores and boreholes. Subsequently, seabed material is thoroughly investigated in a laboratory. An important aspect of offshore construction work is geotechnical engineering - an engineering discipline that applies the principles of engineering mechanics to predict the behaviour of soil. This is a challenging task due to the wide range of soil properties and the highly non-linear behaviour exhibited by soils.

1.4 Offshore wind turbine support structures

The entire sub-structure, from below seabed level to above the splash zone, is referred to as the “support structure”. The interface to the turbine tower can be more than 20 m above mean sea level in high tide areas.

Offshore wind turbine support structures are moment resistant structures. The moment loading can be transferred to the surrounding soil using either monopod or multipod structures. Monopod structures are defined as having a single interface to the soil, whereas multipod structures have three or four interfaces. The interface between the support structure and soil can be made using piles, caissons or direct foundation.

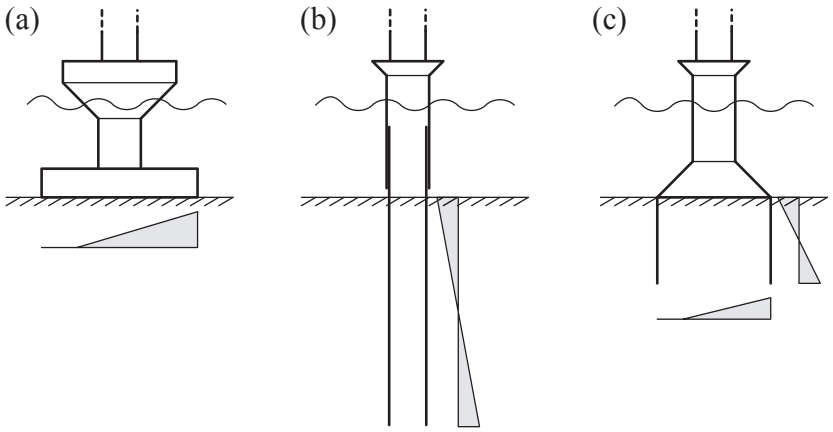

Fig. 4. Monopod support structures with soil reaction forces under moment loading. (a) Gravity based monopod; (b) monopile; (c) bucket foundation.

1.5 Monopods

The three different types of monopods are illustrated in Fig. 4. The gravity foundation (Fig. 4 a) is a shallow foundation bearing on the upper sediment layers and the loading is transferred by a large base to the seabed. The gravity base must have sufficient self-weight to avoid overturning. To obtain a large self-weight, the gravity foundations are typically constructed using reinforced concrete. Additional ballast material can be added after installation to further increase the weight. Gravity foundations have proven to be cost-effective in shallow, protected waters around Denmark. Reinforced concrete structures are built onshore and floated out to sea where they are filled with gravel and sand, similar to traditional bridge building technology. The cost-effectiveness of the gravity foundation is due to the cheap fabrication costs.

The concept is limited to sites where the upper sediment layers have a limited inclination and sufficient bearing capacity. Extensive ground preparation must be carried out before installation. The main disadvantage is the difficult handling due to the large self-weight, ranging from 1400 to over 3000 tons. The installation of a gravity foundation requires little time, but calm weather conditions are necessary.

Fig. 5. Construction yard for fabrication of monopiles for Horns Rev 2 Offshore Wind Farm, Denmark, 2008.

The monopile support structure (Fig. 4 b) is the most widely applied concept in recent offshore wind farm developments (Fig. 5). The monopile effectively extends the steel turbine tower under water. The monopile often consists of two parts; one part, the pile, is drilled or driven into the seabed until the final depth is reached, typically 20-40 m. The second part, the transition piece, has a slightly larger (or smaller) diameter than the pile, and is grouted with the pile with an overlap of 8-10 m. There are several reasons for the success of the monopile. The weight of the pile or transition piece typically does not exceed 250 tons; handling is relatively easy and several jack-ups are capable of installing a monopile. The duration for installation is short in locations where driving with a hydraulic hammer is sufficient for complete installation. In addition, the concept is well-known and only small risks are associated with monopile installation. The main disadvantage of the monopile is the high price of steel and fabrication. Also, at sites where drilling is required, installation is very slow and thus expensive. Monopile installation by means of hydraulic impact hammers is often subjected to environmental concerns.

The monopod bucket foundation (Fig. 4 c), often referred to as “suction caisson”, is a new concept which has the potential to be cost-effective in certain soil conditions. Depending on the skirt length and diameter, the bucket foundation can have a bearing capacity similar to

Fig. 6. Offshore installation of a monopod bucket foundation, Denmark, 2009.

that of a monopile, a gravity foundation or in between. The bucket foundation can be installed using suction assisted penetration combined with other installation methods. This gives the possibility of having a self-installing foundation concept, avoiding the use of expensive jack-ups and installation vessels, and thus significantly reducing installation costs. The bucket foundation can be installed in fine sands or clay materials. The bucket foundation typically requires less steel compared to monopiles; however, fabrication is slightly more expensive due to the complicated structure. Rocks or large stones can cause failure of installation, thus the concept imposes larger installation risks than monopiles. Presently, one bucket foundation has been installed onshore in Frederikshavn, Denmark, in 2004. Another, the Mobile Met Mast (Fig. 6), has been recently installed offshore at Horns Rev 2 Offshore Wind Farm, Denmark, in February 2009. The Mobile Met Mast was designed on the basis of the research work presented in this Ph.D. thesis. The bucket foundation has a promising future and more are likely to be installed in the future.

1.6 Multipods

In addition to monopods, various multipod concepts based on either gravity, piles or caissons exist. These structures differ principally from monopods as the moment resistance is obtained by a tension/compression action. The gravity, piled and caisson based multipods are illustrated in Fig. 7.

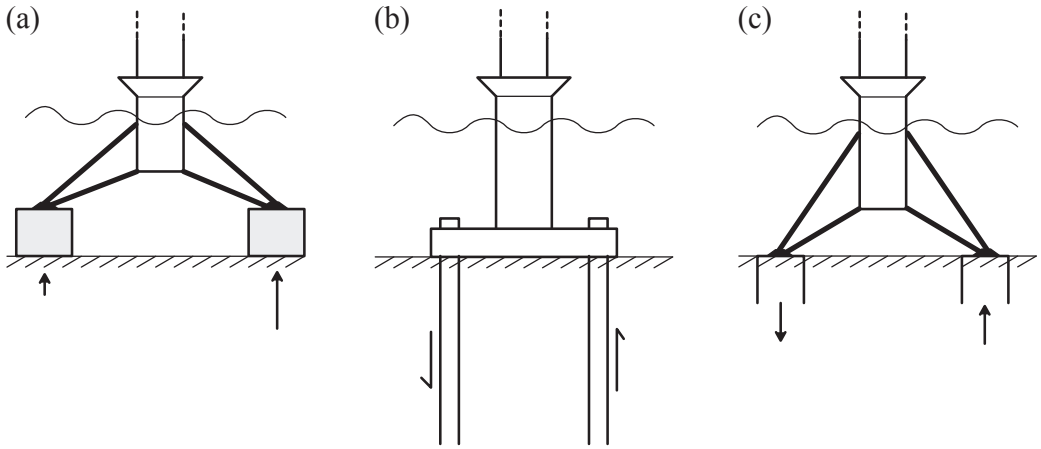

Fig. 7. Multipod support structures with soil reaction forces under moment loading. (a) Gravity based multipod; (b) piled multipod; (c) caisson based multipod.

The multipod can be designed in various geometries. The main design drivers are construction material, number of legs, length of legs and weight. The moment resistance relies on a combination of gravity, piles and caissons. Multipods are common in the oil and gas industry, but are not yet utilized in offshore wind farms.

While monopods are likely to remain competitive in shallow water depths, multipods have an advantage in deeper waters, more than 20-30 m. Erecting larger turbines in deeper waters sets high requirements to the stiffness of the support structure. The stiffness of a monopile can only be obtained by introducing a large (and expensive) amount of additional steel to the structure. However, multipods can easily be designed to fulfil stiffness requirements.

A key element to construct economically feasible support structures is to keep offshore construction work at a minimum. Exposed sites are typically governed by small weather windows for installation vessels to operate. Thus concepts such as appropriately designed multipods, allowing for rapid installation have a major advantage. The main disadvantage of multipod structures is the logistic problems arising during construction due to the geometric shape. Also, for steel multipods, the fabrication costs tend to be high due to the extensive welding work.

Experience within the offshore construction industry origins from single, purpose-made oil and gas structures. However, future offshore wind farms will consist of more than 100 turbines, thus concepts suitable for batch production must be put into use. Monopiles, as well as certain multipod designs are suitable for batch production.

2. OVERALL AIM AND SPECIFIC OBJECTIVES

2.1 Rationale

As outlined in the Introduction, the offshore wind energy sector is projected to expand significantly. The cost of support structures constitutes a significant proportion of the total cost for an offshore wind farm. Reduction of costs and risks related to support structures can significantly increase the economic feasibility of future offshore wind farms.

The costs and risks related to offshore wind turbine support structures may be reduced by:

- being able to assess the risks of structural and soil failure in the design phase;
- improving the current design guidelines in order to optimize designs and minimize risks of failure; and
- enabling novel and innovative support structures concepts to be put into use.

It is essential that research is targeted to address all the above points.

The overall aim and specific objectives of the research work presented in the present Ph.D. thesis are within the field of geotechnical engineering.

2.2 Overall aim

The overall aim was to establish novel design guidance for offshore wind turbine support structures, directly or indirectly, in order to reduce the risks and costs associated with future support structures, in particular the monopile and the bucket foundation concepts.

2.3 Specific objectives

The specific objectives were:

- to improve the current design guidelines for prediction of the accumulated tilt of an offshore wind turbine in order to minimize risks of failure due to soil fatigue in response to long-term cyclic loading originating from wind and waves;

- to develop a widely applicable numerical design tool for support structures, capable of simulating effects of cyclic loading, which may be used to benchmark and improve the current design guidelines, as well as address risks of cyclic liquefaction;

- to establish a method for interpretation of piezocone data in silt sediments in order to assess the risk of cyclic liquefaction/mobility developing in response to cyclic loading originating from an offshore wind turbine; and

- to improve the current guidelines for the design of bucket foundations in order to minimize the risk of structural buckling during installation, thereby enabling an innovative support structure concept to be put into use.

3. THE RESEARCH PROJECT

The research work presented in this Ph.D. thesis is based on research components which are not directly inter-related, as previously mentioned. The research components are divided into four research topics and are reported in five scientific papers, submitted for publication in scientific journals or conference proceedings. An overview of the research topics and publications is illustrated in Fig. 8.

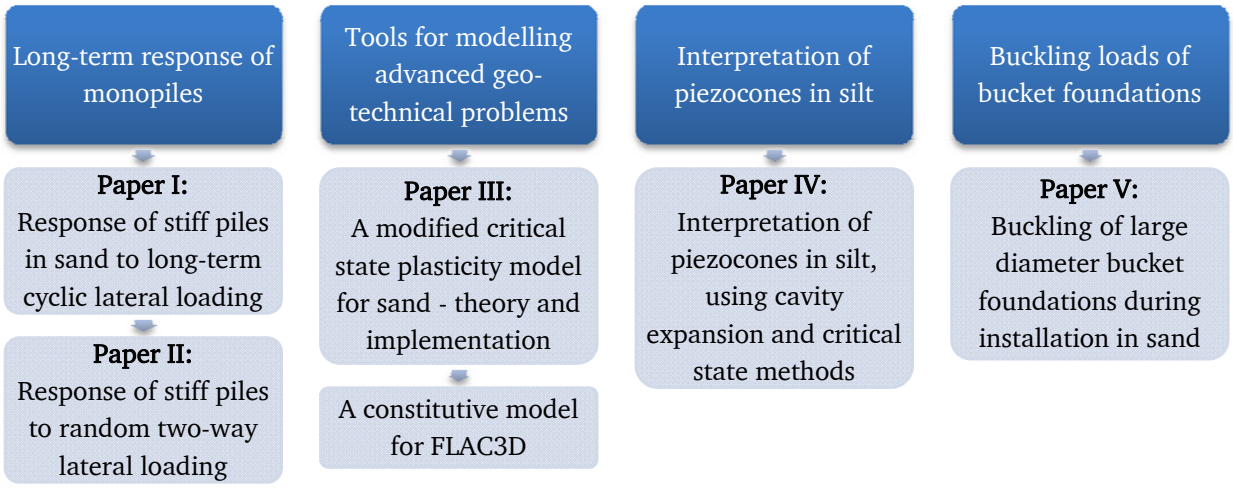

Fig. 8. Overview of the research topics and papers.

This chapter provides an overview of the contents of the five papers; including background information, rationale for the research topics, objectives and chosen methodologies.

3.1 Long-term response of monopiles

The monopile support structures are subjected to strong cyclic loading, originating from wind and wave loads, not only in extreme conditions but also in serviceability conditions. This can lead to accumulated rotation of the wind turbine tower, adversely affecting its ultimate strength and fatigue life. The long-term movements may significantly affect all parts of the wind turbine, including the support structure, machine components and blades. Therefore, it is of great importance to investigate the effects of cyclic loading.

The interactions between soil and laterally loaded piles are typically accounted for by use of $p-y$ curves, originally introduced by Reese & Matlock (1956) and McClelland & Focht (1958). The $p-y$ curves for piles in sand described by Reese *et al.* (1974) and O'Neill & Murchison (1983) led to recommendations in the standards by Det Norske Veritas (DNV

1977) and the American Petroleum Institute (API 1993) for oil and gas installations. In 2004, these recommendations were adopted in the standard "Design of offshore wind turbine structures" (DNV 2004) which represents the current state-of-the-art for design of monopiles in the offshore wind industry.

The recommended $p - y$ curves are designed primarily for evaluation of the ultimate lateral capacity. Important design issues, such as accumulated rotation and stiffness changes due to long-term cyclic loading are poorly accounted for. Methods proposed by Long & Vanneste (1994) and Lin & Liao (1999) provide simple means for predicting the effects of cyclic loading. Other investigations include small-scale tests on stiff piles reported by Peng *et al.* (2006), and a more theoretical approach by Lesny & Hinz (2007). However, further investigations are needed to verify the form of the models and to extend their use in predicting the long-term behaviour of monopiles.

Paper I: "Response of stiff piles in sand to long-term cyclic lateral loading" and Paper II: "Response of stiff piles to random two-way lateral loading" explore the load-displacement

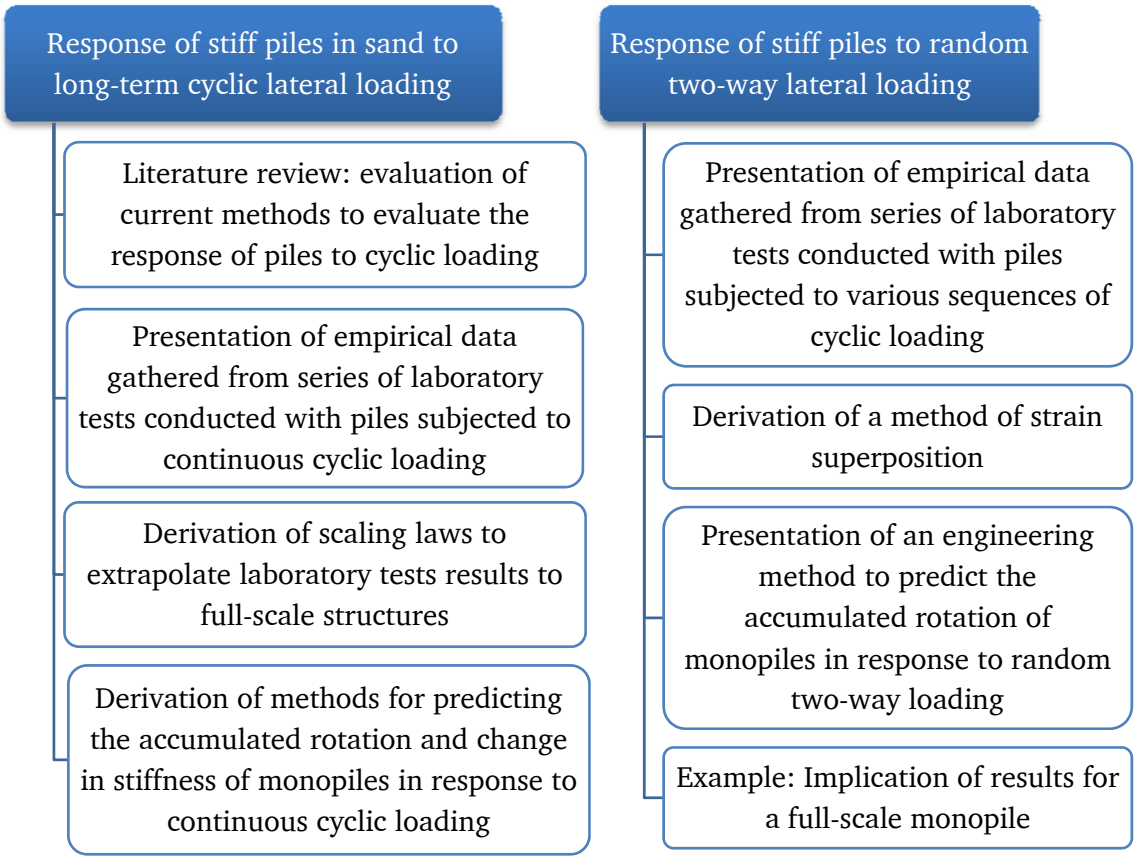

Fig. 9. Overview of Papers I and II.

behaviour of stiff monopiles in sand subjected to long-term cyclic loading. The objective was to improve the current design guidelines for prediction of the accumulated tilt of an offshore wind turbine monopile in response to cyclic loading originating from wind and waves. The research work was based on results from series of laboratory tests carried out with due consideration to scaling up of the results. An overview of the contents and the main outcomes of this research topic is shown in Fig. 9.

3.2 Modelling of advanced geotechnical problems

Numerical methods, such as finite element of finite difference, provide an important tool for investigating soil-structure interaction and optimizing the design of support structures. For soil materials, only simple, classical elasto-plastic material models are supported by most commercial engineering codes, for example Mohr-Coulomb and Cam-Clay. Whereas these models are useful for many geotechnical problems, they are insufficient for complex problems. More advanced constitutive models are required to accurately simulate the response of soil under a wide range of relative densities and mean effective stress levels, as well as cyclic loading and related observations, such as accumulation of pore pressure, cyclic mobility and cyclic liquefaction.

The critical state soil mechanics (CSSM) (Roscoe *et al.* 1958; Schofield & Wroth 1968) provides a broad framework to explain the fundamental behaviour of granular materials. The success and broad recognition of the CSSM have led to widespread application in constitutive models. A versatile and yet simple model, formulated within the framework of CSSM, is the critical state two-surface plasticity model for sands presented by Manzari & Dafalias (1997) and Manzari & Prachathananukit (2001). This model has proved to successfully simulate drained and undrained stress-strain behaviour of non-

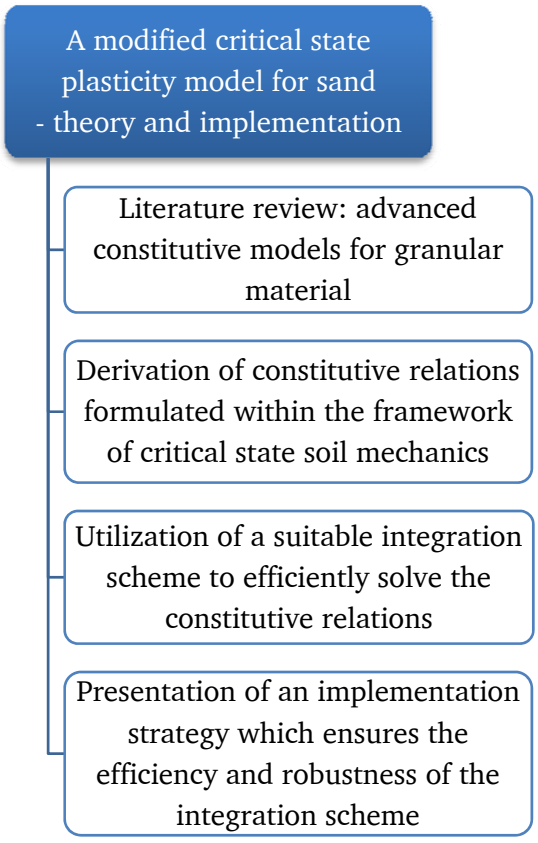

Fig. 10. Overview of Paper III.

cohesive sands under monotonic and cyclic loading in a wide range of confining stresses and densities (Manzari & Prachathananukit 2001; Taiebat *et al.* 2006).

Paper III: "A modified critical state plasticity model for sand - theory and implementation" addresses the implementation of a constitutive material model. The objective was to implement an efficient and robust advanced material model, capable of simulating the response of granular material to monotonic and cyclic loading, and thereby to obtain a powerful numerical tool for analysing soil-structure interaction which can be used to benchmark and improve current design guidelines as well as address risks of cyclic liquefaction. The plasticity model is based on the "critical state two-surface plasticity model for sands" and was implemented as a user-subroutine in the commercial finite difference code FLAC3D (Fast Lagrangian Analysis of Continua in Three Dimensions) by Itasca, using a return mapping algorithm in connection with a suitable implementation strategy. An overview of the contents and the main outcomes of this research topic is shown in Fig. 10.

3.3 Interpretation of piezocones in silt

The piezocone is the most widely used device for offshore geotechnical site investigations. A piezocone is pushed into the ground at a constant rate, while the cone resistance, sleeve friction and pore pressures are measured. The measured data give important information on the soil parameters required for the design of offshore wind turbine support structures.

Silt represents a soil, intermediate between sand and clay, in which cone penetration takes place under partially drained conditions at a standard rate of penetration. Interpretation of piezocone data in silt sediments is conceptually difficult, as the measured response is affected by the degree of pore pressure dissipation during cone penetration; therefore, methods for interpretation of piezocone tests in silt are limited and not well-established.

Silt sediments are encountered frequently in the coastal areas of the North Sea, typically at depths of 5-15 m. These sediments are problematic in relation to the design of support structures for offshore wind turbines if the soil parameters determined from the piezocone data differ significantly from those obtained by investigating intact samples in a triaxial apparatus.

Paper IV: "Interpretation of piezocones in silt, using cavity expansion and critical state methods" presents a numerical study of the process of piezocone penetration in silt sediments.

The objective was to derive a methodology capable of interpreting piezocone data in silty soils, and to derive a site-specific correlation to evaluate the *in-situ* state of the silt sediments found in the North Sea in order to assess the risk of cyclic liquefaction.

The process of cone penetration was modelled using the method of cylindrical cavity expanding, while accounting for partially drained conditions. The silt sediment was modelled using the modified critical state two-surface plasticity model. An overview of the contents and the main outcomes of this research topic is shown in Fig. 11.

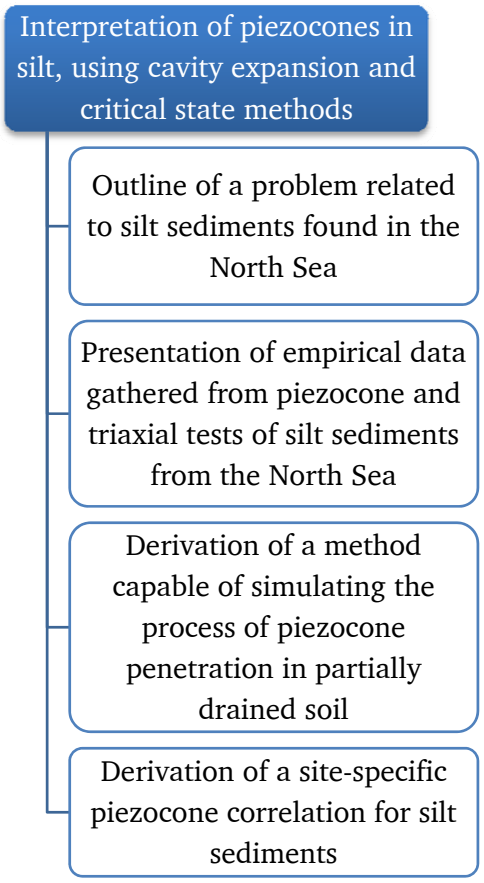

Fig. 11. Overview of Paper IV.

3.4 Buckling loads of bucket foundations

Bucket foundations have the potential to be a cost-effective option for future offshore wind farms, if suction assisted penetration is employed. The suction installation technology was introduced originally by Shell (Senepere & Auvergne 1982), and currently is used widely for suction anchor piles and skirted foundations within the oil and gas offshore industry. During installation, suction is added to create a pressure differential across the bucket lid, thereby effectively increasing the downward force on the bucket while reducing the skirt tip resistance. Presently, a single wind turbine supported by a bucket foundation has been installed (Ibsen 2008).

The geometry of bucket foundations falls into the category of thin shell structures as the ratio between the bucket diameter and wall thickness is very large. Therefore, the structure is particularly exposed to structural buckling due to the predominantly hydrostatic loading during installation. Buckling is therefore a major design consideration.

Over the last decades, much research has been carried out to investigate the imperfection sensitivity of shell buckling (Teng 1996); however, the methods recommended by current standards are considered as semi-empirical due to the lack of agreement between theoretical

and experimental buckling loads. Buckling failure loads are influenced by several factors, in particular, geometric imperfections, residual stresses, material plasticity, lid stiffness and the degree of lateral support provided by the soil to the embedded skirt.

Paper V: "Buckling of large diameter bucket foundations during installation in sand" addresses the risk of failure during installation of bucket foundations using suction assisted penetration. The objective was to benchmark theoretical expressions and current standards for evaluating buckling loads, and to provide design guidance on issues not addressed by the current standards, thereby minimizing the risk of structural buckling during installation and enabling an innovative support structure concept to be put into use. The research work was based on finite element methods and observations from full-scale bucket foundations. An overview of the contents and the main outcomes of this research topic is shown in Fig. 12.

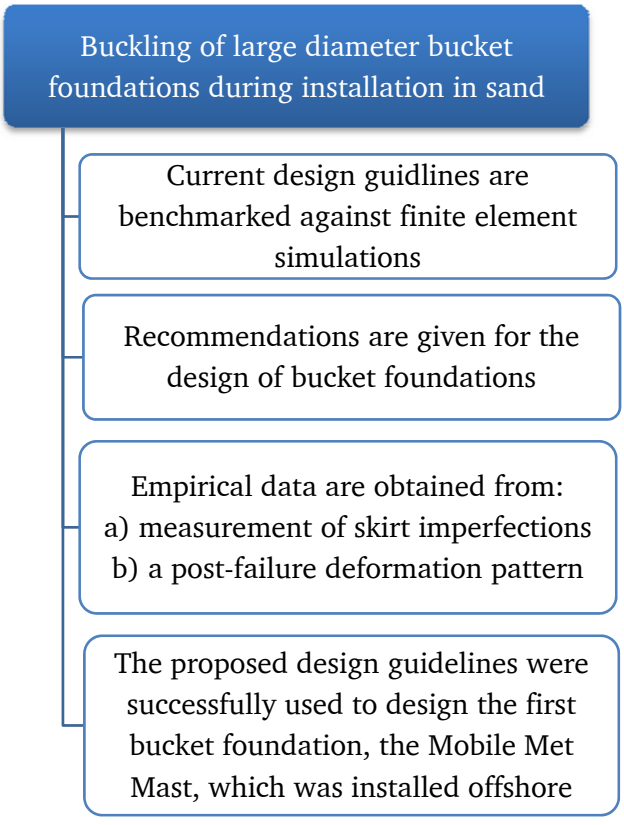

Fig. 12. Overview of Paper V.

4. CONCLUSIONS AND RECOMMENDATIONS FOR FUTURE RESEARCH

The research work presented in this Ph.D. thesis was undertaken to improve the design of future offshore wind turbine support structures. The work has been divided in four selected research topics in the field of geotechnical engineering which are not directly inter-related. Each research topic was targeted to assess risks of failure, improve the current design guidelines or enable the use of innovative concepts for future support structures. Overall, the outcomes of the research work presented in this Ph.D. thesis may reduce risks and costs related to support structures, either directly or indirectly, and thereby contribute to increasing the economic feasibility of future offshore wind farms.

This chapter outlines the major contributions and main conclusions of the research work. Furthermore, recommendations for future research, and the technological developments necessary for the research, are suggested on the basis of the current design guidelines and the research work presented in this Ph.D. thesis.

4.1 Long-term response of monopiles

Fundamental investigations conducted in a laboratory were used to develop design guidelines for prediction of the accumulated tilt of offshore wind turbines in response to cyclic loading originating from wind and waves. The outcome improves the current guidelines for design of monopiles and minimizes the risk of failure due to soil fatigue.

The major contribution is a novel engineering methodology capable of incorporating effects of continuous or random two-way cyclic loading on the response of monopiles in a simple manner. The basis for the method is supported by results of 1-g laboratory tests in which a stiff pile, installed in sand, was subjected to 10-10000 cycles of varying amplitude and mean load. The tests were conducted at a scale of 1:50 of a typical monopile. A complete non-dimensional framework for stiff piles in sand was derived and applied to interpret the test results.

The tests results showed that the accumulated rotation of monopiles is largely affected by the characteristics of the applied cyclic load. Thus, parameters characterizing the load, other than maximum load levels, are required for accurate predictions. A very significant result was that

the most onerous loading condition was found to be between one-way and two-way loading. Also, the results showed that cyclic loading always increases the pile stiffness and the increase is independent of relative density. This contrasts with the current methodology of degrading static $p - y$ curves to account for cyclic loading.

The methodology proposed for prediction of the accumulated rotation of an offshore wind turbine monopile in response to random two-way loading is based on the following 6 assumptions, which are supported by laboratory tests:

- The accumulation of pile rotation under continuous cyclic loading increases with a power to the number of load cycles.
- The order of cyclic loading is irrelevant, thus, any load series may be rearranged into a convenient series of cyclic loading.
- Load cycles can be superposed according to a relationship similar to Miner's rule.
- Reversed load cycles can be accounted for by subtraction.
- A rainflow-counting method can be used to decompose a time series of varying loads into a set of load reversals.

The derived method was applied to predict the long-term response of a typical full-scale monopile. The results suggest that considerations of accumulated rotation may be a primary design driver and the largest load cycles, though very few, have a much higher impact on the accumulated rotation than 10^7 cycles at the fatigue limit state.

The research work presented provides preliminary guidelines which give a strong basis for further research. Of particular interest is the scalability of the results to full-scale monopiles. Therefore, future work should include field trials of monopiles in sand. Laboratory tests, when interpreted carefully in terms of properly chosen, dimensionless variables, may be used successfully for the design of full-scale structures. However, the proposed method for predicting accumulated rotation relies on one dimensionless parameter and two dimensionless functions, empirically determined from laboratory tests, to which no scaling laws are applied. It should be borne in mind that the proposed scaling relationships for stiffness and capacity values, in absolute terms, differ by several orders of magnitude. Thus, direct application of the proposed methodology requires a high degree of confidence in the applied (or lack of) scaling laws. In this context, field testing of almost real sized monopiles, for example, with a diameter of 1 m, in a controlled loading environment will provide very important information. Laboratory tests may be conducted to mimic field trials of monopiles

and scaling laws may be developed to allow laboratory tests and field trials of monopiles in sand to be compared in terms of stiffness, capacity and accumulated rotation. If the agreement between laboratory and field results is highly satisfactory, these comparisons will give confidence to the use of the scaling laws for design of full-scale monopiles.

Further research should also investigate piles installed in very dense and saturated sand, the effect of altering pile dimensions, and the response of piles to multi-directional loading.

4.2 Modelling of advanced geotechnical problems

A widely applicable numerical design tool for support structures, capable simulating effects of cyclic loading, was developed on the basis of the commercial finite difference code FLAC3D - a tool which can be used to benchmark and improve current design guidelines, as well as address the risk of failure due to cyclic liquefaction/mobility of soils in response to cyclic loading originating from an offshore wind turbine. The major contribution is information on the derivation, integration and implementation of an advanced plasticity model for granular material capable of simulating effects of cyclic loading and a thoroughly tested user-defined sub-routine for FLAC3D.

An advanced plasticity model, similar to the model proposed by Manzari & Dafalias (1997), was presented and special emphasis was made to outline the physical interpretation of the model, especially the important role of the state parameter which is used to define the peak shear strength of sands, as well as the point of transition from compactive to dilative behaviour. A multi-axial surface formulation, based on a versatile shape function, was introduced and adopted to prescribe a family of smooth and convex contours in the π-plane. A fast and accurate time-stepping integration scheme, based on the general return mapping method suitable for an explicit global solver, was implemented and tested. The integration scheme was found to have convergence problems at low mean effective stress levels. The convergence problems were addressed by adopting a suitable implementation strategy to ensure stability and robustness. The performance of the integration scheme was tested and appropriate tolerance criteria were suggested to obtain sufficient efficiency, stability and accuracy. The plasticity model was implemented and thoroughly tested in FLAC3D and was proven capable of accurately simulating triaxial test data of silt sediments from the North Sea (LeBlanc & Randolph, 2008).

Future research work should address the calibration of the model. The model has several model parameters and it may be difficult to determine the optimal parameters during model calibration. Therefore, suitable calibration strategies must be developed to ease the calibration process. Furthermore, the model should be calibrated to a wide range of soils, in order to a) prove the simulation capabilities of the model, and b) gain experience with representative values of model parameters. In addition, research should include general application of the plasticity model to analyse complex problems relating to soil-structure interaction.

4.3 Interpretation of piezocones in silt

A novel methodology for interpretation of piezocone data in silt sediments was established in order to assess the risk of cyclic liquefaction/mobility developing in silt layers in response to the cyclic loading of an offshore wind turbine.

The major contribution is the establishment of a numerical methodology capable of generating a site-specific correlation between triaxial test data and the *in-situ* state of silt sediments. The method addresses problems of deriving soil parameters on the basis of piezocone tests and triaxial tests of intact, but possibly disturbed, soil samples.

The method partly accounts for the complex deformation of the soil around the cone during penetration and includes effects of drainage conditions in saturated soil. The process of piezocone penetration was modelled in FLAC3D as a cylindrical cavity expanding in a saturated two-phase soil, under the assumption of axial symmetry conditions to generate a correlation between the *in-situ* state parameter and two piezocone parameters; the corrected cone tip resistance and the dynamic pore pressure measured at the cone shoulder. The *in-situ* state of silt was expressed in terms of the state parameter which, in conjunction with the critical state line, provides a precise definition for the state of silt.

The proposed methodology was successfully applied in a case study of silt sediments originating from the North Sea, at a location where one piezocone test and one vibro-core sampling test had been performed. The results suggested the seemingly contradictory evidence of low cone resistance and high triaxial shear strength could be explained readily. The low cone resistance was a derived effect of the silt having a large slope of the critical state line, resulting in rather weak and compressible behaviour at high mean effective stresses.

Further research should address verification and benchmarking of the proposed method, using sets of related piezocone and triaxial test results. For example, the model may be calibrated to undisturbed triaxial test results, and then used to predict the piezocone parameters. Thereafter, the model prediction may be benchmarked against measured piezocone parameters. Correct interpretation of piezocones in silt sediments remains a partly unresolved issue when intact silt samples are unavailable.

4.4 Buckling loads of bucket foundations

Guidelines for design of bucket foundations against structural buckling were developed on the basis of advanced numerical methods and observations from full-scale structures. The outcomes of the research work extend the current design guidelines and may be used to minimize the risk of failure during suction installation of future bucket foundations. If installation risks are handled successfully, the bucket foundation can be put into use as a novel and innovative support structure.

The major contributions are novel design guidelines for predicting the buckling pressure of bucket foundations during suction installation in sand. The hydrostatic buckling pressures of large diameter bucket foundations installed in sand were analysed using three-dimensional, non-linear finite element analyses, while accounting for material plasticity, geometric imperfections, residual stresses, embedment depth and derived effects of adding suction, such as the presence of hydraulic gradients in the soil. Theoretical expressions and current standards for evaluating buckling loads were benchmarked and design guidance was given for future bucket foundations. The results and conclusions presented were successfully used to design the first bucket foundation, the Mobile Met Mast, which was installed offshore in Denmark, 2009.

The main conclusions are summarized below:

- The recommendations by DNV (2002) appear to provide a conservative estimate of the hydrostatic buckling pressure, if the geometric skirt imperfections are less than thrice the wall thickness.
- The severity of realistic imperfections can be significantly less than the severity of imperfections generated from an eigenmode analysis. Thus, it may be appropriate to measure the as-built imperfections and perform refined numerical buckling analyses.

- It is recommended that the number and position of weldings be considered in the design phase in order to avoid geometric imperfections which are close to the deformation pattern of the eigenmode imperfections.
- Residual stresses, one third of the yield stress, were found to reduce the buckling pressure by approximately 10%.
- It is recommended that the skirt support from the lid of the bucket foundation is assumed pinned unless refined analyses, incorporating the actual lid geometry, are performed. A clamped lid support increased the buckling pressure by approximately 10%.
- The lateral support provided to an embedded skirt by sand is significant in respect to structural buckling. The degree of skirt fixation may conveniently be expressed in terms of the equivalent pinned embedment depth which depends on the bucket properties, the sand properties, the embedment depth and the degree of applied suction. Appropriate values of the equivalent pinned embedment depth were determined numerically and observations from a bucket foundation in Wilhelmshaven, which failed due to buckling, confirmed the numerical findings.
- The equivalent pinned penetration depth is a function of the applied suction. The effect of adding suction increased the equivalent pinned penetration depth by up to 0.4 m.
- A simple calculation method for designing a bucket foundation against hydrostatic buckling during suction installation is proposed.

The research work addressed shortcomings of the current standards. Preliminary guidelines are presented which may be adopted to reduce the risk of buckling failure during installation of future bucket foundations. The validity of the presented guidelines is limited to bucket foundations with dimensions comparable to those used in the numerical analyses. Further research should aim at developing design guidelines which are valid for arbitrary bucket dimensions and attempt to verify the main conclusions by physical testing. Horizontal loading of the bucket skirt may arise from waves, currents or the installation vessel, thus, future research should also aim at investigating the effect of horizontal loading on the hydrostatic buckling pressure.

4.5 Concluding remarks

The research work presented in this Ph.D. thesis was targeted to improve the design of offshore wind turbine support structures. Important topics, all relating to the field of geotechnical engineering, were selected and investigated, using numerical methods and/or physical testing in order to a) assess risks of failure, b) improve the current design guidelines, and c) enable the use of innovative support structure concepts. The outcomes of each of the four research topics contribute, either directly or indirectly to reducing the risks and costs associated with future support structures. The research work focused on the monopile, the most common support structure concept, and the bucket foundation, a novel and innovative support structure concept. Overall, the outcomes of the research work enable low-cost and low-risk support structures to be put into use and are therefore an important contribution to increase the economic feasibility of future offshore wind farms.

LITERATURE CITED

API (1993). *Recommended practice for planning, designing, and constructing fixed offshore platforms - working stress design*. American Petroleum Institute, Washington D. C., RP2A-WSD.: 20th ed.

DNV (1977). *Rules for the design, construction and inspection of offshore structures.* Det Norske Veritas, Høvik.

DNV (2002). *Recommended practice: Buckling strength of shells*. Det Norske Veritas, Høvik, DNV-RP-C202.

DNV (2004). *Offshore standard: design of offshore wind turbine structures.* Det Norske Veritas, Hellerup, DNV-OS-J101.

Ibsen, L. B. (2008). Implementation of a new foundations concept for offshore wind farms. *Proc., 15th Nordic Geotechnical Meeting*, Sandefjord, 19-33.

Kühn, M. (2001). *Dynamic and design optimisation of offshore wind energy conversion systems.* DUWIND Delft University Wind Energy Research Institute, Delft. ISBN 90-76468-07-9.

LeBlanc, C. & Randolph, M. F. (2008). Interpretation of piezocones in silt, using cavity expansion and critical state methods. *Proc., 12th Conf., International Association for Computer Methods and Advances in Geomechanics*, India. 822-829.

Lesny, K. & Hinz, P. (2007). Investigation of monopile behaviour under cyclic lateral loading. *Proc.,Offshore Site Investigation and Geotechnics*, London, 383-390.

Lin, S. S. & Liao, J. C. (1999). Permanent strains of piles in sand due to cyclic lateral loads. *J. of Geotech. and Geoenv. Engng.* **125**, No. 9, 798-802.

Long, J. & Vanneste, G. (1994). Effects of cyclic lateral loads on piles in sand. *J. of Geotech. Engng.* **120**, No. 1, 225-244.

Manzari, M. T. & Dafalias, Y. F. (1997). Critical state two-surface plasticity model for sands. *Geotechniqué* **47**, No. 2, 255-272.

Manzari, M. T. & Prachathananukit, R. (2001). On integration of a cyclic soil plasticity model. *Int. J. for Numerical and Analytical Methods in Geomechanics* **25**, No. 6, 525-549.

McClelland, B. & Focht, J. (1958). Soil modulus for laterally loaded piles. *Transactions, ASCE* **123**, 1049-1086.

O'Niell, M. W. & Murchison, J. M. (1983). *An evaluation of p-y relationships in sands.* Dept. of Civil Engineering, University of Houston, Houston, Research Rep. No. GT-DF02-83.

Peng, J. R., Clarke, B., & Rouainia, M. (2006). A device for cyclic lateral loaded model piles. *Geotech.Testing J.* **29**, No. 4, 1-7.

Reese, L., Cox, W. R., & Koop, F. D. (1974). Analysis of laterally loaded piles in sand. *Proc., 6th Offshore Tech. Conf.*, Houston, Paper No. 2079.

Reese, L. & Matlock, H. (1956). Nondimensional solutions for laterally loaded piles with soil modulus assumed proportional to depth. *Proc., 8th Conf. on Soil Mech. and Found. Eng.*, University of Texas, Austin, Special Publication No. 29.

Roscoe, K. H., Schofield, A. N. & Wroth, C. P. (1958). On yielding of soils. *Geotechniqué* **8**, No. 1, 22-53.

Schofield, A. N. & Wroth, C. P. (1968). *Critical state soil mechanics*. McGraw-Hill, London.

Senepere, D. & Auvergne, G. A. (1982). Suction anchor piles – a proven alternative to driving or drilling. *Proc., 14th Offshore Tech. Conf.*, Houston, 483-493.

Taiebat, M., Shahir, H. & Pak, A. (2006). Study of pore pressure variation during liquefaction using two constitutive models for sand. *Soil Dynamics and Earthquake Engineering* **27**, No. 1, 60-72.

Teng, J. G. (1996). Buckling of thin shells: recent advances and trends. *Applied Mechanics Reviews* **49**, No. 4, 263-274.

SCIENTIFIC PAPERS

PAPER I

LeBlanc, C., Houlsby, G. T. & Byrne, B. W.

Response of stiff piles in sand to long-term cyclic lateral loading

Geotechniqué, October 2008. Accepted.

Monopiles at Horns Rev 2 Offshore Wind Farm, Denmark

Response of stiff piles in sand to long-term cyclic lateral loading

Christian LeBlanc[1], Guy T. Houlsby[2] and Byron W. Byrne[3]

1) Ph.D. research student, Dept. of Civil Engineering, Aalborg University & Dept. of Offshore Technology, DONG Energy, A.C.Meyers Vænge 9, 2450 Copenhagen SV, Denmark. Phone: (+45) 9955 2558. E-mail: chrle@dongenergy.dk

2) Professor of Civil Engineering, Dept. of Engineering Science, Parks Rd., Oxford OX1 3PJ, UK.

3) University Lecturer in Civil Engineering, Dept. of Engineering Science, Parks Rd., Oxford OX1 3PJ, UK.

Keywords: Piles, Repeated loading, Laboratory tests, Sands, Settlement, Stiffness

Date written: 30.10.2007

Date revised: 13.10.2008

Number of words: 5326

Number of pages: 45

Number of figures: 13

Number of tables: 5

ABSTRACT

The driven monopile is currently the preferred foundation type for most offshore wind farms. Whilst static capacity of the monopile is important, a safe design must also address issues of accumulated rotation and changes in stiffness after long-term cyclic loading. Design guidance on this issue is limited. To address this, a series of laboratory tests were conducted where a stiff pile in drained sand was subjected to between 8000 and 60000 cycles of combined moment and horizontal loading. A typical design for an offshore wind turbine monopile was used as a basis for the study, to ensure that pile dimensions and loading ranges were realistic. A complete non-dimensional framework for stiff piles in sand is presented and applied to interpret the test results. The accumulated rotation was found to be dependent on relative density and was strongly affected by the characteristics of the applied cyclic load. Particular loading characteristics were found to cause a significant increase in the accummulated rotation. The pile stiffness increased with number of cycles, which contrasts with the current methodology where static load-displacement curves are degraded to account for cyclic loading. Methods are presented to predict the change in stiffness and the accumulated rotation of a stiff pile due to long-term cyclic loading. The use of the methods developed is demonstrated for a typical full-scale monopile.

INTRODUCTION

Wind power currently offers a very competitive source of renewable energy, and therefore the market for onshore and offshore windfarms is projected to expand rapidly within the next decade. There are strong political and industrial forces, especially in northern Europe, supporting the development of offshore wind power to reduce reliance on fossil fuels and control greenhouse gas emissions.

There are several foundation concepts for offshore wind farms. The cost-effectiveness of a particular concept depends to a large extent on the site conditions. Most current foundations are ‘monopiles’, which are stiff piles with large diameters, driven 20 m to 30 m into the seabed. Recently installed monopiles have diameters in the range of 4 m to 6 m and a length/diameter ratio of approximately 5. Fig. 1 illustrates the proportions of a typical offshore wind turbine on a monopile foundation.

The design of monopiles relies on standards and empirical data originating from the offshore oil and gas sector. However, the loading of an offshore wind turbine is very different in both magnitude and character to oil and gas installations. It is characteristic for offshore wind turbines that the sub-structure will be subjected to strong cyclic loading, originating from the wind and wave loads. This occurs not only during extreme conditions but also during serviceability conditions. This can lead to accumulated rotation of the wind turbine tower, adversely affecting its ultimate strength or fatigue life. The long-term movements of the foundation may significantly impact all parts of the wind turbine, including the support structure, machine components and blades. Therefore, it is of great importance to investigate the effects of cyclic loading.

The primary design drivers for offshore wind turbine foundations are those of deformation and stiffness rather than ultimate capacity. Modern offshore wind turbines are

designed as “soft-stiff” -structures, meaning that the 1st natural frequency is in the range between the excitation frequency bands, 1P and 3P, in order to avoid resonances. 1P and 3P denote the frequency bands of the rotor rotation and the blade passing, typically in the range of 0.3 Hz and 1 Hz, respectively. Long-term cyclic loading of the foundation is likely to change the stiffness of the surrounding soil and therefore the interaction of the foundation and the soil, due to accumulation of irreversible deformations. Any significant change in stiffness may result in interference between the 1^{st} natural frequency and the excitation frequencies, 1P or 3P, which would be highly problematic. Thus, it is important to assess the concepts of stiffness and/or strength changes during long-term cyclic loading.

The performance of monopiles subjected to long-term cyclic loading must therefore be addressed to achieve a safe design of an offshore wind turbine. Although many useful methods have been proposed to predict the response of piles to lateral cyclic loading, methods predicting the accumulated rotation and resulting stiffness due to long-term cyclic loading are limited. This paper explores the load-displacement behaviour of stiff monopiles in sand subjected to long-term cyclic loading. The objective is to provide information for the development of a conceptual model capable of predicting the response of monopiles to this loading.

Laboratory tests were conducted to simulate a driven monopile in drained conditions subjected to 8000-60000 load cycles of combined moment and horizontal loading. In comparison, a typical offshore wind turbine is designed for a fatigue load with 10^7 cycles. The laboratory tests were carried out on the laboratory floor, with due consideration of issues of scaling of the results. The main advantage of performing the experiments at $1g$ was the capability to apply up to 60000 load cycles in a realistic timeframe whilst maintaining high quality displacement measurements. It was possible to isolate the testing rig from the effect of external vibrations, so that the displacements of the pile measured were solely related to the

applied loading conditions.

CURRENT METHODOLOGY

Piles are widely used for various structures such as bridges, high-rise structures and offshore oil and gas installations. The interactions between soil and laterally loaded piles are typically accounted for by use of p-y curves, originally introduced by Reese and Matlock (1956) and McClelland and Focht (1958). The p-y curves adopt the Winkler approach by uncoupling the response of various layers in the soil and can therefore easily include effects of non-linearity, soil layering and other soil properties. A p-y curve defines the relationship $p(y)$ between the soil resistance p arising from the non-uniform stress field surrounding the pile mobilised in response to the lateral pile displacement y, at any point along the pile. Implementation of p-y-curves requires a numerical procedure to solve the fourth-order differential equation for beam bending with appropriate boundary conditions

$$E_p I_p \frac{d^4 y}{dz^4} - p(y) = 0 \quad , \quad z \in [0; L] \tag{1}$$

in which E_p and I_p denote the elastic modulus and second moment of area of a pile, respectively.

The p-y curves have evolved primarily from research in the oil and gas industry, as the demand for large pile-supported offshore structures increased during the 1970s and 1980s. Research has included testing of full-sized piles in sand under both static and cyclic loading conditions. An overview of the important tests and results are given by Reese and Impe (2001). The p-y curves for piles in sand described by Reese *et al.* (1974) and O'Neill and Murchison (1983) lead to recommendations in the standards (DNV 1977; API 1993) for oil and gas installations. In 2004, these recommendations were adopted in the standard "Design of

Offshore Wind Turbine Structures" (DNV 2004) which represents the current state-of-the-art for design of monopiles in the offshore wind industry.

The method adopted in the standards uses a procedure to construct non-linear p-y curves for monopiles in sand subjected to cyclic loading as a function of the static ultimate lateral resistance p_u

$$p = Ap_u \tanh\left(\frac{Bz}{Ap_u} y\right) \qquad A = 0.9 \text{ for cyclic loading} \tag{2}$$

in which B is an adjustment parameter to account for the relative density of the sand. This method was originally developed by O'Neill and Muchison (1983) and has some theoretical basis. However, it relies to a high degree on empiricism, using data obtained primarily from two full-scale load tests reported by Cox *et al.* (1974). These tests were conducted using two slender piles, with diameter 0.61 m and length 21 m. The piles were subjected to static and cyclic lateral load. To assess the validity of the method, systematic studies were conducted by Murchison and O'Neill (1984) which proved the method to be superior to other methods. However, the validity of the method relies on very few tests on relatively flexible driven steel piles subjected to cyclic loading.

Shortcomings of current methodology

The current design methodology, based on p-y curves, has gained broad recognition due to the low failure rate of piles over several decades. However, when applied to offshore wind turbine foundations the design methodology is being used outside its verified range and several design issues are not properly taken into account.

Firstly, current standards rely on methods built upon empirical data obtained from long, slender and flexible piles. When scaling to large diameter piles, a distinction must be made between a pile that behaves in an almost rigid fashion to one that is relatively flexible, since this affects the soil-pile behaviour (Briaud *et al.* 1984). A rigid pile rotates without flexing significantly and

develops a “toe-kick” under moment and lateral loading. Criteria for rigid or flexible behaviour have been proposed by various researchers, for example Dobry *et al.* (1982), Budhu and Davies (1987) and Carter and Kulhawy (1988). The range of transition from flexible to rigid pile behavior may, according to Poulos and Hull (1989), be evaluated by

$$4.8 < \left(\frac{E_s L^4}{E_p I_p}\right) < 388.6 \tag{3}$$

in which E_s denotes the elastic modulus of the soil. A typical monopile has a diameter of 4 m, wall thickness of $0.05 - 0.07$ m and penetration depth of 18 m. According to (3), the transition from rigid to flexible pile behavior occurs in the range from $E_s \approx 14$ MPa to $E_s \approx 1121$ MPa. Thus, for most sands encountered the monopile behavior tends toward the rigid case.

Secondly, the recommended p-y curves for cyclic loading are designed primarily for evaluation of the ultimate lateral capacity. Important design issues, such as accumulated rotation and stiffness changes due to long-term cyclic loading, are poorly accounted for. Long-term cyclic loading is likely to densify, or in some circumstances possibly loosen, the surrounding soil, resulting in changes to the stiffness of the foundation. Additionally, an accumulated rotation during the lifetime of an offshore wind turbine is expected, since the cyclic loading often occurs from one direction. The current design methodology is not capable of predicting either effects of soil densification or long-term movements of the monopile.

Finally, the current methodology accounts for cyclic loading in an incomplete manner. Repetitive lateral load tests on two offshore piers in Tampa Bay, reported by Long and Vanneste (1994), showed much greater displacements than predicted using the p-y curves proposed by Reese *et al.* (1974). The reason for this discrepancy, according to Long and Vanneste (1994), is that the cyclic p-y curves do not account for such factors as installation method, load characteristics and number of load cycles.

METHODS FOR PREDICTING THE RESPONSE TO LONG-TERM CYCLIC LOADING

The inadequacy of current methodology for predicting the cyclic loading response of piles means that new models, incorporating factors affecting the cyclic behaviour, must be developed. Results from 34 full-scale cyclic lateral load tests of piles in sand were collected by Long and Vanneste (1994) to identify those factors affecting the cyclic behaviour. These included soil density, pile type, installation method and most importantly the characteristics of the cyclic load. Long and Vanneste (1994) adopted a method, originally introduced by Little and Briaud (1988), to account for cyclic loading. The method is based on the deterioration of static p-y curves, which is taken into account by reducing the static soil reaction modulus according to

$$\frac{R_N}{R_0} = N^{-\alpha} \tag{4}$$

in which R_0 and R_N denote the soil reaction modulus on the first and N'th load cycle, respectively. α is an empirically determined degradation parameter which depends on the installation method, soil density and load characteristics.

By investigating a subset of the full-scale tests, Lin and Liao (1999) proposed that the accumulated displacement of piles can be predicted by

$$\frac{u_N - u_0}{u_0} = \beta \ln(N) \tag{5}$$

in which u_0 and u_N denote the pile head deflection in the first and N'th load cycle, respectively. β is an empirical degradation parameter, similar to α, depending on the installation method, soil density and load characteristics.

The methods proposed by Long and Vanneste (1994) and Lin and Liao (1999) provide simple means for predicting the effects of cyclic loading. However, the determination of the

empirical degradation parameters relies on a small number of tests carried out on long, flexible piles subjected to fewer than 50 cycles of loading. Further investigations are needed to verify the form of the models and to extend them for use in predicting the long term behaviour of stiff, driven piles. Other investigations include small-scale tests on stiff piles subjected to 10000 cycles as reported by Peng *et al.* (2006). However, only a few tests are reported and the data interpretation is limited. A more theoretical approach is given by Lesny and Hinz (2007), who attempt to predict accumulated displacements using data from cyclic triaxial tests and a finite element model incorporating Miner's law. The method is theoretical and still requires validation against experimental data.

DIMENSIONLESS EQUATIONS FOR SCALING OF LABORATORY TESTS

The basis of this paper is a set of laboratory floor experiments on stiff monopiles in sand. Results from laboratory tests of foundations in sand must be carefully scaled to predict the behaviour of a full-scale structure. As is well recognised for structures on sand, the loading response is governed by the frictional behaviour of the sand, which in turn is governed by the isotropic stress level. In the laboratory the isotropic stress level controlling the test behaviour is low, resulting in higher friction angles but lower shear stiffnesses, in comparison to a full-scale test. These issues of scaling can be addressed by choosing appropriate scaling methods, as presented in the following.

To ensure that the peak friction angle in a laboratory test corresponds to the value in a full-scale test, the soil sample is prepared at a lower relative density. This is straightforward, but the issues of stiffness are more complex. An attempt to account for the influence of isotropic stress level is made by expressing the shear modulus, G, as

$$\frac{G}{p_a} = c_1 \left(\frac{\sigma'_v}{p_a}\right)^n \tag{6}$$

in which p_a is the atmospheric pressure, c_1 is a dimensionless constant, σ'_v, is an appropriate effective vertical stress and n is the pressure exponent (Kelly *et al.* 2006). Evaluation of the shear modulus using equation (6) requires the determination of a representative vertical effective stress, σ'_v. The vertical effective stress around a pile varies with depth. Thus, an appropriate choice is to use the vertical stress at a depth $c_2 L$ below the seabed

$$\sigma'_v = c_2 L \gamma' \tag{7}$$

in which γ' is the effective unit weight and c_2 is a dimensionless constant. The pressure exponent in equation (6) is reported to vary from 0.435, at very small strains, to 0.765, at very large strains (Wroth *et al.* 1979). The shear strain range of greatest interest is likely to fall in the range 10^3 to 10^4 (Simpson 2002). In this range n is reported to be around 0.75 for sands (Park and Tatsuoka 1994; Porovic and Jardine 1994). However, a value of 0.5 may capture most of the important features of increased shear stiffness with pressure (Wroth and Houlsby 1985). This is confirmed by Kelly *et al.* (2006) who successfully adopted a value of 0.5 to compare results of laboratory and full-scale tests of suction caisson foundations.

For the case of a monopile subjected to a horizontal load H and moment M at the seabed, the resulting lateral displacement u and rotation θ can be obtained from an elastic stiffness relation, expressed as

$$\begin{bmatrix} M/L \\ H \end{bmatrix} = DG \begin{bmatrix} k_1 & k_2 \\ k_2 & k_3 \end{bmatrix} \begin{bmatrix} L\theta \\ u \end{bmatrix} \tag{8}$$

in which $k_1 \ldots k_3$ are dimensionless constants. To obtain the moment-rotation relationship, u can be eliminated to give

$$M = \left(\frac{GL^2 D(k_1 k_3 - k_2^2)}{k_3 - k_2(HL/M)}\right)\theta \tag{9}$$

The issue of scaling is addressed by incorporating equation (6) and equation (7) in

equation (9) to obtain a moment-rotation relationship given entirely in terms of non-dimensional parameters

$$\underbrace{\frac{M}{DL^3\gamma'}}_{\tilde{M}} = \underbrace{\frac{c_1\sqrt{c_2}(k_1k_3 - k_2^2)}{k_3 - k_2(HL/M)}}_{\tilde{k}} \underbrace{\sqrt{\frac{p_a}{L\gamma'}}\theta}_{\tilde{\theta}} \tag{10}$$

in which $\tilde{k}$ is the non-dimensional stiffness and $\tilde{M}$ and $\tilde{\theta}$ are the non-dimensional values of moment and rotation, respectively. The non-dimensional moment/force ratio arising in $\tilde{k}$ will be denoted $\tilde{e} = M/HL$, called the non-dimensional load eccentricity. This suggests that a satisfactory comparison between tests can be obtained by plotting $\tilde{M}$ against $\tilde{\theta}$ while $\tilde{e}$ and other parameters influencing $\tilde{k}$ are kept constant.

Several other parameters may influence the $\tilde{M}$-$\tilde{\theta}$ relationship. These can be understood by investigating the static moment resistance of a monopile. Consider the idealised horizontal stress distribution, in the ultimate lateral limit state, along a stiff pile in sand as illustrated in Fig. 2. The resulting distributed horizontal load along the pile is determined by $KD\sigma_v' = KD\gamma' z$, in which K is a factor depending on the friction angle, see for example (Broms 1964) and d is the depth of the pivot point. The pile toe is assumed to shear at the critical state friction angle φ_{cr}. Thus, the shear resistance at the bottom of the pile is governed by the vertical effective force arising from the overburden sand $(\pi/4)D^2L\gamma'$ plus a contribution arising from the structure c_3V, in which V equal to the gravity force acting on the structure and c_3 is a dimensionless constant between 0 and 1. On the basis of these assumptions, the equations of horizontal equilibrium and moment equilibrium at the pile head are given by

$$H + (c_3V + \frac{\pi}{4}D^2L\gamma')\sin\varphi_{cr} = \left(d^2 - \frac{1}{2}L^2\right)KD\gamma' \tag{11}$$

$$M - (c_3V + \frac{\pi}{4}D^2L\gamma')L\sin\varphi_{cr} = \frac{1}{3}(L^3 - 2d^3)KD\gamma' \tag{12}$$

respectively. These equations can be combined to eliminate d and give the interaction

equation

$$\left(\frac{1}{2}+\frac{3}{2}\alpha-\frac{3}{2}\frac{M}{L^3KD\gamma'}\right)^2=\left(\frac{1}{2}+\alpha+\frac{H}{L^2KD\gamma'}\right)^3 \tag{13}$$

$$\alpha=\frac{(c_3V+\frac{\pi}{4}D^2L\gamma')\sin\varphi_{cr}}{L^2KD\gamma'} \tag{14}$$

where α is introduced for simplicity. This relation can be rearranged to obtain an expression given entirely in non-dimensional parameters

$$\frac{3}{K}\underbrace{\frac{M}{DL^3\gamma'}}_{\tilde{M}}=\alpha+1\pm2(\frac{1}{2}+\alpha+\frac{1}{K}\underbrace{\frac{H}{L^2D\gamma'}}_{\tilde{H}})^{\frac{3}{2}} \tag{15}$$

$$\alpha=(c_3\underbrace{\frac{V}{L^2D\gamma'}}_{\tilde{V}}+\frac{\pi}{4}\underbrace{\frac{D}{L}}_{1/\eta})\frac{\sin\varphi_{cr}}{K} \tag{16}$$

introducing the pile aspect ratio η and the non-dimensional vertical and horizontal load, $\tilde{V}$ and $\tilde{H}$, respectively. The non-dimensional horizontal load $\tilde{H}$ can be replaced by $\tilde{H}=\tilde{M}/\tilde{e}$. Thus, it follows from equation (15) and (16) that the static moment capacity, in terms of $\tilde{M}$, is uniquely determined by the non-dimensional parameters $\tilde{V}$, $\tilde{e}$ and η. This suggests that the non-dimensional moment-rotation relationship in equation (10) could be written as

$$\tilde{M}=\tilde{k}(\tilde{V},\tilde{e},\eta)\tilde{\theta} \tag{17}$$

Thus, a satisfactory comparison of both stiffness and strength, between laboratory and full-scale tests, is likely to be obtained by plotting $\tilde{M}$ against $\tilde{\theta}$, while keeping $\tilde{V}$, $\tilde{e}$ and η constant. This scaling law derived for monotonic loading is also assumed to cover the cyclic response of stiff piles in sand. The non-dimensional parameters are listed in Table 1.

EXPERIMENTAL EQUIPMENT

A simple and efficient mechanical load rig is used to apply loads to the pile. The rig was originally developed by Rovere (2004) for testing of caisson foundations. The rig consists of a

550x600x600 mm container for sand, a steel frame with pulleys, three weight-hangers and a lever with a driving motor, as illustrated in Fig. 3. The lever is attached to the steel frame through a pivot and carries a motor, which rotates a mass m_1 to cause cyclic loading. The motor is a geared single-phase AC motor rotating at a frequency of 0.106 Hz. The pulley ropes are 3 mm low-stretch spectral ropes.

The load rig is a simple static system. Initially, when $m_1 = m_2 = 0$, the weight of the mass m_3 is chosen to balance any force acting on the lever. Thus, assuming that $\Theta \simeq \pi/2$, as is the case for minor lever deflections, any sinusoidal load in the form $f(t) = f_0 + f_a \sin(\omega t)$ can be applied to the pile by appropriately choosing $m_1 = (l_2/l_a)f_a/g$ and $m_2 = ((l_c/l_a)f_a - f_0)/g$. Since $m_2 > 0$, it follows that l_a or l_c must fulfil the condition $l_a/l_c < f_a/f_0$. The load rig is very stable and can accurately provide a sinusoidal loading for more than 1,000,000 cycles.

The experiments were conducted using unsaturated yellow Leighton Buzzard silica sand. The characteristics of the sand are summarised in Table 2 and further information is given by Schnaid (1990).

The container for the sand was carefully filled by pouring sand from a low drop height to achieve a very loose state. A denser state was also obtained using a hammer drill to vibrate the bottom plate of the sand container.

The tests were conducted using a stiff copper pile. The outer dimensions of the pile are scaled to approximately 1:50, in relation to a typical monopile. The pile properties are listed in Table 3. The pile was driven into the sand by gentle driving with a plastic hammer from a fixed drop height. The number of strokes needed to reach the final penetration depth varied from 460 ± 20 to 740 ± 30 for loose and medium dense sand, respectively. The monopile was fixed horizontally during installation using side supports. Horizontal deflections were

measured by two dial gauges. The load rig is illustrated in Fig. 4.

TEST PROGRAMME

The test programme was designed to investigate the response of the pile and its dependency on the relative density of the sand and the characteristics of the applied cyclic load.

The average relative densities were $R_d = 4\%$ and $R_d = 38\%$, corresponding to a loose and a medium-dense state, respectively. A relationship between effective stress, relative density and peak friction angle for Yellow Buzzard Sand is given by Schnaid (1990) and is used to compare peak friction angles between the laboratory tests and a full-scale monopile. For the calculation it is assumed that a representative effective stress can be taken at $0.8L$ beneath the seabed. Fig. 5 illustrates that the peak friction angles used in the laboratory were estimated as 35^o and 43^o, which equate to field conditions of $R_d = 8\%$ and $R_d = 75\%$, corresponding to a loose and a dense state, respectively.

The characteristics of the applied cyclic load must be uniquely defined. In the following, load levels are referred to in terms of the applied moment M. The corresponding horizontal force follows from $H = M/e$. Two independent parameters are defined to characterise the applied sinusoidal loading

$$\zeta_b = \frac{M_{max}}{M_R} \qquad \zeta_c = \frac{M_{min}}{M_{max}} \tag{18}$$

in which M_R refers to the static moment capacity of the pile and M_{min} and M_{max} are the minimum and maximum in a load cycle. The ratio ζ_b is a measure of the size of the cyclic loading, normalised with respect to the static moment capacity. It follows that $0 < \zeta_b < 1$. The ratio $\zeta_c \in [-1; 1]$ quantifies the characteristics of the cyclic load and takes the value 1 for a static test, 0 for one-way loading and -1 for two-way loading. A visual interpretation of the

load ratios is given in Fig. 6.

Initially, static load tests were performed to determine the static moment capacity in terms of $\widetilde{M}_R$, as shown in Fig. 7. From the moment-rotation curves, is not possible to identify a distinct point of failure. Thus, failure is defined by $\tilde{\theta} = 4^o = 0.0698$rad. The moment-rotation curves in Fig. 7 are for convenience fitted by $\tilde{\theta} \approx 0.038rad \times (\widetilde{M}/\widetilde{M}_R)^{2.33}$ and $\tilde{\theta} \approx 0.042rad \times (\widetilde{M}/\widetilde{M}_R)^{1.92}$ for $R_d = 4\%$ and $R_d = 38\%$, respectively, valid in the range $0.25\widetilde{M}_R < \widetilde{M} < 0.50\widetilde{M}_R$.

It is important to select appropriate values of ζ_b so that the experiments reflect realistic loading conditions. Typical design loads for an offshore wind turbine are shown in Table 4. The limit state *ULS* refers to the ultimate load-carrying capacity and *ULS*/1.35 to the worst expected transient load. *SLS* and *FLS* are the serviceability and fatigue limit states occurring 10^2 and 10^7 times during the lifetime of the wind turbine, respectively. Further information is given by DNV (2004).

The design loads are compared to the laboratory loading, in terms of non-dimensional parameters $\widetilde{M}$ and $\widetilde{H}$, by scaling the design loads such that ULS coincides with the static moment capacity of the laboratory pile. Fig. 8 shows this static capacity, determined from equation (15), compared to the capacities determined from five static load tests in loose sand, conducted at different values of $\tilde{e}$. Also shown on the figure are ranges of ζ_b for $\tilde{e} = 1.19$. The comparison suggests that $30\% < \zeta_b < 50\%$ is the range of primary interest for piles with designs governed by the ULS.

The value of ζ_c is expected to vary between -0.5 and 1 since the response of a wind turbine is governed by large aerodynamical damping, resulting in one-way cycling rather than two-way cycling. For completeness ζ_c was investigated in the full range from -1 to 1. The chosen test programme is summarised in Table 5.

DISCUSSION

The results of the laboratory tests are investigated by plotting the angular rotation of the pile θ in response to the applied moment M for both static and cyclic tests. The method for data extraction is outlined in Fig. 9. The gathered data provides information on both stiffness and accumulated rotation as functions of N, the number of load cycles. The evolution of the accumulated rotation is evaluated in terms of the dimensionless ratio

$$\frac{\Delta\theta(N)}{\theta_s} = \frac{\theta_N - \theta_0}{\theta_s} \tag{19}$$

which expresses the magnitude of the rotation $\Delta\theta(N)$ caused by cyclic loading in terms of the rotation θ_s that would occur in a static test when the load is equivalent to the maximum cyclic load (as defined by $\zeta_b \times M_R$). The non-dimensional stiffness $\tilde{k}$ is obtained substituting measured values of $k = M/\theta$ (see Fig. 9) into equation (10), which is rearranged to give

$$\tilde{k} = \frac{k}{L^{5/2} D \sqrt{p_a \gamma'}} \tag{20}$$

Accumulated displacements

The method proposed by Lin and Liao (1999) suggests that accumulated rotation is proportional to $\ln(N)$. This approach was investigated by plotting $\Delta\theta/\theta_s$ as a function of $\ln(N)$. A good fit was obtained for $N < 100$, but extrapolation beyond $N > 500$ underestimated the accumulated rotation. A better fit was found if the accumulated rotation was modelled as increasing exponentially with N rather than logarithmically, as is in agreement with the method proposed by Little and Briaud (1988) and Long and Vanneste (1994). The exponential behaviour appears as straight lines in double logarithmic axes, as shown on Fig. 10.

The results for one-way loading, plotted in Fig. 10a and 10b, show a very good fit with an exponential expression. The results include approximately 10^4 load cycles whereas the

fatigue limit state is governed by 10^7 load cycles. The closeness of fit up to 10^4 cycles indicates that, in the absence of further experimental data, it might be reasonable to extrapolate to $N = 10^7$. Further data are, of course, required to confirm this hypothesis.

The results obtained by varying ζ_c, plotted in Fig. 10c and 10d, exhibit a more volatile behaviour, particularly for $\zeta_c < 0$. However, the trend in the data also follows the exponential behaviour shown in the one-way load tests. Based on these observations, it is proposed that displacements due to cyclic loading can be predicted by

$$\frac{\Delta\theta(N)}{\theta_s} = T_b(\zeta_b, R_d)T_c(\zeta_c) \cdot N^{0.31} \tag{21}$$

in which T_b and T_c are dimensionless functions, depending on the load characteristics and relative density. The function T_c is defined such that $T_c(\zeta_c = 0) = 1$. The expression in equation (21) was fitted to the data in Fig. 10 (the dotted lines) to empirically determine values T_b and T_c. These values are plotted in Fig. 11 as a function of ζ_b and ζ_c. The behaviour of the functions $T_b(\zeta_b, R_d)$ and $T_c(\zeta_c)$ is clearly apparent, and curves were easily fitted. Generally, the loose sand results in low values of T_b as compared to the denser sand. The value of T_c is found to be independent of relative density.

The T_c-curve in Fig. 11 shows a remarkable result. Clearly, when $\zeta_c = 1$, then T_c must be zero since no accumulated displacement will occur under static load. Also, when $\zeta_c = -1$, then it is expected that T_c will be zero since the force applied is equal in both directions. The maximum one-way load is obtained when $\zeta_c = 0$ and intuitively it seems reasonable to expect that this loading will cause the largest accumulated rotation. This assumption is commonly accepted and the majority of lateral load tests reported in the literature are conducted at $\zeta_c = 0$ and some at $\zeta_c = -1$. However, the results presented here clearly illustrate that loading with $\zeta_c \approx -0.6$ causes an accumulated rotation which is more than 4 times larger than for one-way loading, i.e. $\zeta_c = 0$. The authors are not aware of similar observations in cyclic loading tests,

but clearly this result has profound implications for assessing the results of cycling.

Variation of pile stiffness

Interpretation of the stiffness results involves a greater scatter of the data. This is partly because the measurement of secant stiffness in a cycle involves differences of small displacements. Plotting $\tilde{k}_N$ as a function of $\ln(N)$ indicates that the stiffness evolves approximately logarithmically with cycle number, as shown in Fig. 12. This suggests that the evolution of stiffness can be approximated by

$$\tilde{k}_N = \tilde{k}_0 + A_k \ln(N) \tag{22}$$

where A_k is a dimensionless constant. It is observed from Fig. 12 that all slopes are almost equal. This suggests that A_k is independent of both relative density and load characteristics within the observed range. The expression in equation (22) was fitted to the data in Fig. 12 (the dotted lines) using the value $A_k = 8.02$ and values of $\tilde{k}_0$ were determined from the point of intersection with the $\tilde{k}$-axis where $N = 1$. The empirically determined values of $\tilde{k}_0$ can be expressed by

$$\tilde{k}_0 = K_b(\zeta_b) K_c(\zeta_c) \tag{23}$$

in which K_b and K_c are dimensionless functions, depending on the load characteristics and relative density. The function K_c is defined such that $K_c(\zeta_c = 0) = 1$. The empirically determined values of K_b and K_c as functions of ζ_b and ζ_c, respectively, are illustrated in Fig. 13. The behaviour of the functions $K_b(\zeta_b)$ and $K_c(\zeta_c)$ was easily determined and curves fitted. It is not possible to make a clear distinction between the results for $R_d = 4\%$ and $R_d = 38\%$. This indicates that values of stiffness are somewhat independent of the relative density, at least for the low to medium densities tested. However, this is unlikely to hold for $R_d \to 100\%$ since no increase in stiffness is expected for sand in its densest state.

The most important outcome of the results is that stiffness always tends to increase. This

observation opposes the current methodology of degrading static $p-y$ curves to account for cyclic loading.

Example

An example is given to demonstrate the use of the proposed methods. Consider a stiff monopile, $L = 18$ m and $D = 4$ m, driven into sand with a friction angle of 35^0. The task is to determine the increase in stiffness and accumulated rotation due to 10^7 load cycles characterised by $\zeta_b = 0.3$ and $\zeta_c = -0.2$.

Initially, values of θ_s and $\tilde{k}_0$ must be determined. These can be calculated by various methods, for example using $p-y$ curves, finite element models or alternatively, using the non-dimensional framework which has been presented here. The non-dimensional approach requires that the full-scale structure and laboratory pile have comparable values of $\tilde{\eta}$, $\tilde{V}$ and $\tilde{e}$, as is the case in this example. The non-dimensional static rotation for $\zeta_b = 0.3$ gives a non-dimensional moment of $\widetilde{M} = 0.3 \times \widetilde{M}_R = 0.3 \times 0.6 = 0.18$ at which point the non-dimensional rotation is $\tilde{\theta}_s = 0.0023$. The corresponding static rotation of the full-scale monopile follows from the definition of $\tilde{\theta}$ which gives $\theta_s = 0.0033$. The initial non-dimensional stiffness is determined from equation (23), by evaluating K_b and K_c from Fig. 13, to obtain $\tilde{k}_0 = 240 \times 0.9 \approx 216$. The non-dimensional stiffness can optionally be transformed to the absolute value of the full-scale stiffness using the relationship in equation (20).

Given θ_s and $\tilde{k}_0$, it is possible to estimate the accumulated rotation and stiffness change due to long-term cyclic loading. Values of T_b and T_c are determined from Fig. 11 with the representative relative density chosen as $R_d = 4\%$ since the angle of friction is 35^o. The resulting increase in stiffness follows from equation (22)

$$\tilde{k}_N = \tilde{k}_0 + 8.02\ln(10^7) \approx 345 \quad \Rightarrow \quad \frac{\tilde{k}_N - \tilde{k}_0}{\tilde{k}_0} = 60\% \tag{24}$$

This result indicates that the stiffness can be expected to increase by approximately 60% during the lifetime of the wind turbine. The accumulated rotation follows from equation (21)

$$\frac{\Delta\theta}{\theta_s} = 0.047 \times 1.5 \times (10^7)^{0.31} \approx 10.4 \quad \Rightarrow \quad \Delta\theta = 0.0344 \text{ rad } (\approx 2^o) \tag{25}$$

The accumulated rotation is estimated to be 2 degrees which is a value that would breach the tolerance criterion. It should be noted that the accumulated rotation is calculated on the basis of 10^7 load cycles, acting in the same direction. Less rotation must be expected, since the actual loading would be multi-directional. Of course, if ζ_b is in the range between -0.7 and -0.4, then much higher rotation is predicted.

If the monopile is more conservatively designed, say by using a static design capacity equal to 1.5 times ULS, then ζ_b will be approximately 0.2. In this case, the predicted accumulated rotation and increase in stiffness are 0.27^o and 42%, respectively.

CONCLUSION

A series of tests were conducted on small-scale driven piles subjected to long-term cyclic loading. A typical design of a monopile was adopted and used to quantify realistic pile dimensions and loading ranges. Furthermore, a complete non-dimensional framework for stiff piles in sand is presented and applied to interpret the test results.

The accumulated rotation of a stiff pile is largely affected by the characteristics of the applied cyclic load. Thus, parameters characterizing the load, other than maximum load levels, are required for accurate predictions. For example, results for one-way loading were found to differ by a factor of four as compared to two-way loading. A very significant result was that the most onerous loading condition was found to be between one way and two way loading. A

method to predict the accumulated rotation during the lifetime of an offshore wind turbine foundation is presented. When applied, the method predicts that typical tolerances for accumulated rotation are breached if the foundation is designed so that the design capacity is equal to the ULS load. This suggests that considerations of accumulated rotation are the primary design driver. The proposed method does not account for multi-directional loading, which is likely to be less severe in terms of accumulated rotation, as compared to uni-directional loading.

The tests showed that cyclic loading always increased the pile stiffness and the increase was found to be independent of relative density. This contrasts with the current methodology of degrading static $p-y$ curves to account for cyclic loading. A method, based on the experimental work carried out, is presented to predict changes in stiffness due to long-term cyclic loading.

The results in this paper lay out a basic framework to incorporate effects of cyclic loading in a simple manner. Further work should be carried out to investigate piles installed in very dense sand, the effect of altering pile dimensions and how a representative cyclic load is chosen. The effect of the loading frequency on the drained response of laterally loaded piles in sand is limited. However, due to the scale of field monopiles it is possible that the response in saturated sand may not be completely drained and further work on the effects of loading frequency will need to be undertaken. Finally, comparisons to full-scale measurements should be carried out to ensure that the proposed methods are reliable and valid.

REFERENCES

API. (1993). *Recommended practice for planning, designing, and constructing fixed offshore platforms - working stress design*. American Petroleum Institute, Washington, RP2A-WSD: 20 edition.

Briaud, J. L., Smith, T. D., and Meyer, B. J. (1984). Using pressuremeter curve to design laterally loaded piles. *Proc. of the 15th annual offshore tech. conf.,* Houston, Paper No. 4501.

Broms, B. B. (1964). Lateral resistance of piles in cohesionless soils. *J. Soil Mech. Found. Eng. Div*. **90**, No.3, 123–156.

Budhu, M. and Davies, T. (1987). Nonlinear analysis of laterally loaded piles in cohesionless soils. *Canadian Geotech. J.* **24**, no.2, 289–296.

Carter, J. and Kulhawy, F. (1988). *Analysis and design of drilled shaft foundation socketed into rock*. Cornell University, Ithaca, New York.

Cox, W. R., Reese, L., and Grubbs, B. R. (1974). Field testing of laterally loaded piles in sand. *Proc. of the Offshore Tech. Conf.,* Houston, Paper no. 2079.

DNV (1977). *Rules for the design, construction and inspection of offshore structures.* Det Norske Veritas, Hovek, Norway.

DNV (2004). *Offshore standard: Design of offshore wind turbine structures.* Det Norske Veritas, Hellerup, Denmark, DNV-OS-J101.

Dobry, R., Vincente, E., O'Rourke, M., and Roesset, J. (1982). Stiffness and damping of single piles. *J. of Geotech. Engng*. **108**, No. 3, 439–458.

Kelly, R. B., Houlsby, G. T., and Byrne, B. W. (2006). A comparison of field and laboratory tests of caisson foundations in sand and clay. *Geotechniqué* **56**, No. 9, 617–626.

Lesny, K. and Hinz, P. (2007). Investigation of monopile behaviour under cyclic lateral loading. *Proc., Offshore Site Investigation and Geotechnics*, London, 383–390.

Lin, S. S. and Liao, J. C. (1999). Permanent strains of piles in sand due to cyclic lateral loads. *J. of Geotech. and Geoenv. Engng* **125**, No. 9, 798–802.

Little, R. L. and Briaud, J. L. (1988). *Cyclic Horizontal Load Tests on 6 Piles in Sands at Houston Ship Channel.* Research Report 5640 to USAE Waterways Experiment Station, Civil Engineering, Texas A&M University

Long, J. and Vanneste, G. (1994). Effects of cyclic lateral loads on piles in sand. *J. of Geotech. Engng.* **120**, No. 1, 225–244.

McClelland, B. and Focht, J. (1958). Soil modulus for laterally loaded piles. *Transactions, ASCE* **123**, 1049–1086.

Murchison, J. M. and O'Neill, M. W. (1984). Evaluation of p-y relationships in cohesionless soils. *Proc., Symposium of Analysis and Design of Pile Foundations, ASCE,* San Francisco, 174–191.

O'Niell, M. W. and Murchison, J. M. (1983). An evaluation of p-y relationships in sands. Dept. of Civ. Engrg., Univ. of Houston, Houston, Research Rep. No. GT-DF02-83.

Park, C. S. and Tatsuoka, F. (1994). Anisotropic strength and deformation of sands in plane strain compression. *Proc. XIII Int. Conf. on SMFE,* New Delhi, **1**, 1–6.

Peng, J. R., Clarke, B., and Rouainia, M. (2006). A device for cyclic lateral loaded model piles. *Geotech. Testing J.* **29**, No. 4, 1–7.

Porovic, E. and Jardine, R. J. (1994). Some observations on the static and dynamic shear stiffness of ham river sand. *Proc. IS-Hokkaido, Balkemna,* Rotterdam, **1**, 25–30.

Poulos, H. and Hull, T. (1989). The role of analytical geomechanics in foundation engineering. *Foundation Engng.: Current principles and Practices, ASCE,* Reston, **2**, 1578–1606.

Reese, L., Cox, W. R., and Koop, F. D. (1974). Analysis of laterally loaded piles in sand. *Proc., 6th Offshore Tech. Conf.*, Houston, **2**, Paper No. 2079.

Reese, L. and Matlock, H. (1956). Nondimensional solutions for laterally loaded piles with soil

modulus assumed proportional to depth. *Proc., 8th Conf. on Soil Mech. and Found. Eng.*, University of Texas, Austin, Special Publication No. 29.

Reese, L. C. and Impe, W. F. (2001). *Single Piles and Pile Groups Under Lateral Loading.* Taylor & Francis, London.

Rovere, M. (2004). *Cyclic loading test machine for caisson suction foundations.* Tech. report, Ecole Centrale de Lille - Politecnico di Milano, Milano.

Schnaid, F. (1990). *A study of the cone-pressuremeter test in sand*. Ph.D thesis, University of Oxford.

Simpson, B. (2002). Engineering needs. In *Pre-failure Deformation Characteristics of Geomaterial* (Jamiolkowski, Lancellotta & Lo-Presti (ed.)), Swets & Zeitlinger, Torino, pp. 1011–1026.

Wroth, C. P. and Houlsby, M. F. (1985). Soil mechanics: Property characterisation and analysis procedures. *Proc., 11th Int. Conf. Soil Mech. Found. Engng.*, San Francisco, 1–50.

Wroth, C. P., Randolph, M. F., Houlsby, G. T., and Fahey, M. (1979). *A review of the engineering properties of soils with particular reference to the shear modulus.* Report CUED/D-SOILS TR75, University of Cambridge.

NOTATION

The following symbols are used in this paper:

c_1, c_2, c_3	dimensionless constants (-);
d	pile pivot point (m);
D	pile diameter (m);
D_{10}, D_{60}	particle sizes (mm);
e	load eccentricity (m);
E_p	elastic modulus of the pile (Pa);
E_s	elastic modulus of the soil (Pa);
f, f_0, f_a	load rig forces (N);
g	gravitational acceleration (m/s^2);
G	shear modulus (Pa);
G_s	specific gravity (-);
H	horizontal load at seabed (N);
I_p	moment of inertia of the pile (m^4);
k_1, k_2, k_3	dimensionless parameters (-);
k	pile stiffness (Nm/rad);
k_0	pile stiffness in first cycle (Nm/rad);
k_N	pile stiffness in N'th cycle (Nm/rad);
K	Broms factor (-);
K_b, K_c	dimensionless functions (-);
l_2, l_a, l_c	load rig dimensions (m);
L	penetration depth of pile (m);
m_1, m_2, m_3	load rig masses (kg);
M, M_{min}, M_{max}	moment at seabed (Nm);
M_R	static moment resistance of pile (Nm);
N	number of load cycles (-);
p_a	atmospheric pressure (Pa);

p'	effective isotropic stress (Pa);
R_d	relative density (%);
t	time (s);
T_b, T_c	dimensionless functions (-);
V	gravity force acting on the structure (N);
y	horizontal deflection (m);
z	depth below seabed (m);
α	dimensionless parameter (-);
$\gamma_{min}, \gamma_{max}$	dry unit weight (kN/m^3);
γ'	effective unit weight (kN/m^3);
ω	rotational frequency (Hz);
φ	angle of friction (^{o})
φ_{cr}	critical state angle of friction (^{o})
σ'_v	effective vertical stress (Pa);
θ	pile rotation (rad);
θ_0	pile rotation in first cycle (rad);
θ_N	pile rotation in N'th cycle (rad);
θ_s	static pile rotation (rad);
ζ_b, ζ_c	load characteristic parameters (-);

Note: "$\sim$" is used above parameters when reference is made to their corresponding dimensionless values, see Table 1.

TABLES

Moment loading:	$\widetilde{M} = M/L^3 D\gamma'$
Vertical force:	$\tilde{V} = V/L^2 D\gamma'$
Horizontal force:	$\widetilde{H} = H/L^2 D\gamma'$
Rotation: degrees	$\tilde{\theta} = \theta\sqrt{p_a/L\gamma'}$
Load eccentricity:	$\tilde{e} = M/HL$
Aspect ratio:	$\eta = L/D$

Table 1: Non-dimensional parameters

Particle sizes, $D_{10}/D_{30}/D_{50}/D_{60}$: mm	0.63/0.70/0.80/0.85
Specific gravity, G_s:	2.65
Minimum dry unit weight, γ_{min}: kN/m^3	14.65
Maximum dry unit weight, γ_{max}: kN/m^3	17.58
Critical angle of friction, φ_{cr}: degrees	34.3

Table 2: Characteristics of yellow Leighton Buzzard Sand (Schnaid 1990)

Pile diameter, D: mm	80.0
Wall thickness: mm	2.0
Penetration depth, L: mm	360.0
Load eccentricity, e: mm	430.0
Pile weight, V: N	35.0

Table 3: Properties of the copper monopile

	N -	M (MNm)	H (MN)	V (MN)
ULS	1	95	4.6	5.0
ULS/1.35	1	70	3.4	5.0
SLS	10^2	45	2.0	5.0
FLS	10^7	28	1.4	5.0

Table 4: Typical design loads for a 2MW turbine

No.	Type	$\tilde{e}$	R_d	φ	ζ_b	ζ_c	N
1	Static	0.10	4%	35^o	-	-	-
2	Static	0.42	4%	35^o	-	-	-
3	Static	0.78	4%	35^o	-	-	-
4	Static	1.19	4%	35^o	-	-	-
5	Static	3.33	4%	35^o	-	-	-
6	Cyclic	1.19	4%	35^o	0.20	0	8200
7	Cyclic	1.19	4%	35^o	0.27	0	18200
8	Cyclic	1.19	4%	35^o	0.34	0	8400
9	Cyclic	1.19	4%	35^o	0.40	0	17700
10	Cyclic	1.19	4%	35^o	0.53	0	8600
11	Cyclic	1.19	4%	35^o	0.40	-0.98	8510
12	Cyclic	1.19	4%	35^o	0.40	-0.67	7400
13	Cyclic	1.19	4%	35^o	0.40	-0.33	8800
14	Cyclic	1.19	4%	35^o	0.40	0.33	65370
15	Static	1.19	38%	43^o	-	-	-
16	Cyclic	1.19	38%	43^o	0.27	0	8090
17	Cyclic	1.19	38%	43^o	0.40	0	7423
18	Cyclic	1.19	38%	43^o	0.52	0	17532
19	Cyclic	1.19	38%	43^o	0.40	-0.50	9003
20	Cyclic	1.19	38%	43^o	0.40	-0.80	9814
21	Cyclic	1.19	38%	43^o	0.40	0.50	9862

Table 5: Test programme

FIGURES

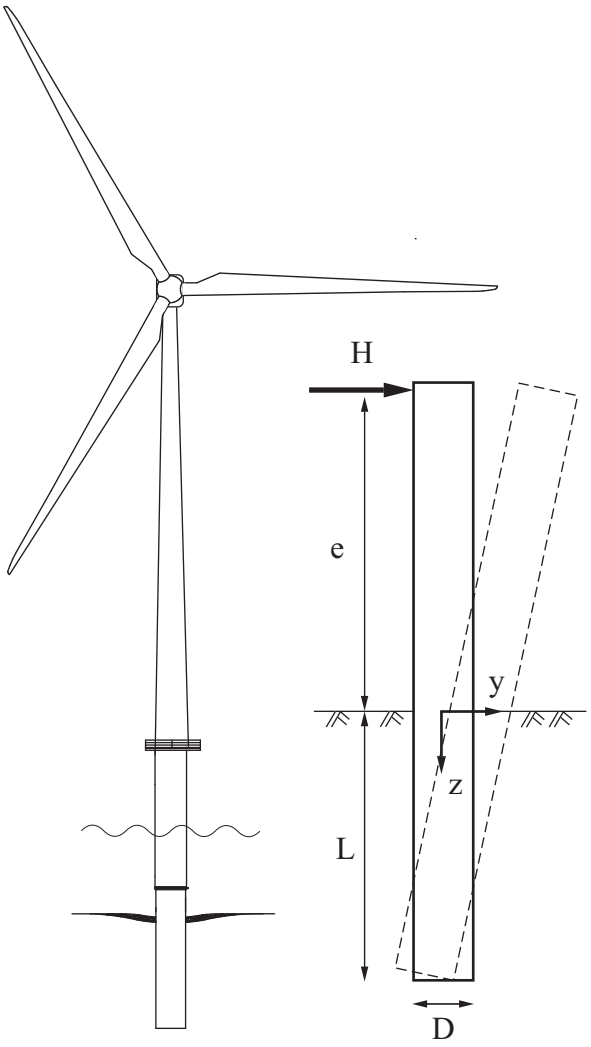

Figure 1: A typical offshore wind turbine installed on a monopile foundation

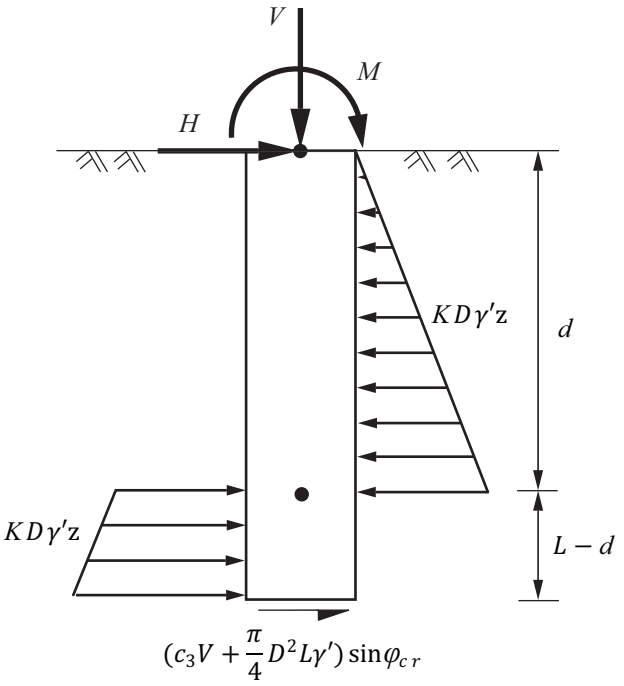

Figure 2: Horizontal stress distribution in the ultimate limit state for a laterally loaded stiff pile in sand

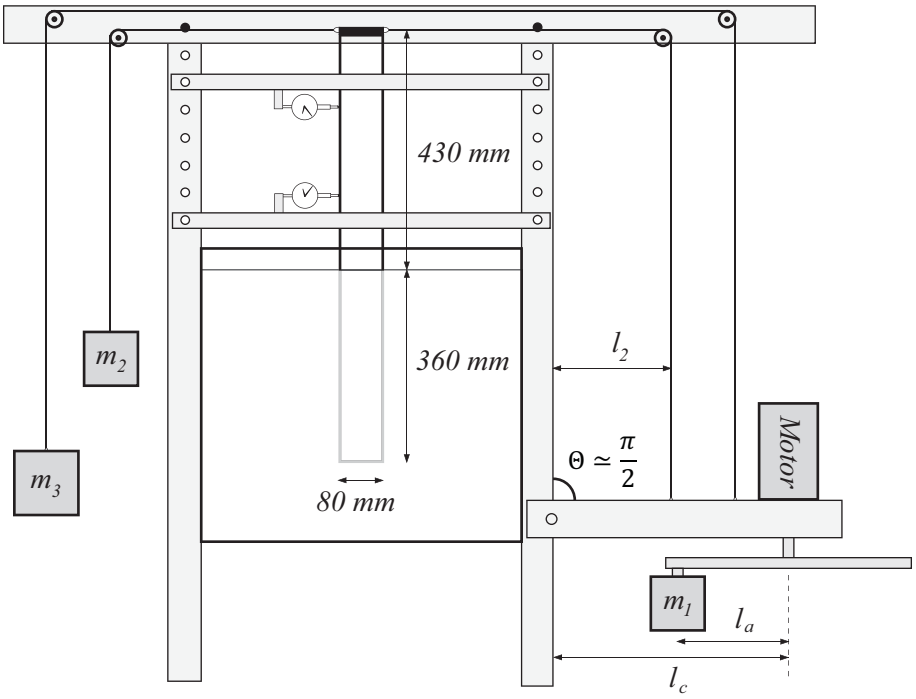

Figure 3: Mechanical load rig used to investigate the response of stiff piles to long-term cyclic loading

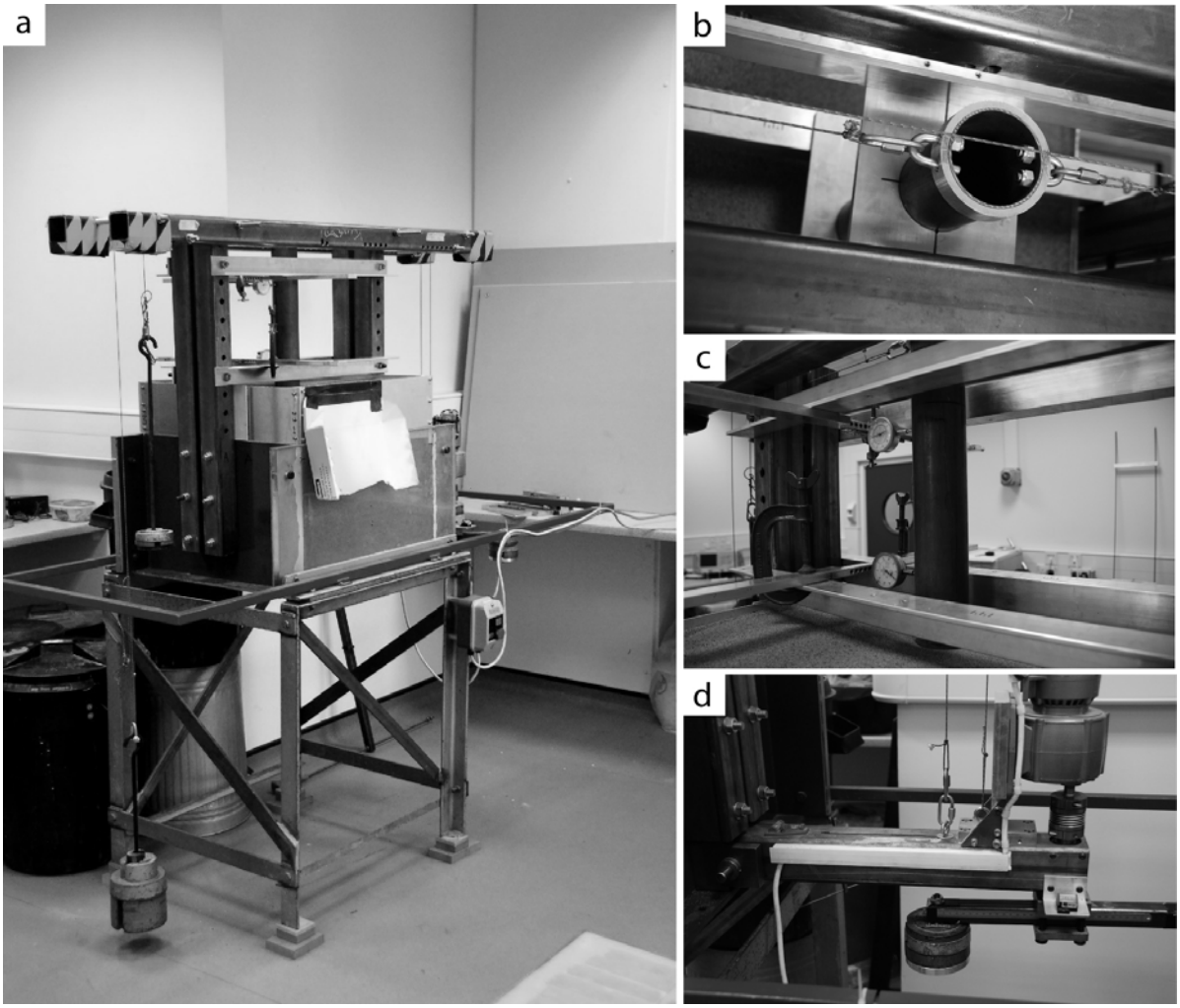

Figure 4: Experimental setup: a) Mechanical load rig. b) Side supports used during installation. c) Installed pile with two dial gauges measuring horizontal deflections. d) Driving motor

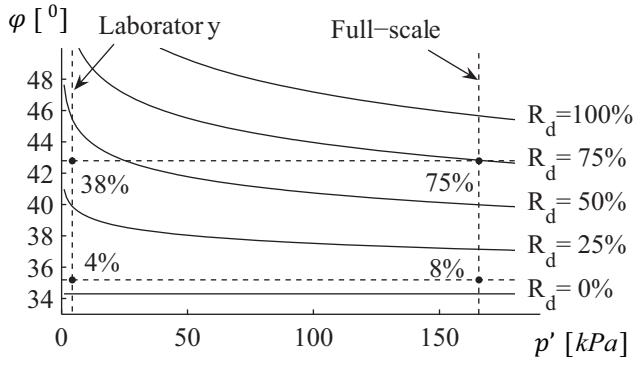

Figure 5: Friction angles of yellow Leighton Buzzard Sand as function of the effective isotropic stress p' and relative density R_d

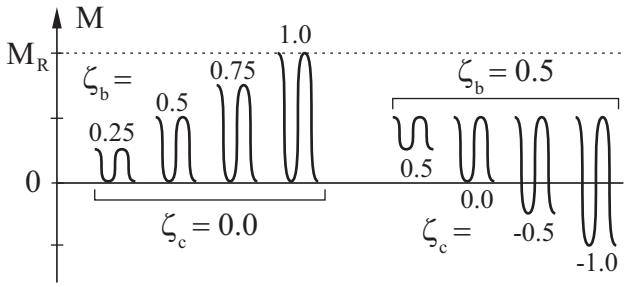

Figure 6: The characteristics of cyclic loading defined in terms of ζ_b and ζ_c

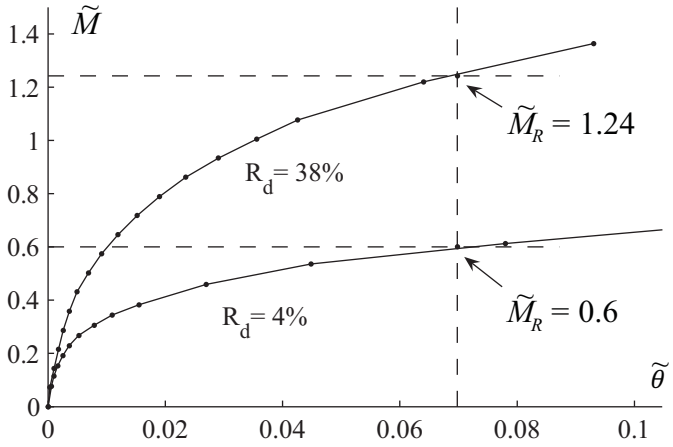

Figure 7: Moment capacity determined from static load tests for $\tilde{e} = 1.19$

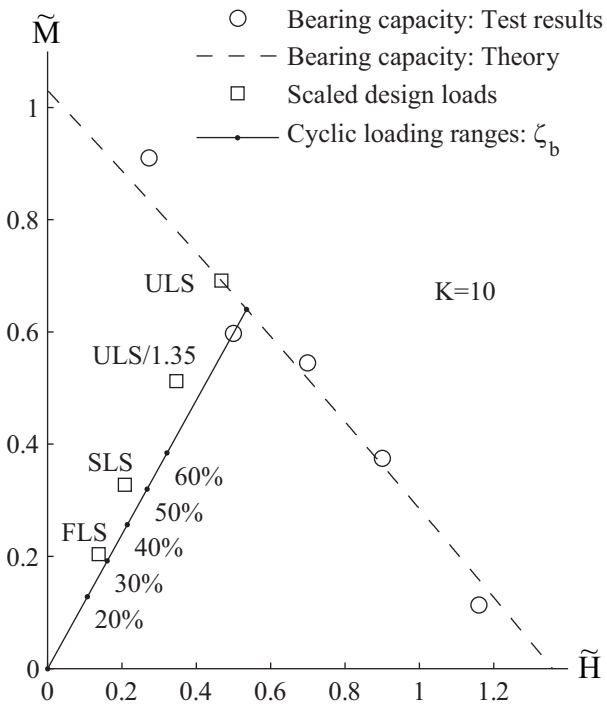

Figure 8: Cyclic loading ranges, in terms of ζ_b, in relation to design loads of typical an offshore wind turbine

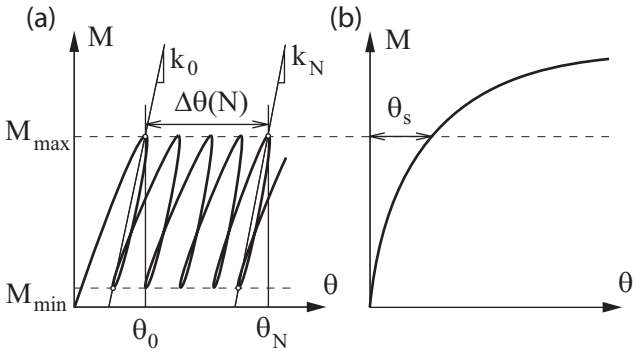

Figure 9: Method for determination of stiffness and accumulated rotation.

(a) Cyclic test (b) Static test

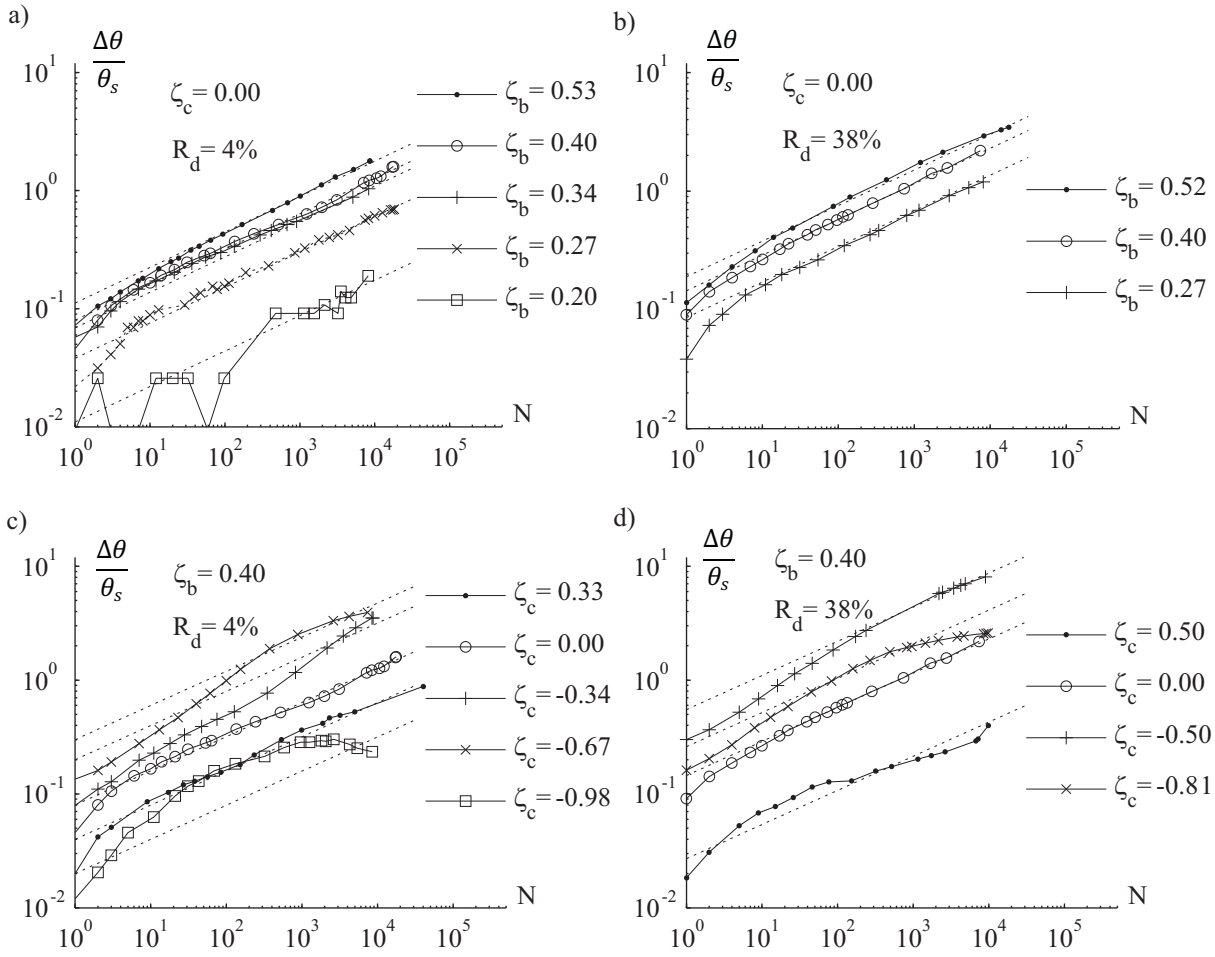

Figure 10: Measured displacements as a function N, R_d, ζ_b and ζ_c.

The dotted lines are obtained using equation (21)

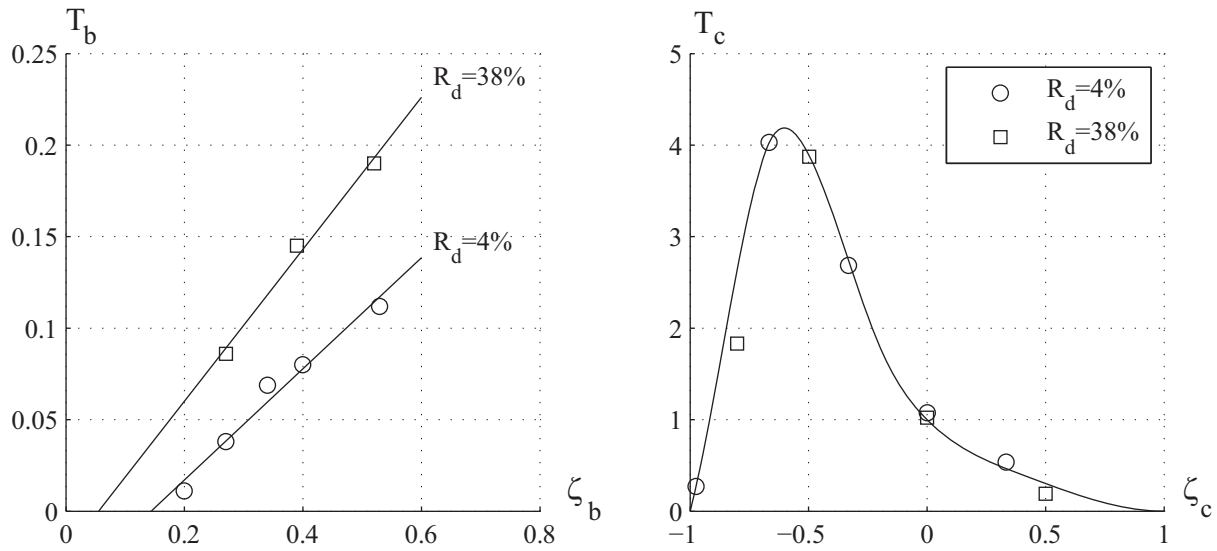

Figure 11: Functions relating T_b and T_c to the relative density, R_d, and the characteristics of the cyclic load in terms of ζ_b and ζ_c

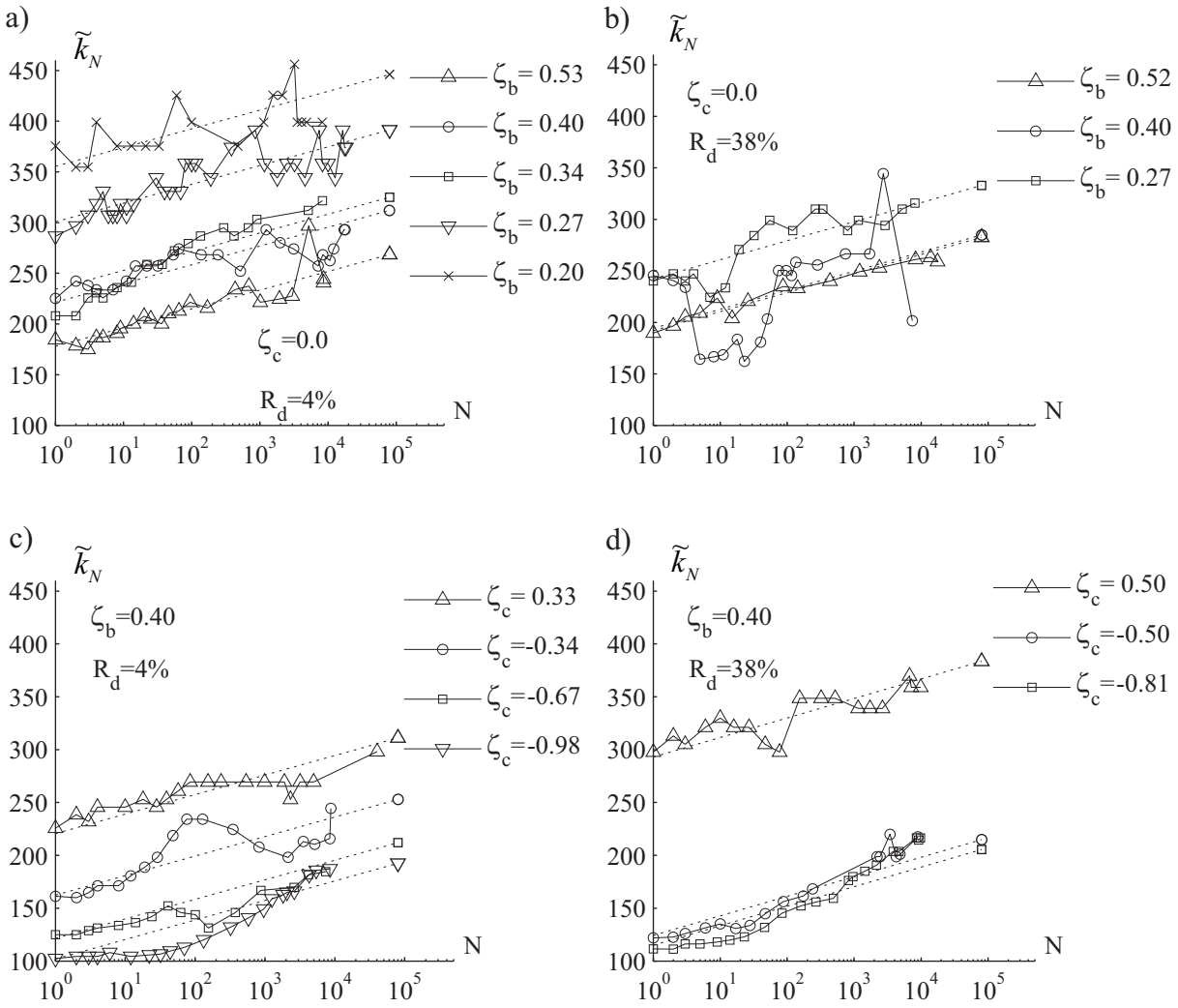

Figure 12: Measured stiffness as a function N, R_d, ζ_b and ζ_c.

The dotted lines are obtained using equation (22)

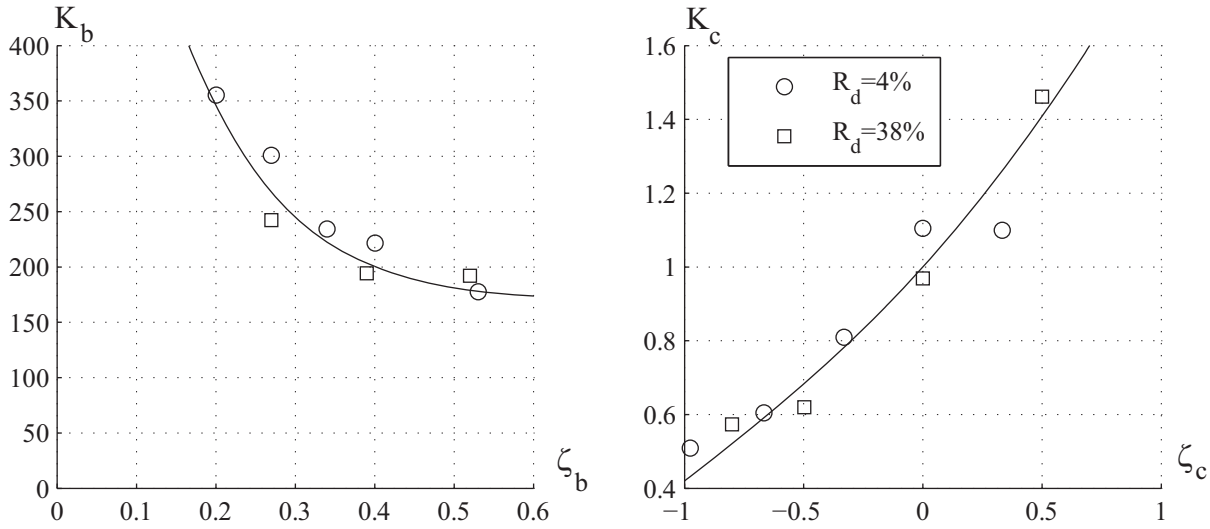

Figure 13: Values of K_b and K_c as a function of the relative density, R_d, and the characteristics of the cyclic load in terms of ζ_b and ζ_c

PAPER II

LeBlanc, C., Byrne, B. W. & Houlsby, G. T.

Response of stiff piles to random two-way lateral loading

Submitted for publication.

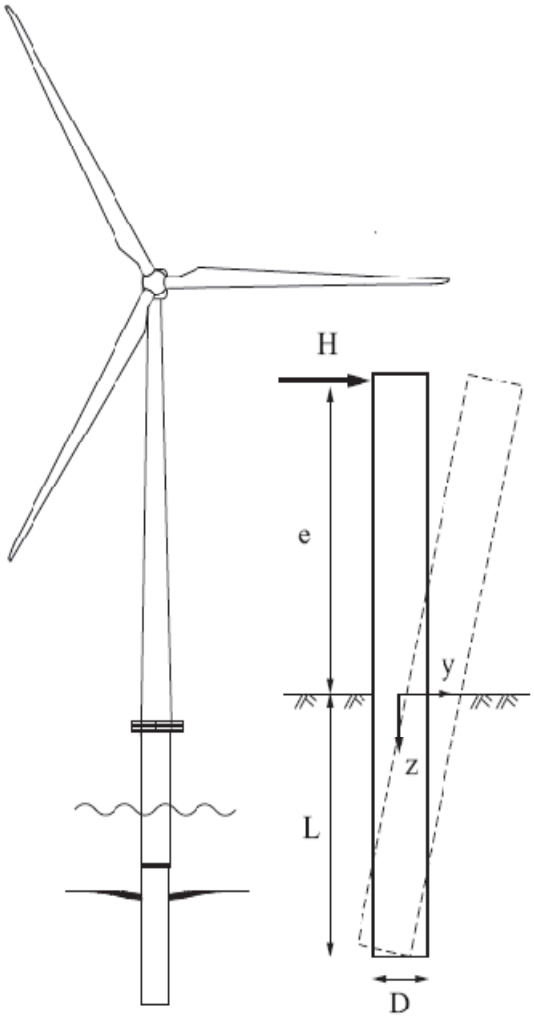

Loading of an offshore wind turbine

Response of stiff piles to random two-way lateral loading

Christian LeBlanc[1], and Byron W. Byrne[2] and Guy T. Houlsby[3]

1) Ph.D. research student, Dept. of Civil Engineering, Aalborg University & Dept. of Offshore Technology, DONG Energy, A.C.Meyers Vænge 9, 2450 Copenhagen SV, Denmark. Phone: (+45) 9955 2558. E-mail: chrle@dongenergy.dk.

2) University Lecturer in Civil Engineering, Dept. of Engineering Science, Parks Rd., Oxford OX1 3PJ, UK.

3) Professor of Civil Engineering, Dept. of Engineering Science, Parks Rd., Oxford OX1 3PJ, UK.

Keywords: Piles, Repeated loading, Laboratory tests, Sands, Settlement

Date written: 11.09.2008

Date revised: -

Number of words: 1971

Number of figures: 10

Number of tables: 3

Abstract:

A model for predicting the accumulated rotation of stiff piles under random two-way loading is presented. The model is based on a strain superposition rule similar to Miner's rule and uses rainflow-counting to decompose a random time-series of varying loads into a set of simple load reversals. The method is consistent with that proposed by LeBlanc *et al.* (2008) for predicting the response of piles to continuous long-term cyclic loading. The validity of the model is supported by 1-*g* laboratory tests where a stiff pile, installed in drained sand, is subjected to a series of 10-10000 load cycles with varying amplitude and mean load. Finally an example is given for an offshore wind turbine indicating that accumulated pile rotation during the life of the turbine is dominated by the worst expected load.

1. Introduction

Typical foundations for offshore windfarms are 'monopiles': large diameter ($4 - 6$ m) piles installed $15 - 30$ m into the seabed. Fig. 1 shows a typical offshore wind turbine on a monopile foundation. Whilst the static lateral capacity of the monopile is important, a safe design must also consider accumulated rotation during the wind turbine lifetime. Design guidance on this issue is currently limited.

Design of laterally loaded piles is usually based on the use of non-linear *p-y* curves as introduced by Reese and Matlock (1956) and McClelland and Focht (1958). For piles in sand the work by Reese *et al.* (1974) and O'Niell and Murchison (1983) led to DNV recommendations (2004) for design of monopiles, as typically used by the offshore wind industry. These recommendations are primarily based on two full-scale tests reported by Cox *et al.* (1974) and address the ultimate moment capacity of the pile. There is, however, limited design guidance for prediction of accumulated rotation under long-term variable-amplitude cyclic loading.

Long and Vanneste (1994), using work by Little and Briaud (1988), accounted for cyclic loading of piles by reducing the static soil reaction modulus to degrade the static *p-y* curves. More recently LeBlanc *et al.* (2008) describe a method for predicting accumulated pile rotation in response to continuous long-term cyclic loading on the basis of 1-*g* laboratory tests. These simple methods estimate the effect of continuous cyclic loads on the piles, but methods considering random loading are limited. Stewart (1986) proposed a method to superpose strains in triaxial tests on the basis of damage in a similar way to Miner's rule (Miner, 1948). Lin and Liao (1999) then adopted this concept of strain superposition to

predict the accumulated deflection of piles under variable-amplitude cyclic lateral loading. Their method assumes that strain accumulation evolves logarithmically with the number of cycles (*N*), which contrasts with the work of Little and Briaud (1988), Long and Vanneste (1994) and LeBlanc *et al.* (2008) where the accumulation of pile rotation increases as a power function of *N*. Lesny and Hinz (2007) provide a more theoretical approach, predicting accumulated pile rotation using data from cyclic triaxial tests and a finite element model incorporating Miner's rule.

This note describes a model for predicting accumulated pile rotation under random two-way lateral loading. The proposed method is based on Miner's rule and is consistent with that proposed by LeBlanc *et al.* (2008) for piles under continuous long-term cyclic loading. The basis for the model is supported by 1-*g* laboratory tests where a stiff pile, installed in sand, was subjected to 10-10000 cycles of varying amplitude and mean load. The tests were conducted at a scale of 1:50 of a typical monopile with properties shown in Table 1. A mechanical rig was used to apply loading, and horizontal pile deflections were measured at two levels using both dial gauges and displacement transducers. The experiments were conducted in unsaturated yellow Leighton Buzzard 14/25 sand in a loose ($R_d = 4\%$) or a medium-dense state ($R_d = 38\%$). LeBlanc *et al.* (2008) describe in detail the equipment and test procedures.

2. Cyclic Loading of Piles

(a) Continuous Cyclic Loading

Horizontal loads H acting at distance e above the seabed result in seabed moments $M = e \times H$. The cyclic loading is characterized in terms of two parameters, $\zeta_b = M_{max}/M_R$ and

$\zeta_c = M_{min}/M_{max}$, in which M_R is the static moment pile capacity, while M_{min} and M_{max} are the minimum and maximum values during the load cycle (Fig. 2). LeBlanc *et al.* (2008) show that the pile rotation θ, in terms of θ_0 and $\Delta\theta$ (as defined in Fig. 3), can be predicted by

$$\theta = \theta_0 + \Delta\theta(\mathrm{N}) \quad (1)$$

where

$$\Delta\theta(N) = (T_b \times T_c \times N^{\alpha}) \times \theta_s \quad (2)$$

$T_b = T_b(\zeta_b, R_d)$ and $\mathrm{T_c} = \mathrm{T_c}(\zeta_c)$ are dimensionless multipliers and θ_s is the rotation that would occur in a static test when $M = \zeta_b \times M_R$. The characteristics of the loading (ζ_c) were found to affect the cyclic behavior significantly. The value $\alpha = 0.30$ was empirically determined.

The measured response and predictions using equation (1) and (2) are shown in Fig. 4 for piles under three types of continuous cyclic loading. The input parameters for load regimes A, B and C are listed in Table 2. The difference of θ_s and θ_0 is due to θ_s being determined from a separate static test whilst θ_0 comes from the much more rapid cyclic test.

(b) Influence of Load Sequence

Relationships based on Miner's rule assume that damage is independent of the loading sequence. For sands accumulation of strains may be interpreted as material damage. Stewart (1986) assesses this and reports that in triaxial tests on sand samples the accumulated strains were not affected by the loading sequence. Fig. 5 shows results from two tests carried out to assess the accumulation of pile rotation (the Figure shows envelopes of rotation). In the first test, the applied loads were 10^4 cycles of type A, 100 cycles of type B and finally 10 cycles

of type C. The order of loading was reversed in the second test. The post-cycling accumulated pile rotation is assessed for $M = 0$ to avoid the effects of elastic strains. The resulting accumulated pile rotation was found to differ by only $\Delta\theta = 1.4\%$ suggesting that accumulated pile rotation is independent of loading sequence.

(c) Strain Superposition

The cumulative pile rotation due to a mix of cyclic loads can be handled using a superposition method consistent with the approach of LeBlanc *et al.* (2008) and Miner's rule. The basic procedure assumes that the accumulated rotation induced by N_a cycles of type "a" can be obtained equivalently by N_b^0 cycles of type "b", where N_b^0 is referred to as the equivalent number of cycles. Consider the accumulated rotation $\Delta\theta_a$ in response to N_a cycles of type "a" which is given by equation (2) as:

$$\Delta\theta_a = (\theta_s T_b T_c)_a \times (N_a)^{\alpha} \quad (3)$$

Alternatively $\Delta\theta_a$ might have been obtained by applying cycles of type "b" with the required number given by:

$$N_b^0 = \left(\frac{\Delta\theta_a}{(\theta_s T_b T_c)_b}\right)^{\frac{1}{\alpha}} \quad (4)$$

If N_b cycles of type "b" are then applied subsequent to N_a cycles of type "a" the resulting accumulated rotation may be evaluated by equation (2) as

$$\Delta\theta_b = (\theta_s T_b T_c)_b \times \left(N_b^0 + N_b\right)^{\alpha} \quad (5)$$

and the total pile rotation according to equation (1) by

$$\theta_b = \Delta\theta_b + \max\left[\theta_{0,a}, \theta_{0,b}\right] \quad (6)$$

Fig. 6 shows the superposition approach diagrammatically. The proposed method is consistent with the assumption that the accumulated rotation is independent of loading sequence.

Figs. 7 and 8 show measured and predicted pile rotation in response to the load sequence $1000 \times \mathrm{A} \rightarrow 1000 \times \mathrm{B} \rightarrow 1000 \times \mathrm{C}$. The theory predicts the cumulative pile rotation closely, with the difference between predicted and measured pile rotations less than 6%.

(d) Effect of Load Reversal

The above method does not address the effect of load reversals. Consider the cyclic load of type "a" defined in terms of ζ_b and ζ_c. The cyclic load defined by $-\zeta_b$ and ζ_c is equivalent to "a" but acts in the opposite direction and is denoted "-a". Fig. 9 shows pile rotations under the loading sequence $(N \times \mathrm{B}) \rightarrow (N \times -\mathrm{B}) \rightarrow (5N \times \mathrm{B})$ in which a load reversal is applied. It is found that $2.51 \times N$ cycles are required to neutralize the effect of the loading reversal so that the accumulated rotation is equal to the rotation prior to the reversed loading. This test was repeated for medium-dense sand where $1.96 \times N$ cycles were required to neutralize the effect of reversed loading.

The results indicate that a conservative approach might assume that at least $1 \times N$ cycles are needed to neutralize the reversed loading. This leads to the approach where it is only necessary to subtract the number of reversed load cycles. Suppose that a load time series is decomposed into $N_a(\zeta_b > 0)$ cycles of type "a" and $N_a(\zeta_b < 0)$ cycles of type "−a". If "a" is the dominant load direction the resulting accumulated rotation can be estimated by using

the net cycles in that direction (*i.e.* $N_a = N_a(\zeta_b > 0) - N_a(\zeta_b < 0)$ in the direction of "a").

e) Extended Rainflow-Counting

Rainflow-counting is commonly applied to assess fatigue life of structures. The method decomposes a time-series of varying loads into a set of load reversals so that Miner's rule can be applied. This method can be applied to the analysis of accumulated pile rotation. The method counts the number of half load reversals specified only in terms of amplitude, thus it is necessary to extend the method to include the mean load of each load reversal. An extended rainflow-counting procedure, based on a procedure by Rychlik (1987), is used to decompose a load time-series into a set of load reversals defined in terms of ζ_b and ζ_c (illustrated in Fig. 10).

3. Calculation Approach

The above leads to a methodology for predicting accumulated pile rotation under random two-way loading based on 5 assumptions:

(1) The accumulation of pile rotation under continuous cyclic loading evolves according to equations (1) and (2).

(2) The order of cyclic loading is irrelevant, thus, any load series may be rearranged into a convenient series of cyclic loading (section 2b).

(3) Load cycles can be superposed (section 2c).

(4) Reversed load cycles can be accounted for by subtraction (section 2d).

(5) A rainflow-counting method can be used to decompose a time series of varying loads into a set of load reversals (section 2e).

The method requires the values $(T_b, T_c, N, \theta_0)_i$ to be determined for each type i of simple load reversal, characterized by $(\zeta_b, \zeta_c)_i$ where $\zeta_b \in [0;\ 1]$ and $\zeta_c \in [-1;\ 1]$. Representative values of $(T_b, T_c)_i$ are given by LeBlanc *et al.* (2008) and the effective number of cycles N_i follows from the rainflow-counting method. The value for θ_0 can be replaced by θ_s, and since θ_0 is typically less than θ_s, this results conservatively in a slightly higher estimate of the accumulated pile rotation. It is relatively straightforward to determine the values for θ_s from the static load deflection curve. Finally, the accumulated pile rotation is calculated by

$$\begin{aligned} &\Delta\theta_0 = 0 \\ &\textit{iterations } i = 1,2,\dots,i_{max} \\ &\quad \Delta\theta_i = \left((\Delta\theta_{i-1})^{\frac{1}{\alpha}} + \mathrm{N}_i \times (\theta_\mathrm{s}\mathrm{T}_\mathrm{b}\mathrm{T}_\mathrm{c})_i^{\frac{1}{\alpha}} \right)^{\alpha} \\ &\quad \theta_i = \Delta\theta_\mathrm{i} + \ max\left[\theta_{\mathrm{s},1}, \dots, \theta_{\mathrm{s},i}\right] \end{aligned} \tag{7}$$

Example

The methodology can be used to assess the effect of different loads on the accumulated rotation of an offshore wind turbine. Typically, the load conditions are divided into the ultimate, serviceability and fatigue limit states (ULS, SLS and FLS) which occur 1, 10^2 and 10^7 times during the turbine's lifetime. Realistic design loads for a 2MW turbine are $M_{ULS} = 0.74 \times M_R$, $M_{SLS} = 0.47 \times M_R$ and $M_{FLS} = 0.29 \times M_R$ where M_R is the ultimate capacity. Table 3 is based on these load characteristics for the model scale pile. It assumes that load characteristics are governed by $\zeta_c = 0$, though realistic load conditions are of a random character. The maximum accumulated rotation, determined using Table 3, is $\theta_p = 8.77 \times 10^{-3}$ radian. The contributions by SLS and FLS alone, cause accumulated deflections of 22% and 45% of θ_p, respectively. By comparison the worst expected load causes an accumulated deflection of 61% of θ_p. It is likely that the larger load cycles (M_{ULS} and M_{SLS}) act in one direction during storm events whilst FLS load cycles will be omni-

directional due to changing wind directions. Assuming that $2/3$ of the FLS cycles act in one direction and $1/3$ in the reversed direction then the estimated total rotation θ_p is reduced by 11% and the ULS load contributes 68% of the total accumulated rotation. Thus the largest load cycles, though very few, have a much higher impact on the accumulated rotation than the 10^7 cycles at the FLS.

4. Conclusion

This note sets out a method for predicting accumulated pile rotation under random two-way loading. The proposed model adopts a relationship similar to Miner's rule for superposing strain increments and is consistent with the method of LeBlanc *et al*. (2008) for piles under continuous long-term cyclic loading. Rainflow-counting is used to decompose time-series of varying loads into a set of simple load reversals. The validity of the model is supported by series of 1-g laboratory tests using drained sand. The model relies on the dimensionless parameter α and the functions T_b and T_c which are empirically determined. Further work should be carried out to investigate these parameters and functions, ideally from tests performed using large-scale piles installed in saturated sand. The effects of omni-directional loading should also be addressed.

REFERENCES

Cox, W. R., Reese, L., and Grubbs, B. R. Field testing of laterally loaded piles in sand, *Proc. of the Offshore Tech. Conf.*, Houston, 1974, Paper no. 2079.

DNV. Offshore standard, DNV-OS-J101: Design of offshore wind turbine structures, Det Norske Veritas, Hellerup, Denmark, 2004.

LeBlanc, C., Houlsby, G. T. and Byrne, B. W. Response of stiff piles to long-term cyclic lateral loading, *Geotechniqué*, 2008. Accepted.

Lesny, K. and Hinz, P. Investigation of Monopile Behaviour under cyclic lateral loading, *Proc., Offshore Site Investigation and Geotechnics*, Soc. for Underwater Technology, London, 2007, 383–390.

Long, J. and Vanneste, G. Effects of cyclic lateral loads on piles in sand, *Journal of geotechnical engineering*, 1994, **120**, No. 1, 225–244.

Lin, S. S. and Liao, J. C. Permanent strains of piles in sand due to cyclic lateral loads, *Journal of Geotechnical and Geoenvironmental Engineering*, 1999, **125**, No. 9, 798–802.

Little, R. L. and Briaud, J.-L. Full scale cyclic lateral load tests on six single piles in sand, *Miscellaneous Paper GL-88-27*, Geotechnical Div., Texas A&M Univ., College Station, Texas, 1988.

Miner, M. A. Cumulative damage in fatigue, *Jour. of applied mechanics*, 1948, **12**, No. 3, A159-164.

McClelland, B. and Focht, J. A. J. Soil modulus for laterally loaded piles, *Transactions*, 1958, **123**, 1049–1086.

O'Niell, M. W. and Murchison, J. M. An evaluation of p-y relationships in sands, *Research Rep. No. CE-STR-90-27*, Dept. of Civ. Engrg., Univ. of Houston, Houston, 1983.

Reese, L. and Matlock, H. Nondimensional solutions for laterally loaded piles with soil modulus assumed proportional to depth, *Proc., VIII Conf. on Soil Mech. and Found. Eng.*, University of Texas, Austin, 1956, pp. 41.

Reese, L., Cox, W. R., and Koop, F. D. Analysis of Laterally Loaded Piles in Sand, Proc., *Sixth annual offshore tech. conf.*, Houston, 1974, vol. 2.

Rychlik, I. A new definition of the rainflow cycle counting method, *Int. Jour. of Fatigue*, 1987, **9**, No. 2, 119–121.

Schnaid, F. A study of the cone-pressuremeter test in sand, Ph.d thesis, University of Oxford, 1990.

Steward, H.E. Permanent strains from cyclic variable-amplitude loadings. *Jour. of Geotechnical Engineering*, 1986, **112**, No. 6, 646-660.

NOTATION

α	=	dimensionless parameter (-);
D	=	pile diameter (m);
e	=	load eccentricity (m);
H	=	horizontal load (N);
L	=	penetration depth of pile (m);
M	=	moment at seabed (Nm);
M_{min}	=	minimum moment in load reversal (Nm);
M_{max}	=	maximum moment in load reversal (Nm);
M_R	=	static moment resistance of pile (Nm);
N	=	number of load cycles (-);
N_a	=	number of load cycles of type a (-);
N_a^0	=	equivalent number of load cycles of type a (-);
R_d	=	relative density (%);
t	=	wall thickness (mm);
T_b, T_c	=	dimensionless functions;
y	=	horizontal deflection (m);
z	=	depth below seabed (m);
ζ_b, ζ_c	=	load characteristic parameters (-);
θ	=	pile rotation (rad);
θ_0	=	maximum pile rotation in first cycle (rad);
θ_d	=	accumulated pile rotation (rad);
θ_s	=	static pile rotation (rad);
θ_p	=	predicted maximum pile rotation (rad);

Pile diameter, D: mm	80.0
Wall thickness, t: mm	2.1
Penetration depth, L: mm	360.0
Load eccentricity, e: mm	430.0

Table 1. Properties of the copper monopile

Load regime	ζ_b	ζ_c	$T_b(\zeta_b, R_d)$	$T_c(\zeta_c)$	θ_s [rad]	$\theta_0[rad]$
A	0.28	0	0.055	1	0.45×10^{-3}	0.35×10^{-3}
B	0.41	0	0.091	1	0.90×10^{-3}	0.63×10^{-3}
C	0.53	0	0.135	1	1.60×10^{-3}	0.93×10^{-3}

Table 2. Characteristics of the load types A, B and C

Characteristics of the cyclic loading

Load Type	N	θ_s *(rad)*	T_b	T_c
FLS	1.00×10^7	4.80×10^{-4}	0.057	1
SLS	100	1.39×10^{-3}	0.0955	1
ULS	0*	5.32×10^{-3}	0.17	1

Calculation of cumulative rotation using algorithm in Table 4

Load Type	i	$\Delta\theta_i$	$max[\theta_{s,1}, \dots, \theta_{s,i}]$	θ_i
-	0	0	0	0
FLS	1	3.44×10^{-3}	4.80×10^{-4}	3.92×10^{-3}
SLS	2	3.45×10^{-3}	1.39×10^{-3}	4.84×10^{-3}
ULS	3	3.45×10^{-3}	5.32×10^{-3}	$\theta_p =$ 8.77×10^{-3}

Calculation of accumulated rotation for continuous cyclic loading (virgin loading) using equation (1) and (2)

Load Type	$\Delta\theta = (\theta_s T_b T_c)_a \times N^\alpha$	$\theta = \theta_s + \Delta\theta$	Ratio of θ to θ_p
FLS	3.44×10^{-3}	3.92×10^{-3}	44.8 %
SLS	5.28×10^{-4}	1.92×10^{-3}	21.9 %
ULS	0	5.32×10^{-3}	60.7 %

* A ULS peak load occurs only once. Thus, $N = 0$ since a full reloading cycle at the ULS load will not occur (Fig. 3).

Table 3. Example: Prediction of the cumulative rotation for an offshore wind turbine

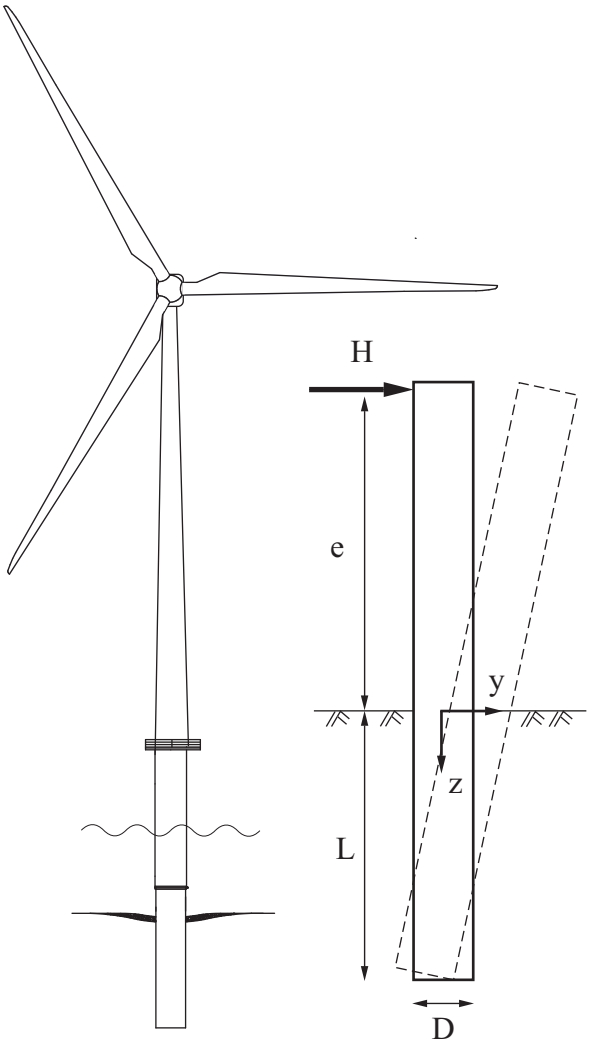

Fig. 1. A typical offshore wind turbine installed on a monopile foundation

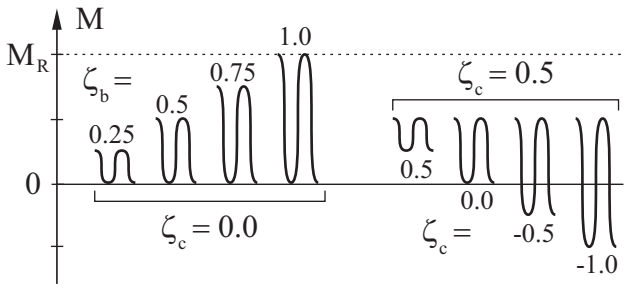

Fig. 2. The characteristics of cyclic loading defined in terms of ζ_b and ζ_c

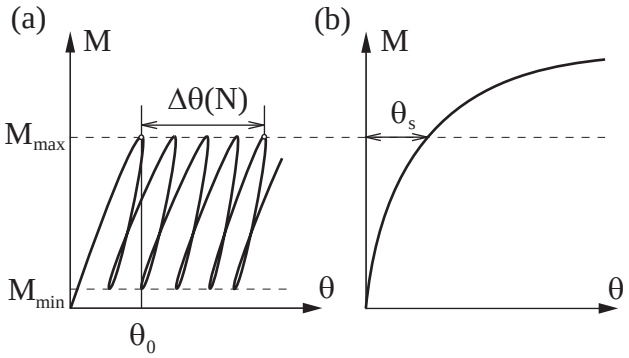

Fig. 3. Method for determination of accumulated rotation. (a) Cyclic test (b) Static test

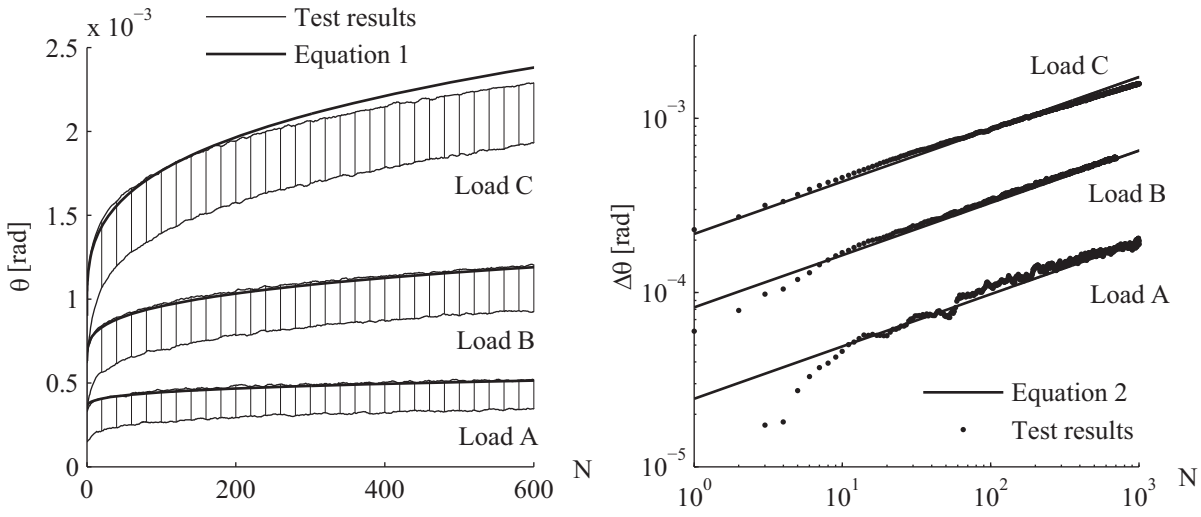

Fig. 4. Measured and predicted pile rotation in response to continuous sinusoidal loading of type A, B and C

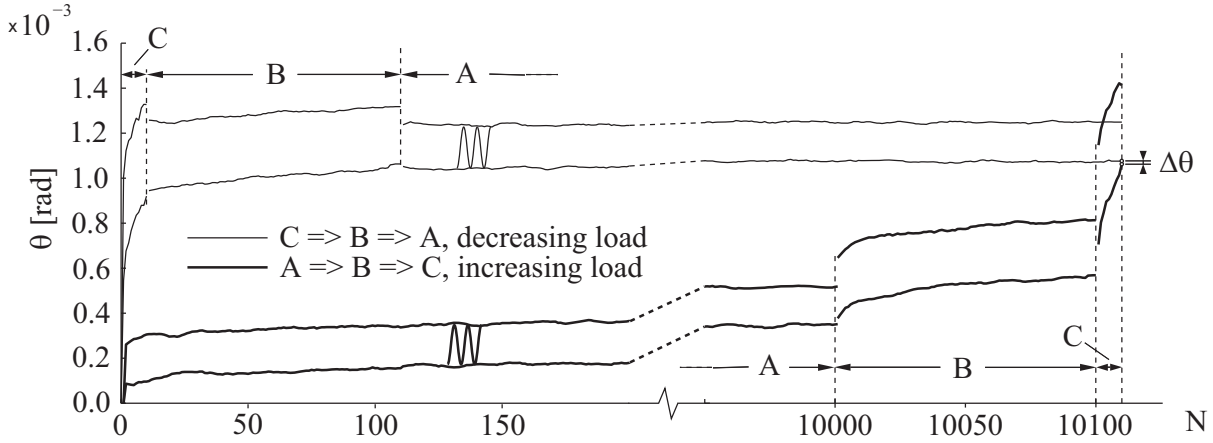

Figure 5. Envelopes of pile rotation measured for an increasing load sequence $10^4 \times A \rightarrow 100 \times B \rightarrow 10 \times C$ and an equivalent decreasing load sequence $10 \times C \rightarrow 100 \times B \rightarrow 10^4 \times A$

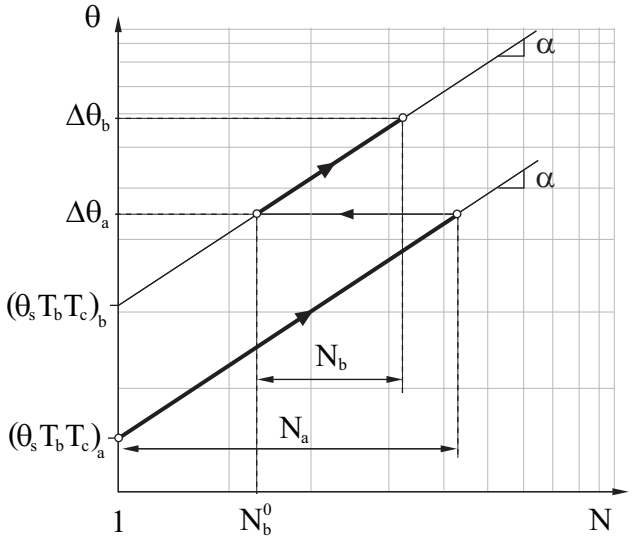

Fig. 6. Superposition theory for prediction of cumulative pile rotation in response to variable cyclic loading

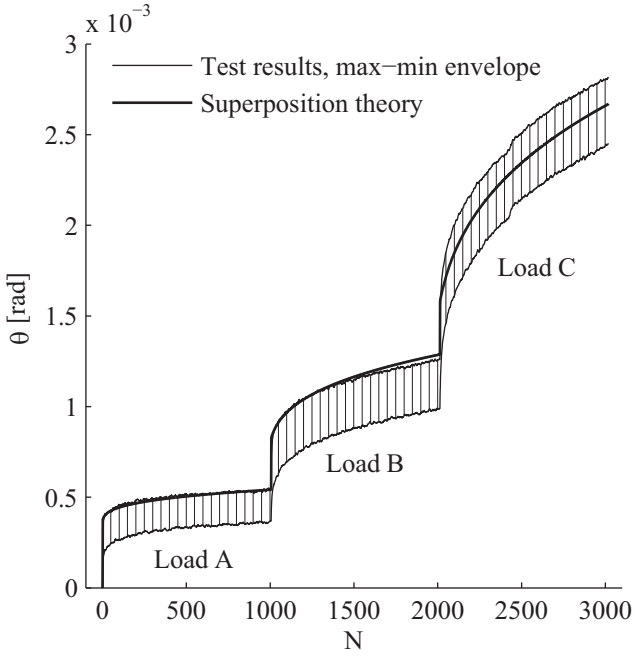

Fig. 7. Comparison of measurements and prediction of the accumulated pile rotation in response to variable cyclic loading: $1000 \times A \rightarrow 1000 \times B \rightarrow 1000 \times C$

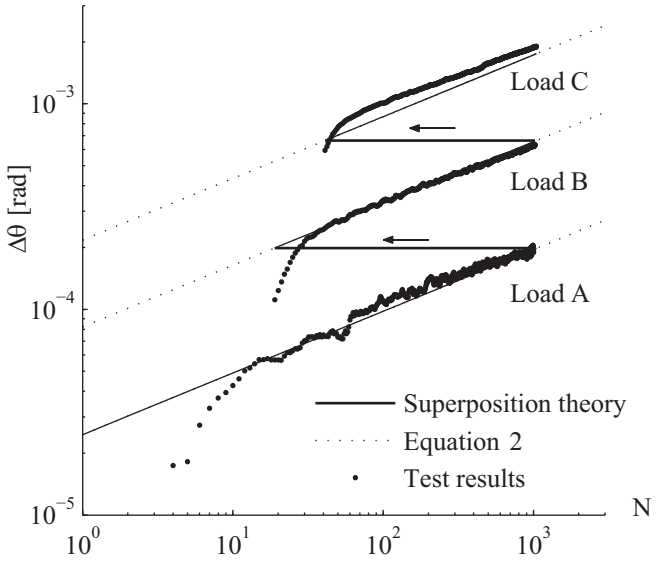

Fig. 8. Comparison of measurements and prediction of $\Delta\theta$ in response to variable cyclic loading: $\mathbf{1000 \times A \rightarrow 1000 \times B \rightarrow 1000 \times C}$

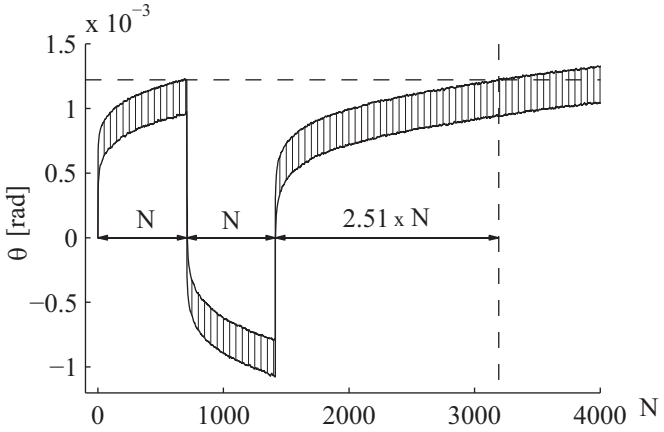

Fig. 9. Pile deflection in response a change in direction of loading type B, corresponding to $\zeta_b = 0.41 \rightarrow \zeta_b = -0.41 \rightarrow \zeta_b = 0.41$

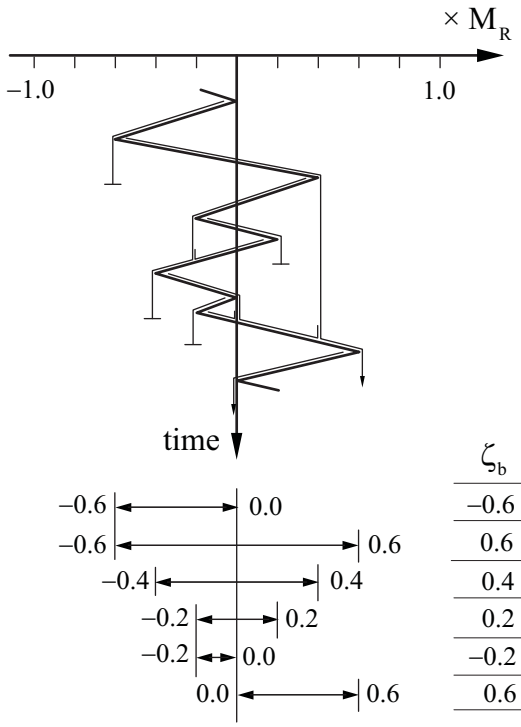

ζ_b	ζ_c
−0.6	0.0
0.6	−1.0
0.4	−1.0
0.2	−1.0
−0.2	0.0
0.6	0.0

Fig. 10. Example of an extended rainflow counting method based on a procedure by Rychlik (1987)

PAPER III

LeBlanc, C., Hededal, O. & Ibsen, L. B.

A modified critical state plasticity model for sand - theory and implementation

Dept. of Civil Engineering, Aalborg University, Aalborg, DCE Technical Memorandum No. 8, 2008.

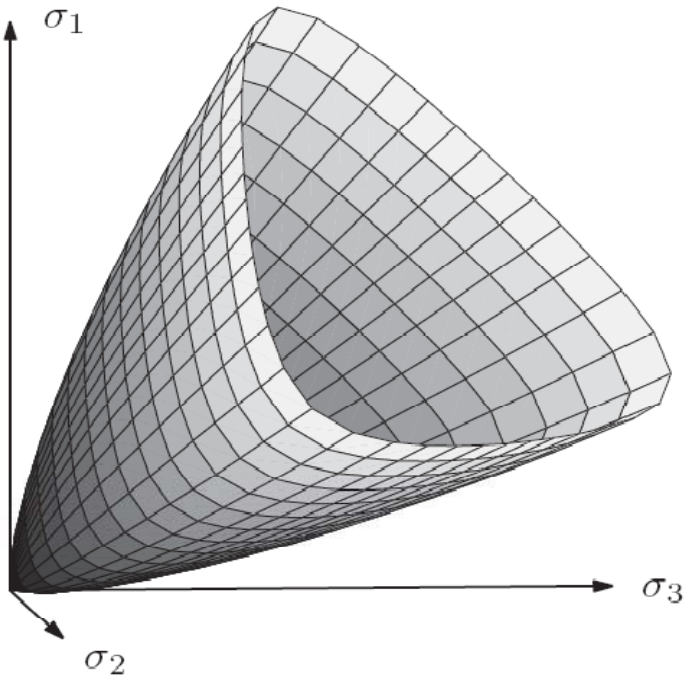

Bounding surface of the modified critical state two-surface plasticity model for sand

A modified critical state two-surface plasticity model for sand - theory and implementation

C. LeBlanc[1,2,*] O. Hededal[3] and L. B. Ibsen[1]

[1] *Department of Civil Engineering, Aalborg University, 9000 Aalborg, Denmark*
[2] *Department of Offshore Technology, DONG Energy, 2450 Copenhagen SV, Denmark*
[3] *Department of Civil Engineering, Technical University of Denmark, 2800 Kgs. Lyngby, Danmark*

SUMMARY

This paper provides background information and documentation for the implementation of a robust plasticity model as a user-subroutine in the commercial finite difference code, FLAC3D by Itasca. The plasticity model presented is equal to the 3 dimensional critical state two-surface plasticity model for sands by Manzari *et al.*, but uses a modified multi-axial surface formulation based on a versatile shape function prescribing a family of smooth and convex contours in the π-plane. The model is formulated within the framework of critical state soil mechanics and is capable of accurately simulating volumetric and stress-strain behaviour under monotonic and cyclic loading and thereby related observations like accumulation of pore pressure, cyclic mobility and cyclic liquefaction. The plasticity model is implemented with an integration scheme based on the general return mapping algorithm. The integration scheme faces convergence difficulties, primarily at very low mean effective stresses. The convergence problems are addressed by suitable correction strategies designed to add robustness, stability and efficiency to the integration scheme. An outline of all model parameters is given with suggestions for parameter reductions.

KEY WORDS: constitutive modeling; granular materials; critical state; bounding surface; return mapping method; implementation strategy

1. INTRODUCTION

Over the last decades, plasticity models that accurately simulate stress-strain behaviour of materials have been successfully used within several engineering disciplines. However, for granular materials, only simple classical elasto-plastic models are supported by most commercial engineering codes, e.g. Mohr-Coulomb and Cam-Clay. While these models are useful for many geotechnical problems, they are insufficient for more complex problems. More advanced models may be required to accurately simulate the response of soil under a wide range of relative densities and mean effective stress levels. Also, advanced models are required to simulate the response to cyclic loading and related observations such as accumulation of

*Correspondence to: C. LeBlanc, Dept. of Offshore Technology, DONG Energy, A.C.Meyers Vænge 9, 2450 Copenhagen SV, Denmark, E-mail: chrle@dongenergy.com

pore pressure, cyclic mobility and cyclic liquefaction. Continuum-based constitutive models simulating the cyclic behaviour of soil are primarily developed and applied within the framework of earthquake engineering in which the degradation of strength and stiffness is essential for the prediction of seismic performance of structures. The models are complex as several geotechnical features, e.g. characteristic states, critical states and failure envelopes, must be successfully simulated while accounting for a strong influence of the third stress invariant and the isotropic stress level.

The critical state soil mechanics (CSSM) [27, 28] provide a broad framework to explain the fundamental behaviour of granular materials. The success and broad recognition of the CSSM has lead to widespread application in constitutive models. The *Norsand model* [19] initially adopted the CSSM in a model formulation. Later notable critical state models include [3, 7, 13, 25, 31] and more complex models, also accounting for anisotropic stress-strain behaviour, are presented by [6, 10]. A versatile and yet simple model, formulated by within the framework of CSSM, is the *critical state two-surface plasticity model for sands* presented by Manzari et al. [23, 24]. The model has proved to successfully simulate drained and undrained stress-strain behaviour of non-cohesive sands under monotonic and cyclic loading in a wide range of confining stresses and densities [24, 30]

This paper provides background information and documentation for the implementation of a robust plasticity model as a user-subroutine in the commercial finite difference code FLAC3D (Fast Lagrangian Analysis of Continua in Three Dimensiobs) by Itasca. The constitutive model presented is equal to the two-surface critical state plasticity model for sands by Manzari et al. [23, 24], except for minor modifications. Thus, the model is denoted the *modified two-surface critical state plasticity model for sands*. The major modification is the introduction of an alternative multi-axial surface formulation based on a versatile shape function used to prescribe a family of smooth and convex contours in the π-plane. Emphasis is made to outline the physical interpretation of the plasticity model. An outline of all model parameters is given with suggestions for parameter reductions.

An efficient integration scheme based on a general return mapping algorithm originally proposed by Simo and Ortiz [29] is tailored to the plasticity model. The integration scheme is efficient, however only conditionally stable. Thus, an implementation strategy is introduced to add robustness to the integration scheme. The stability and efficiency is tested by simulations of undrained monotonic and cyclic triaxial tests. Thus, this paper provide complete information for implementation of a robust user-defined constitutive model, capable of simulating the response of non-cohesive sands, in a commercial finite difference (or finite element) code.

2. ON THE FRAMEWORK OF CRITICAL STATE SOIL MECHANICS

The concept *critical state* is successfully applied within the CSSM [27, 28]. Consider a soil sample subjected to shear loading. As shearing continues beyond peak shear stress, a state is reached after which further shearing causes zero volumetric change and zero change in shear stress, see Figure 1. This state, describing the post-peak behaviour, is referred to as the *critical state*, according to Casagrande [2]. An important outcome of the CSSM is that the critical

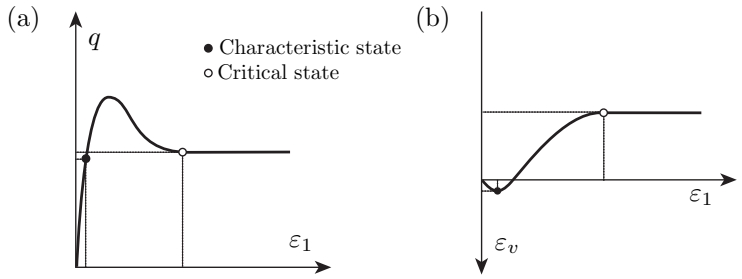

Figure 1. Outline of a typical triaxial compression test on dense sand performed under constant isotropic stress with q and ε_v converging against a constant value at critical state.

state can be represented by a straight line in p-q stress space[†], with the inclination being largely independent of both the relative density and isotropic stress level. The inclination can be defined by the *critical stress ratio*, $M_{\mathrm{cr}} = q/p$. M_{cr} seems to represent an intrinsic parameter and is therefore adopted as a fundamental model parameter.

At critical state, the soil particles can rearrange while the packing density remains constant. The *critical void ratio*, e_{cr}, is used to quantify the packing density at critical state. Experiments indicate that e_{cr} is independent of the initial void ratio, i.e. the soil particles always self-organize toward a critical packing density when sheared beyond critical state [2]. Figure 2a schematically illustrates the void ratio converging toward e_{cr} under monotonic shearing. The

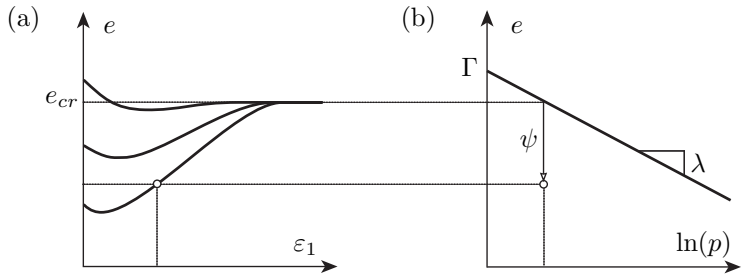

Figure 2. (a) Outline of change in void ratio obtained from triaxial compression tests of sand under a constant isotropic stress. (b) Variation of critical void ratio with isotropic stress level.

value of e_{cr} depends on the isotropic stress level as outlined in Figure 2b. Within the CSSM, the variation of e_{cr} and p is assumed linear in e_{cr}-ln(p) space. The line is referred to as the *critical state line*, defined by

$$e_{cr} = \Gamma - \lambda \ln\left(\frac{p}{p_{\mathrm{u}}}\right) \qquad p_{\mathrm{u}} = 1kPa \tag{1}$$

The constants λ and Γ denote the line inclination and the reference void ratio at the unit pressure p_{u}, respectively. It is convenient to have a parameter indicating the distance to critical

[†]In this paper, all stress notations refer to effective stresses.

state. In this context, the *state parameter* is defined by

$$\psi = e - e_{cr} \tag{2}$$

with e referring to the void ratio in the current state [1]. The state parameter is an essential parameter arising from the framework of the critical state soil mechanics and has been successfully adopted for constitutive modelling. The state parameter is adopted in the current model to prescribe peak stress levels and dilatancy behaviour.

3. MODELLING THE PEAK SHEAR STRENGTH OF SANDS

It is well documented that a strong correlation exists between the relative density and the peak shear strength of sands. The typical variation of peak shear strength with isotropic pressure and relative density is outlined in Figure 3a and 3b.

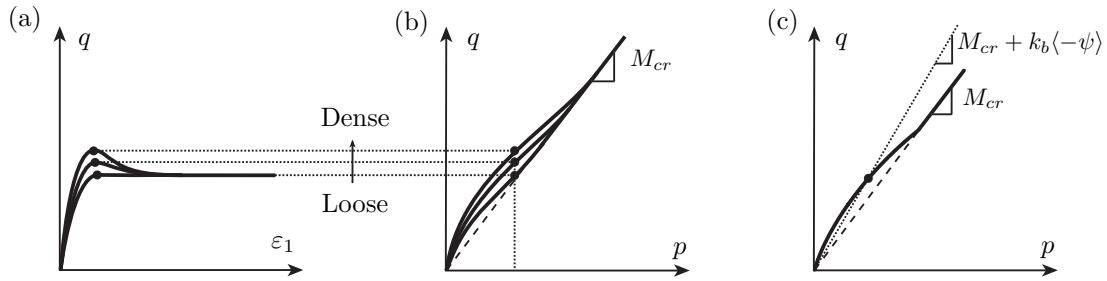

Figure 3. Typical variation of drained shear strength with isotropic pressure and relative density obtained from triaxial compression tests. (a) (ε_1, q)-diagram (b) (p, q)-diagram (Cambridge diagram) (c) Model formulation of bounding line.

The peak shear strength can be divided into two components. A base component is related to the critical state shear stress, with sand particles being able to rearrange under constant volume. This component can be represented by the critical stress ratio, M_{cr}. The second component arises from the dilation of the sand due to shearing. A densely packed sand will exhibit strong dilation and thus obtain a large shear strength due to the increased amount of energy needed for grain particles to slide around adjacent particles. The resulting peak shear strength can be defined by a threshold in stress space referred to as *failure envelope* or *bounding line*.

Since the location of the bounding line is highly correlated to the dilatancy, and thereby the packing density of the sand, it is meaningful to adopt the state parameter ψ in a bounding line formulation for constitutive modelling. The bounding line adopted by the current model is based on a formulation whereby the *bounding stress ratio*, $M_b = q/p$, is equal to M_{cr} plus a contribution proportional to ψ [32, 23]

$$M_b(\psi) \quad = \quad M_{cr} + k_b\langle -\psi \rangle \tag{3}$$

in which k_b is a dimensionless model parameter and $\langle\ \rangle$ refer to Macauley brackets, defined by $\langle x \rangle = 0$ if $x < 0$ else $\langle x \rangle = x$. This formulation ensures an increased peak shear strength for densely packed sands with curvature of the bounding line arising from the p-dependency of ψ.

Furthermore, the formulation ensures that the bounding line coincides with the critical state line for either very loose sands or at high isotropic pressures. The bounding line formulation is illustrated in Figure 3c.

It can be noted, that if the slope of the critical state line is very small (i.e. $\lambda \approx 0$), then the p-dependency of ψ in (1) become negligible. In this case, the location of the bounding and characteristic surfaces is then only influenced by the current void ratio, or as commonly adopted for sands, the relative density.

4. TRANSITION FROM COMPACTIVE TO DILATIVE BEHAVIOUR

Shearing of a granular material causes volumetric changes that are either compactive or dilative. Typical effective stress paths obtained from three triaxial compression tests on dense sand, performed with p = constant, are outlined in figure 4a. The corresponding volumetric changes are outlined in Figure 4b. The points, marked with dots, indicate the transition from compressive to dilative behaviour determined by $\delta\varepsilon_v/\delta\varepsilon_1 = 0$. These points indicate that there is a threshold in stress space, dividing the volumetric behaviour from compressive to dilative. This threshold is referred to as the *characteristic state* [22]. A consistent definition of the characteristic state is based on zero change in plastic volumetric strain, $d\varepsilon_v^p = 0$ [26].

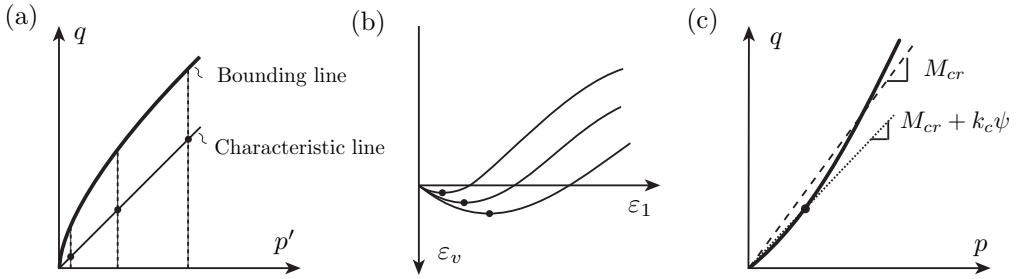

Figure 4. Outline of typical triaxial compression tests on dense sand performed with p' = constant. [16]

From monotonic triaxial tests, it has been determined that characteristic states can be represented by a straight line through origin in stress space [12, 15]. This line is referred as the *characteristic line*. Experiments indicate that the inclination of the characteristic line is constant and independent of both relative density and the isotropic stress level [12, 26]. Thus, it is tempting to define the characteristic line as a straight line with constant inclination, in terms of the *characteristic stress ratio*, $M_c = q/p$. However, while this is valid for monotonic loading, it may not be valid for cyclic loading. Also, one must have that $M_c \to M_{cr}$ as $\psi \to 0$, since the criterion defining the characteristic line, $d\varepsilon_v^p = 0$, must be fulfilled at the critical state. Thus, in the current model, the characteristic line is defined by

$$M_c(\psi) \quad = \quad M_{cr} + k_c\psi \tag{4}$$

in which k_c represents a dimensionless model parameter [23]. The characteristic line is illustrated in Figure 4c. The underlying physical background is rather weak, however, the simple formulation has been successfully adopted to simulate sand subjected to cyclic loading [23, 24].

5. MULTI-AXIAL FORMULATION

Granular materials exhibit a strong influence of the third stress invariant. This influence appear when comparing triaxial compression and extension tests, ie. lower shear friction can be sustained in triaxial extension. Thus, accurate simulation of granular materials require that the bounding and characteristic lines, defined in (3) and (4) respectively, are generalized to *bounding* and *characteristic surfaces* defined stress space using a multi-axial formulation. The multi-axial formulation introduced in this paper differs from the formulation used in the original model by Manzari *et al.* [23].

The influence of third stress invariant is conveniently depicted in the π-plane in which p remains constant. The minimum requirement for defining a contour in the π-plane is the specification of a 'corner' and a 'midpoint' of the triangular shape, corresponding to eg. triaxial compression and extension, respectively. Thus, for triaxial extension we may define the stress ratios of the bounding and characteristic lines similar to triaxial compression in (3) and (4) by

$$M_b^{ex} = M_{cr}^{ex} + k_b^{ex}\langle -\psi \rangle \qquad M_c^{ex} = M_{cr}^{ex} + k_c^{ex}\psi \tag{5}$$

in which M_{cr}^{ex}, k_b^{ex} and k_c^{ex} are model parameters for triaxial extension equivalent to the parameters M_{cr}, k_b and k_c for triaxial compression.

Several mathematical formulations are proposed to define the triangular contour of the bounding surface, e.g. Lade [11], Matsuoka-Nakai [14] and Mohr-Coulomb. A versatile shape formulation, derived from a cubic polynomial of principal stresses, is proposed by Krenk [20, 21]. The formulation prescribes a family of smooth and convex contours given in terms of

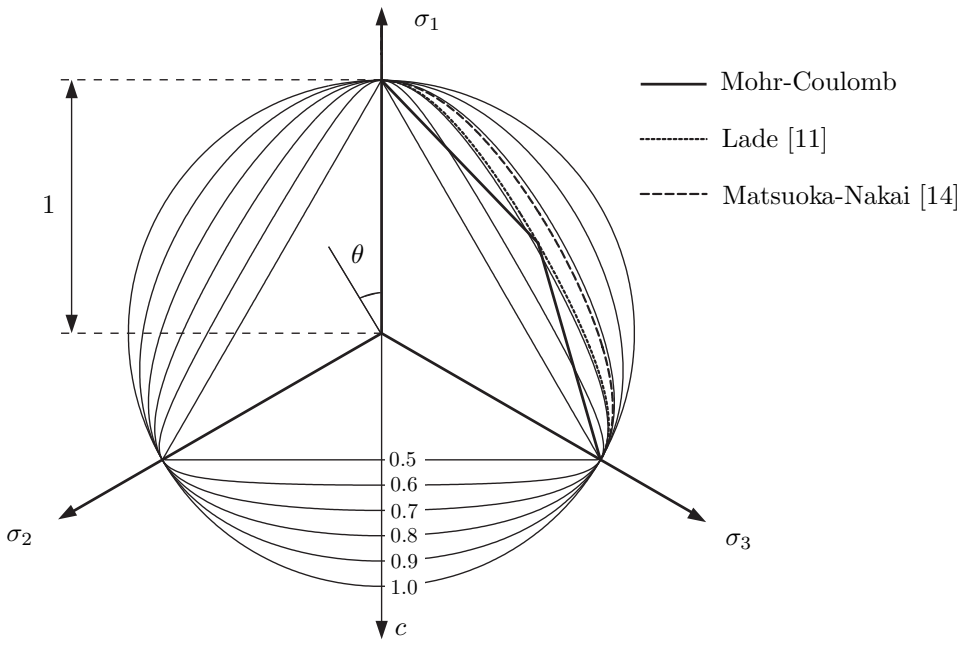

Figure 5. The family of surface contours prescribed by the function $g(c, \theta)$.

the second and third deviatoric stress invariants. The contours of this family can represent any shape from circular to triangular depending on a shape parameter. The original formulation by Krenk [20, 21] can be reformulated in terms of the Lode angle θ and the normalized shape function $g(c, \theta)$, defined such that $g(c, 0) = 1$ in triaxial compression and $g(c, \pi) = c$ in triaxial extension and thereby that $M_c^{ex} = cM_c$. In this case, g is expressed by

$$g(c,\theta) = \frac{\cos(\gamma)}{\cos\left(\frac{1}{3}\arccos(\cos(3\gamma)\cos(3\theta))\right)} \quad , \quad \gamma = \frac{\pi}{3} + \arctan\left(\frac{1-2c}{\sqrt{3}}\right) \tag{6}$$

The shape of the contours is uniquely defined by c. For example, a triangle is obtained for $c = 0.5$ whereas a circle is obtained for $c = 1$. The family of curves for $c \in [0.5; 1.0]$ is illustrated in Figure 5.

The shape of the bounding and characteristic surfaces are defined in terms of $g(c, \theta)$ in (6) using the shape parameters, $c = c_b$ and $c = c_c$, respectively. The values of c_b and c_c may be evaluated from the stress ratios defined in (3), (4) and (5).

$$c_b(\psi) = \frac{M_b^{ex}}{M_b} \qquad c_c(\psi) = \frac{M_c^{ex}}{M_c} \tag{7}$$

Both c_b and c_c are functions of ψ. For cohesionless granular materials, it is generally accepted that the bounding surface contour is triangular with $M_b \geq M_b^{ex}$; c_b will therefore lie in the range between 0.5 and 1. Representative values of c_c are limited accounted for in the literature.

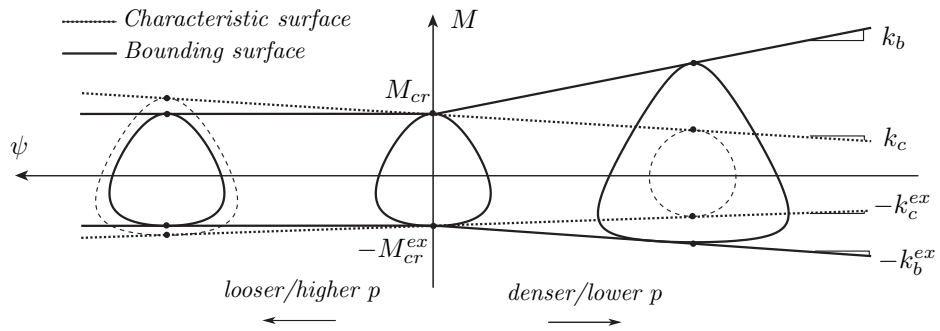

Figure 6. Visualization of the bounding and characteristic surface contours, as function of the state parameter ψ.

Figure 6 illustrates the shape of the bounding and characteristic surfaces as function of ψ as expressed in (7). For samples denser than critical ($\psi < 0$), the bounding surface obtains a triangular shape enclosing the characteristic surface; dilation will therefore occur before the bounding surface is reached. The bounding and characteristic surfaces become identical and equal to the *critical state surface* at the critical state ($\psi = 0$) where $c_b = c_c = M_{cr}^{ex}/M_{cr}$. For samples looser than critical ($\psi > 0$), the characteristic surface expands beyond the bounding surface to cause an entirely compactive behaviour, since the stress state always stays within the bounding surface.

Figure 7 illustrates the bounding surface in the principal stress space obtained using the expressions (3) and (5) in conjunction with (6) and (7).

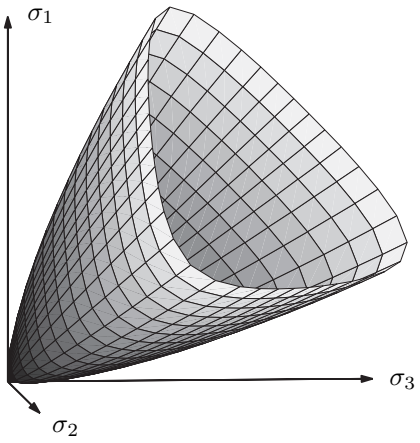

Figure 7. Visualization of the bounding surface in principal stress space.

A total of 6 model parameters define the surface contours and these may be determined from triaxial tests in both extension and compression. However, it may be appropriate to to adopt some simplifying assumptions in order to eliminate the model parameters M_{cr}^{ex}, k_b^{ex} and k_c^{ex} defining the behaviour in triaxial extension. Experimental evidence suggest that the critical angle of friction ϕ_{cr} is approximately equal under triaxial compression and extension [8]. Similarly, the widely applied Mohr-Coulomb failure criteria assumes that shear strength is governed by a constant angle of friction ϕ. The value of M is related to ϕ by $M = 6\sin\phi/(3-\sin\phi)$ in triaxial compression and $M^{ex} = 6\sin\phi/(3+\sin\phi)$ in triaxial extension. Combining these equations yields that the value of M and M^{ex} are related by $M^{ex} = 3M/(3+M)$. Thus, if the assumption of a constant friction angle under triaxial compression and extension is adopted, then (7) can be substituted by

$$c_b(\psi) = \frac{3}{3+M_b} \qquad c_c(\psi) = \frac{3}{3+M_c} \tag{8}$$

to eliminate the model parameters M_{cr}^{ex}, k_b^{ex} and k_c^{ex}.

If the assumption of a constant friction angle under triaxial compression and extension is undesired, then an alternative approach eliminating the 2 model parameters, k_b^{ex} and k_c^{ex}, may be done by simply choosing

$$c_b = c_c = \frac{M_{cr}^{ex}}{M^{cr}} \tag{9}$$

6. ELASTO-PLASTIC FORMULATION

The mathematical formulation of the plasticity model is presented in this section. The derivation follows that of Manzari and Prachathananukit [24]. The plasticity model is derived within the framework of non-associated elasto-plasticity. In the following derivation, all stress

notations refer to effective stresses. Bold symbols symbolize symmetric second-order tensors and the operators $\boldsymbol{u} : \boldsymbol{v}$ and $|\boldsymbol{u}|$ refer to the tensor product and tensor norm, respectively.

6.1. Elastic behaviour

The constitutive relations are formulated in terms of isotropic and deviatoric stress defined by $p = (\sigma_{11} + \sigma_{22} + \sigma_{33})/3$ and $\mathbf{s} = \boldsymbol{\sigma} - p\mathbf{I}$, respectively. $\mathbf{I}$ denotes the second order identity tensor. The elastic behaviour is based on the traditional isotropic hypoelastic formulation in which the elastic incremental stress-strain behaviour is defined by

$$d\boldsymbol{\varepsilon}_d^e = \frac{1}{2G} d\mathbf{s} \qquad d\varepsilon_v^e = \frac{1}{K} dp \tag{10}$$

where $d\boldsymbol{\varepsilon}_d^e$ and $d\varepsilon_v^e$ refer to the deviatoric and volumetric elastic strain increments, respectively. In the hypoelastic formulation, the elastic moduli, K and G, are assumed functions of the isotropic pressure

$$K = K_0 \left(\frac{p}{p_{\text{ref}}} \right)^b \qquad G = G_0 \left(\frac{p}{p_{\text{ref}}} \right)^b \tag{11}$$

in which p_{ref} is used as the reference pressure for which $K = K_0$ and $G = G_0$. The pressure exponent b is a model parameter, expressing the variation of the elastic modules with the isotropic pressure. The value of b is reported to vary from 0.435, at very small strains, to 0.765, at very large strains [33]. A value of 0.5 captures most of the important features of increased shear stiffness with pressure [34].

6.2. Yield and plastic potential functions

The elastic domain is enclosed by a yield surface with a cone-type shape and the apex in origin as illustrated in Figure 8. The yield surface is uniquely defined by the equation

$$f = |\mathbf{r}| - \sqrt{\frac{2}{3}} mp = 0 \qquad \mathbf{r} = \mathbf{s} - p\boldsymbol{\alpha} \tag{12}$$

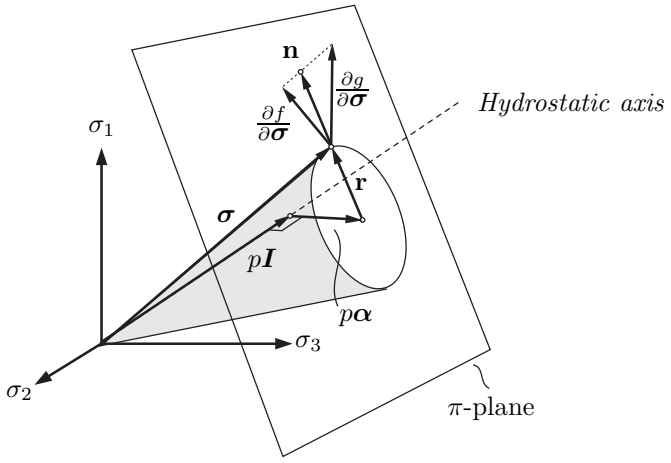

Figure 8. The cone-type yield surface defined in terms of m and $\boldsymbol{\alpha}$.

where $\boldsymbol{\alpha}$ is refered to as the deviatoric back-stress ratio tensor. This definition implies that the yield surface remains circular in the π-plane. The value $\sqrt{2/3}m$ and $\boldsymbol{\alpha}$ define the radius and the axis direction of the cone, respectively. The normals to the yield surface ($\partial f/\partial \boldsymbol{\sigma}$) and the plastic potential ($\partial g/\partial \boldsymbol{\sigma}$) define the loading and plastic flow direction, respectively. These are defined by:

$$\frac{\partial f}{\partial \boldsymbol{\sigma}} = \mathbf{n} - \frac{1}{3}N\mathbf{I} \qquad \frac{\partial g}{\partial \boldsymbol{\sigma}} = \mathbf{n} + \frac{1}{3}D\mathbf{I} \tag{13}$$

where $\mathbf{n} = \mathbf{r}/|\mathbf{r}|$ is the deviatoric normal to the yield surface. The parameters N and D define the magnitude of the isotropic components. From (12), it follows that $N = \boldsymbol{\alpha} : \mathbf{n} + \frac{2}{3}m$. The *dilatancy parameter* D has an important role as it controls the isotropic flow direction and thus the volumetric behaviour of the plasticity model. The plastic flow is non-associated, except in the special case where $D = -N$. It should be noted, that the formulation is not suitable for modeling constant stress-ratio response, i.e. consolidation paths where the stress ratio is constant as very high stress levels may be reached without inducing plastic strains, due to the lack of a surface cap.

6.3. Surface definitions using image points

The model is formulated by use of *image points*. The image point defines a point on a surface in the π-plane and is uniquely defined by the image vector $\boldsymbol{\alpha}_i$ pointing from the hydrostatic axis to the image point, in the direction of $\mathbf{n}$, see Figure 9. The bounding and characteristic surfaces, defined previously, can be formulated in terms of image vectors. In this case, the surfaces are expressed by

$$\boldsymbol{\alpha}_i = \sqrt{\frac{2}{3}}\left(g(c_i, \theta_{\mathbf{n}})M_i(\psi) - m\right)\mathbf{n} \quad , \quad i = b, c \tag{14}$$

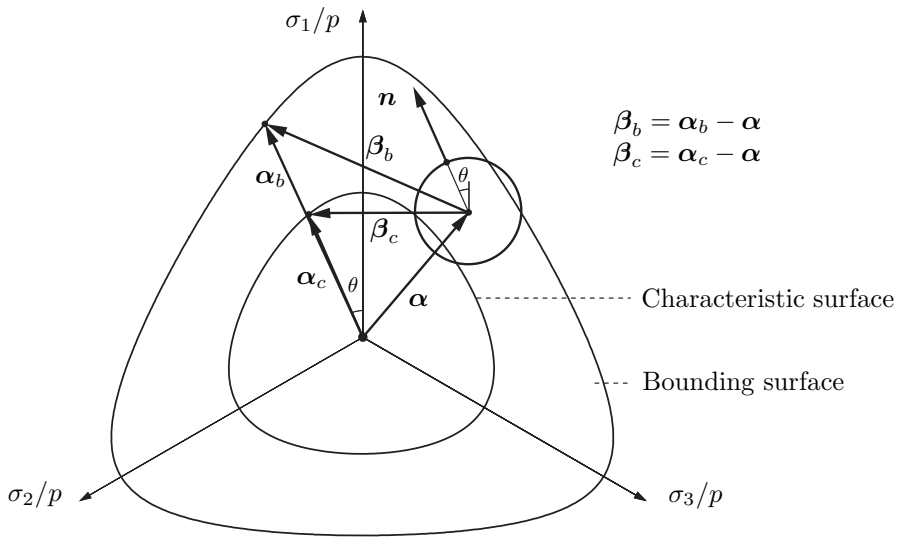

Figure 9. Illustration of the yield, characteristic and bounding surfaces in the π-plane.

where $\theta_{\mathbf{n}}$ refers to the Lode angle of $\mathbf{n}$. It is important to note that this surface formulation refers to back-stress ratios rather than stress ratios since the radius of the yield surface $\sqrt{2/3}m$ is subtracted. The Lode angle may be determined from the stress invariants J_2 and J_3 of $\mathbf{n}$

$$\cos(3\theta_n) = \frac{3\sqrt{3}}{2}\frac{J_3}{(J_2)^{3/2}} \tag{15}$$

The tensors, $\boldsymbol{\beta}_b = \boldsymbol{\alpha}_b - \boldsymbol{\alpha}$ and $\boldsymbol{\beta}_c = \boldsymbol{\alpha}_c - \boldsymbol{\alpha}$, define the distance between $\boldsymbol{\alpha}$ and their respective image points. These tensors are adopted in the formulation of model dilatancy and evolution laws for hardening parameters.

6.4. Volumetric behaviour

It is essential that the volumetric behaviour is simulated correctly. From (13), it follows that the plastic volumetric strains are proportional to D. The formulation of D is therefore of great importance. D is defined by

$$D = (A_0 + A_z)(\boldsymbol{\beta}_c : \mathbf{n}) \quad , \quad A_z = \langle \mathbf{z} : \mathbf{n} \rangle \tag{16}$$

where the *dilatancy parameter* A_0 represents a positive and dimensionless scaling parameter. This definition implies that the sign of $\boldsymbol{\beta}_c : \mathbf{n}$ defines the threshold between compressive and dilative behaviour. Thus, any stress state inside the characteristic surface obtains a compressive behaviour, since $\boldsymbol{\beta}_c : \mathbf{n} > 0$, whereas on-loading beyond the characteristic surface obtains a dilative behaviour, since $\boldsymbol{\beta}_c : \mathbf{n} < 0$.

The *unloading dilatancy parameter* A_z is defined in terms of the *fabric tensor* $\mathbf{z}$ which enables the model to capture the dilatancy of sand under reversed loading. The definition of A_z imply that $A_z = 0$, except during reversed loading where $A_z > 0$. The evolution of $\mathbf{z}$ is defined from an evolution law originally introduced by Dafalias [5]

$$d\mathbf{z} = \widetilde{\mathbf{z}} d\lambda \qquad \widetilde{\mathbf{z}} = -C_z(A_z^{max}\mathbf{n} + \mathbf{z})\langle -D \rangle \tag{17}$$

The factors C_z and A_z^{max} are positive dimensionless model parameters. The definition of $\mathbf{z}$ may be hard to interpret, however, the introduction of $\mathbf{z}$ enables the model to recall load history and evolve accordingly. The parameter A_z^{max} becomes an upper threshold value of A_z. The definition in (17) implies that $\mathbf{z}$ evolves in a direction opposite to $\mathbf{n}$ whenever the sample dilates ($D > 0$) such that the tensor product $\mathbf{z} : \mathbf{n}$ becomes positive, only when the load direction shifts to unloading.

6.5. Kinematic and isotropic hardening

Both kinematic and isotropic hardening are adopted in the model. The kinematic evolution law is based on a proposition by Dafalias and Popov [4]

$$d\boldsymbol{\alpha} = \widetilde{\boldsymbol{\alpha}} d\lambda \qquad \widetilde{\boldsymbol{\alpha}} = C_\alpha \left(\frac{|\boldsymbol{\beta}_{\mathbf{b}} : \mathbf{n}|}{b_r - |\boldsymbol{\beta}_b : \mathbf{n}|} \right) \boldsymbol{\beta}_b \tag{18}$$

C_α is a positive model parameter and b_r is a parameter that must be defined such that $b_r > |\boldsymbol{\beta}_b : \mathbf{n}|$. The adopted value is $b_r = 2\sqrt{2/3}(M_b - m)$. The evolution law ensures that $\boldsymbol{\alpha}$, the center of the yield cone, evolves in the direction of $\boldsymbol{\beta}_b$. The rate of evolution will converge to zero as $\boldsymbol{\alpha}$ approaches the bounding surface, due to inclusion of the factor $|\boldsymbol{\beta}_{\mathbf{b}} : \mathbf{n}|$. This implies

that the stress state remains inside the bounding surface during hardening. The bounding surface will contract during softening as the sand dilates and $\psi \to 0$. This contraction can leave the stress state outside the bounding surface. In this case, the direction of $\boldsymbol{\beta}_b$ is opposite to the loading direction $\mathbf{n}$, causing $|\boldsymbol{\beta}_b : \mathbf{n}|$ to become negative. Thus, $\boldsymbol{\alpha}$ will evolve in the opposite direction of $\boldsymbol{\beta}_b$ and thereby follow the contracting bounding surface. The isotropic hardening law is based on an original proposition by Manzari et al. [23]

$$dm = \widetilde{m} d\lambda \qquad \widetilde{m} = C_m(1 + e_0)D \tag{19}$$

where C_m is a model parameter and e_0 is the initial void ratio. The formulation implies that the evolution of m becomes proportional to the plastic rate of change of volume. This ensures that a compacted sand obtains a larger elastic domain than a loose sand. Even though the model allows for isotropic hardening, this model practically retain a constant radius m of the elastic domain. Therefore, isotropic hardening is often neglected ($C_m = 0$) since it is of less importance for the shear behaviour of sands.

6.6. Model parameters

A complete list of model parameters is given in Table I. The table include suggestions for elimination of several model parameters to ease calibration if limited data is available. Specification of initial conditions is required - these include e_0, p_0, $\mathbf{S}_0$, $\mathbf{A}_0$ and m_0. The initial value of the back-stress may conveniently be chosen as $\mathbf{A}_0 = \mathbf{S}_0/p_0$. It may be appropriate to choose a small initial size of the yield cone, i.e. $m_0 \approx 0.05$, and neglect isotropic hardening

List of model parameters:			Reduction of parameters	
Parameter		Description	Optional	Monotonic
Elasticity	K_0	Reference bulk modulus. [Pa]	-	-
	G_0	Reference shear modulus. [Pa]	$0.5 \times K_0$	-
	b	Pressure exponent.	0.5	-
Critical state	λ	Slope of CSL in e-ln(p) space.	-	-
	Γ	Critical state void ratio for p'=1Pa.	-	-
	M_{cr}	Slope of CSL in p-q space in triaxial compression.	-	-
	M_{cr}^{ex}	Slope of CSL in p-q space in triaxial extension.	n.a.[1]	-
Surface definitions	k_b	Bounding line in triaxial compression.	-	-
	k_b^{ex}	Bounding line in triaxial extension.	n.a.[1]	-
	k_c	Characteristic line in triaxial compression.	-	≈ 0
	k_c^{ex}	Characteristic line in triaxial extension.	n.a.[1]	≈ 0
Hardening	C_m	Evolution of isotropic hardening.	0	n.a.
	C_α	Evolution of kinematic hardening.	-	-
Dilatancy	A_0	Dilatancy parameter	-	-
Unloading dilatancy	C_z	Evolution of fabric tensor.	0	n.a.
	z_{max}	Limit size of fabric tensor.	0	n.a.
[1]: Simplifying assumption: $M_i^{ex} = 3M_i/(3 + M_i) \quad i = b, c$				

Table I. List of model parameters and optional parameter reductions.

($C_m = 0$). In this case, the size of the elastic domain remains small and the response to shearing is mainly governed by the evolution law for kinematic hardening. Thus, G_0 is of less importance and may conveniently be chosen as $G_0 = 0.5 \times K_0$ which corresponds to an elastic Poisson's ratio equal to 0.29. A representative shear stiffness is then obtained by calibrating C_α.

7. INTEGRATION ALGORITHM

An efficient and accurate time-stepping integration scheme must be adopted to incrementalize and utilize the cyclic plasticity model. The fact that the elasto-plastic stiffness depends on both current stresses and hardening parameters challenges the integration of the constitutive relations. The most suitable integration algorithm may depend on the type of global solver. This paper provides a fast, stable and accurate integration algorithm suitable for an explicit global solver, such as FLAC3D. It is characteristic for an explicit global solver, that the step-size is very small. This calls for a fast return mapping or sub-stepping integration scheme on constitutive level. A benchmark analysis by Manzari [24] included a cutting plane algorithm belonging to the family of explicit return mapping methodss, originally derived by Simo & Ortiz [29]. The benchmark analysis showed that the highest efficiency was obtained using the cutting plane algorithm, however, the algorithm failed to converge at low stress levels. A return mapping method is adopted in this paper and convergence problems are addressed by adopting a suitable implementation strategy.

7.1. Return mapping method

The derivation of the return mapping method relies on basic elasto-plastic assumptions. Firstly, the integration of the constitutive relations must satisfy the consistency condition. The consistency condition, in terms of the hardening parameter H, is given by

$$\frac{\partial f}{\partial \boldsymbol{\sigma}} d\boldsymbol{\sigma} - H d\lambda = 0 \qquad\qquad H = -\left(\frac{\partial f}{\partial \boldsymbol{\alpha}} \tilde{\boldsymbol{\alpha}} + \frac{\partial f}{\partial m} \tilde{m} \right) \tag{20}$$

Secondly, the theory of elasto-plasticity assumes that a stress increment can be divided into an elastic and a plastic part

$$\Delta\boldsymbol{\sigma} = \mathbf{C} : (\Delta\boldsymbol{\varepsilon} - \Delta\boldsymbol{\varepsilon}^p) = \Delta\boldsymbol{\sigma}^e - \Delta\boldsymbol{\sigma}^p \tag{21}$$

The stress increments $\Delta\boldsymbol{\sigma}^e$ and $\Delta\boldsymbol{\sigma}^p$ are referred to as the elastic predictor and plastic corrector, respectively and $\mathbf{C}$ refers to the hypoelastic stiffness matrix. The purpose of the return mapping method, is to determine the plastic corrector such that the stress state remains on the yield surface while the consistency condition is fulfilled. Given the current stress state $\boldsymbol{\sigma}_0$ and a strain increment $\Delta\boldsymbol{\varepsilon}$, the stress state in the subsequent step can be calculated by

$$\boldsymbol{\sigma} = \boldsymbol{\sigma}_0 + \mathbf{C} : (\Delta\varepsilon - \Delta\boldsymbol{\varepsilon}^p) \tag{22}$$

according to (21). By initially setting $\Delta\boldsymbol{\varepsilon}^p = \mathbf{0}$ in (22), the elastic predictor stress $\boldsymbol{\sigma}^{elas}$ is calculated, leaving the plastic correction $\Delta\boldsymbol{\sigma}^p = \mathbf{C} : \Delta\boldsymbol{\varepsilon}^p$ to be determined. The plastic correction is governed by the flow rule

$$\Delta\boldsymbol{\varepsilon}^p = \Delta\lambda \frac{\partial g}{\partial \boldsymbol{\sigma}} \tag{23}$$

Thus, the purpose of the return mapping method is reduced to determining the magnitude of $\Delta\lambda$ while fulfilling (20). This is addressed by a first order Taylor expansion of the yield function around $\boldsymbol{\sigma}^{elas}$ while utilizing that $f(\boldsymbol{\sigma}) = 0$

$$f(\boldsymbol{\sigma}) = f(\boldsymbol{\sigma}^{elas}) - \frac{df}{d\boldsymbol{\sigma}} : \Delta\boldsymbol{\sigma}^p + \frac{df}{d\lambda}\Delta\lambda = 0 \tag{24}$$

From the consistency condition, it follows that $df/d\lambda = H$. Thus, by rearranging (24), and using the relation $\Delta\boldsymbol{\sigma}^p = \mathbf{C}\Delta\boldsymbol{\varepsilon}^p$ combined with (23), a linear expression determining the magnitude of the plastic multiplier can be obtained. This linear expression is however inadequate since the gradients $\partial f/\partial\boldsymbol{\sigma}$ and $\partial g/\partial\boldsymbol{\sigma}$ as well as the hardening parameter H vary along the return path from $\boldsymbol{\sigma}^{elas}$ to $\boldsymbol{\sigma}$. An iterative scheme must be adopted to solve this problem. Simo and Ortiz [29] proposed an explicit scheme, the general return mapping method, solving the problem in a sequence of linearized steps. The steps are given by

$$\boldsymbol{\sigma}_i = \boldsymbol{\sigma}_0 + \mathbf{C} : (\Delta\boldsymbol{\varepsilon} - \Delta\boldsymbol{\varepsilon}^p_{i-1}) \tag{25}$$

$$\Delta\lambda = \left(\frac{f(\boldsymbol{\sigma}_i)}{(\partial f/\partial\boldsymbol{\sigma}) : \mathbf{C} : (\partial g/\partial\boldsymbol{\sigma}) + H}\right)_{i-1} \tag{26}$$

$$\Delta\boldsymbol{\varepsilon}^p_i = \Delta\boldsymbol{\varepsilon}^p_{i-1} + \Delta\lambda\left(\frac{\partial g}{\partial\boldsymbol{\sigma}}\right)_{i-1} \tag{27}$$

$$\Delta\mathbf{x}_i = \Delta\mathbf{x}_{i-1} + \Delta\lambda\widetilde{\mathbf{x}}_{i-1} \tag{28}$$

where $\mathbf{x}$ refers to a hardening parameter and $\tilde{\mathbf{x}}$ is the corresponding evolution law. A geometric interpretation of the general return mapping method is illustrated in Figure 10.

It is convenient to rewrite the integration steps (25)-(28) in terms of model parameters. From (12) and (20), it follows that the hardening parameter H can expressed by

$$H = p(\mathbf{n} : \widetilde{\boldsymbol{\alpha}} + \sqrt{\frac{2}{3}}\widetilde{m}) \tag{29}$$

The second denominator term in (25) can be simplified by exploiting that stresses are divided in isotropic and deviatoric stresses. Thus, from (11) and (13), the second denominator term becomes

$$\frac{\partial f}{\partial\boldsymbol{\sigma}} : C : \frac{\partial Q}{\partial\boldsymbol{\sigma}} = -NDK + 2G \tag{30}$$

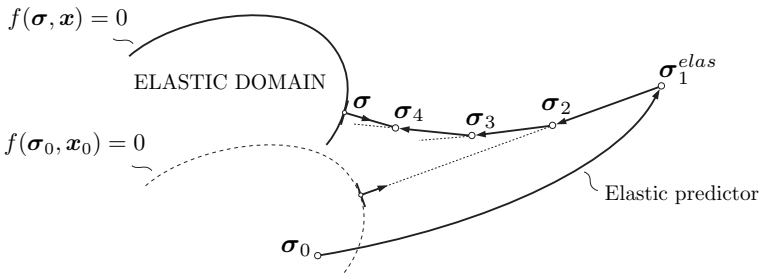

Figure 10. Geometric interpretation of the general return mapping method [29]. An elastic prediction brings the stress state from $\boldsymbol{\sigma}_0$ to $\boldsymbol{\sigma}_1^{elas}$. Subsequently, successive plastic correction steps are applied to return the stress state to the yield surface.

7.2. Integration of elastic relations

The integration of the elastic relations needs special attention due to the p-dependency of the bulk and shear modulus. The resulting isotropic stress p arising from the elastic increment $\Delta\varepsilon_v^e$ can be determined by integration of the elastic relation (11).

$$p = \left(p_0^{1-b} + \frac{1}{p_a^b}(1-b)K_0 \Delta\varepsilon_v^e \right)^{\frac{1}{1-b}} \tag{31}$$

p_0 denotes the isotropic stress at the previous step. The resulting bulk modulus can be calculated subsequently by $K = \Delta p / \Delta\varepsilon_v^e$, with $\Delta p = p - p_0$. If $\Delta\varepsilon_v^e = 0$, then K must be evaluated from (11). The shear modulus scales proportional to the bulk modulus, thus the

---

function ReturnMappingMethod$(\Delta\boldsymbol{\varepsilon}_d,\ \Delta\varepsilon_v)$

Initial state:

$\mathbf{s}_0,\ p_0,\ m,\ \boldsymbol{\alpha},\ \mathbf{z},\ \varepsilon_v,\ \Delta\boldsymbol{\varepsilon}_d^p = \mathbf{0},\ \Delta\varepsilon_v^p = 0$

Update void ratio:

$\varepsilon_v = \varepsilon_v + \Delta\varepsilon_v$

$e = e_0 - (1 + e_0)\varepsilon_v$

Iterations $i = 1, 2, ..., i_{max}$

$p = \left(p_0^{1-b} + (K_0/p_a^b)(1-b)(\Delta\varepsilon_v - \Delta\varepsilon_v^p)\right)^{1/(1-b)}$

$\mathbf{s} = \mathbf{s}_0 + 2G(\Delta\boldsymbol{\varepsilon}_d - \Delta\boldsymbol{\varepsilon}_d^p)$

$\psi = e - (\Gamma - \lambda \ln(p/p_{\text{ref}}))$

If $f(p, \mathbf{s})/p > \epsilon_f$:

Update: $N,\ D,\ K,\ G,\ \mathbf{n},\ \widetilde{\boldsymbol{\alpha}},\ \widetilde{m},\ \widetilde{z}$

Add plastic correction:

$$\Delta\lambda = \frac{f(p,\mathbf{s})}{-NDK + 2G + p(\mathbf{n} : \widetilde{\boldsymbol{\alpha}} + \sqrt{2/3}\widetilde{m})}$$

$$\begin{aligned}
\Delta\boldsymbol{\varepsilon}_d^p &= \Delta\boldsymbol{\varepsilon}_d^p + \Delta\lambda\mathbf{n} \\
\Delta\varepsilon_v^p &= \Delta\varepsilon_v^p + \Delta\lambda D \\
\boldsymbol{\alpha} &= \boldsymbol{\alpha} + \Delta\lambda\widetilde{\boldsymbol{\alpha}} \\
m &= m + \Delta\lambda\widetilde{m} \\
\mathbf{z} &= \mathbf{z} + \Delta\lambda\widetilde{\mathbf{z}}
\end{aligned}$$

Else:

$\mathbf{s}_0 = \mathbf{s}$

$p_0 = p$

return

Table II. The general return mapping method by [29] applied to the modified critical state two-surface plasticity model.

resulting shear stress can be evaluated by

$$\mathbf{s} = \mathbf{s}_0 + 2G\Delta\boldsymbol{\varepsilon}_d^e \qquad G = G_0 \begin{cases} K/K_0 & \text{if } \Delta\varepsilon_v^e \neq 0 \\ (p/p_a)^b & \text{if } \Delta\varepsilon_v^e = 0 \end{cases} \tag{32}$$

The model specific return mapping method, expressed by the above formulations, is outlined in Table II. Note that the return mapping algorithm will continue iterations until $\boldsymbol{\sigma}$ coincides with the yield surface which is evaluated by the criterion $f(p, \mathbf{s}) < \epsilon_f \times p$. Here, ϵ_f specifies a given tolerance. The criterium is chosen to scale proportional to p, since f is evaluated in terms of stress.

8. IMPLEMENTATION STRATEGY

A suitable implementation strategy must be adopted to ensure robustness and efficiency of the integration scheme before actual coding of the plasticity model for computer application. The general return mapping method is only conditionally stable when adopted for the two-surface critical state plasticity model. In general, the return mapping method fails to converge if the imposed strain increment becomes too large. These convergence problems increase as $p \to 0$.

In this paper, most convergence problems are solved by strain-controlled sub-stepping. In general, the imposed increments should be sufficiently small so that sub-stepping on constitutive level is avoided. However, if the isotropic stress level in a single element approaches zero, then extremely small increments must be enforced at the global level to obtain a stable solution. Instead of enforcing a fixed increment size, the local increments are divided into a number of sub-steps as required. The size of each sub-increment is continuously updated from a specified tolerance criterion, so that only the necessary number of sub-increments are applied.

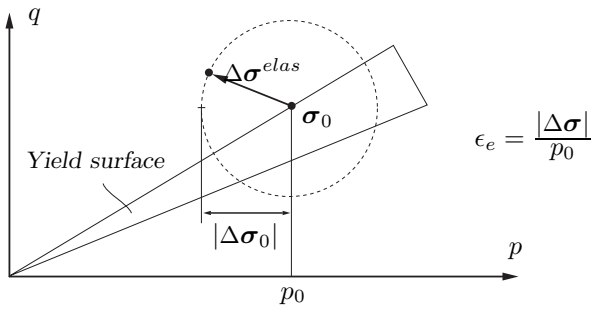

Figure 11. Criterion for initiating a sub-step illustrated in the $p - q$ stress plane

The active sub-step control uses a tolerence criterion based on the magnitude of the elastic prediction $\Delta\boldsymbol{\sigma}^{elas}$, as shown in Figure 11. If the magnitude of the elastic prediction exceeds a given tolerance, the increment is then divided into two sub-increments. The elastic prediction is estimated from the elasticity in the initial state, i.e. $G = G(\boldsymbol{\sigma}_0)$ and $K = K(\boldsymbol{\sigma}_0)$. The criterion initiating sub-steps is defined by $|\Delta\boldsymbol{\sigma}|/p_0 > \epsilon_e$, with ϵ_e specifying a given tolerance. The criterion scales proportional to the isotropic pressure, thus sub-steps are initiated mainly at low stress levels.

The introduction of increment controlled sub-steps ensures that the return-mapping method remains stable. However, the number of sub-steps grows drastically as $p \rightarrow 0$. The high computational costs may be significantly reduced using a stress correction strategy as $p \rightarrow 0$. Here, a stress correction is introduced to prevent p to exceed a lower limit given by $p_{\mathrm{m}} = \epsilon_{\mathrm{m}} p_{\mathrm{ref}}$, in which ϵ_{m} is a specified tolerance criteria. Note that the reference pressure p_{ref} is a constant and may for example be chosen equal to the atmospheric pressure.

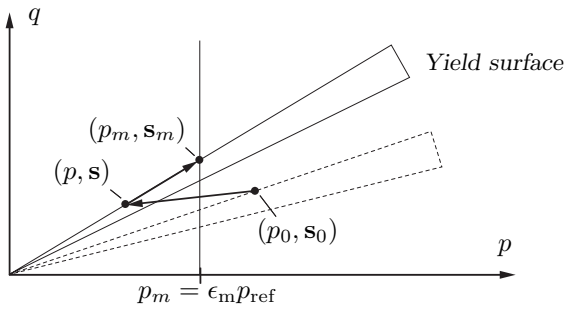

Figure 12. Stress correction for $p \rightarrow 0$ illustrated in the $p - q$ stress plane.

The value of p_m is chosen such that $p_m << p_{\mathrm{ref}}$. If p obtains a value less than p_{m}, then the soil matrix is practically liquefying. In this case, scaling may be applied to translate the stress state from $(p, \mathbf{s})$ to $(p_m, \mathbf{s}_m)$, as illustrated in Figure 12.

$$p_m = \epsilon_{\mathrm{m}} p_{\mathrm{ref}} \qquad \mathbf{s}_m = \left(\frac{p_m}{p} \right) \mathbf{s} \tag{33}$$

This correction strategy may be adopted to significantly reduce the computational costs as cyclic liquefaction evolve. The correction clearly violates the underlying model formulation. However, the correction only slightly changes the model response and may be justified, since validity of the assumptions used to formulate the plasticity model are rather weak for $p \rightarrow 0$. When the correction is applied, the value of $\mathbf{z}$ is simultaneously set to zero ($\mathbf{z} = \mathbf{0}$) since the soil matrix is liquefying. Setting $\mathbf{z}$ to zero effectively resets the ability of the model to recall load history.

Numerical instability occurs if the radius of the yield surface becomes zero or negative ($m \leq 0$). This can occur since the radius of the yield surface is defined to decrease proportionally to the rate of volumetric expansion. Instability can be avoided by setting $\tilde{m} = 0$ in the case where $0 > C_m(1 + e_0)D$ and $m < m_l$. The constant m_l represents a specified lower bound for the size of the yield surface.

An algorithm combining the above mentioned correction strategies is outlined in Table III.

9. EFFICIENCY, ACCURACY AND STABILITY

The performance of the integration scheme is investigated for efficiency, stability and accuracy on a constitutive level. Simulations of conventional cyclic and monotonic triaxial tests,

Initial state:

$\mathbf{s}_0,\ p_0,\ \varepsilon_v,\ m,\ \boldsymbol{\alpha},\ \mathbf{z}$

$\zeta = 0,\ k = 1$

$\Delta\boldsymbol{\varepsilon}_{d,0},\ \Delta\varepsilon_{v,0}$

Iterations $j = 1, 2, ..., j_{max}$

$\Delta\varepsilon_v = \Delta\varepsilon_{v,0}/k$

$\Delta\boldsymbol{\varepsilon}_d = \Delta\boldsymbol{\varepsilon}_{d,0}/k$

$\Delta\boldsymbol{\sigma}^{elas} = \left(2G_0\Delta\boldsymbol{\varepsilon}_d + K_0\mathbf{I}\Delta\varepsilon_v\right)\left(p_0/p_r\right)^b$

If $|\Delta\boldsymbol{\sigma}^{elas}|/p_0 > \epsilon_{\mathrm{e}}$*: Reduce step-length*

$k = 2k$

Else: Start integration

$[s_0,\ p_0] = \mathbf{ReturnMappingMethod}(\Delta\boldsymbol{\varepsilon}_d,\ \Delta\varepsilon_v)$

If $p_0 < \epsilon_{\mathrm{m}} p_{\mathrm{ref}}$*: Add stress correction*

$\mathbf{s}_0 = \epsilon_{\mathrm{m}}(p_{\mathrm{ref}}/p_0)\mathbf{s}_0$

$p_0 = \epsilon_{\mathrm{m}} p_{\mathrm{ref}}$

$\mathbf{z}_0 = \mathbf{0}$

$\zeta = \zeta + 1/k$

Stop iterations when $\zeta = 1$

Final state: $\boldsymbol{\sigma}_0,\ p_0,\ \varepsilon_v,\ m,\ \boldsymbol{\alpha},\ \mathbf{z}$

Table III. Implementation strategy applied to obtain a stable numerical integration scheme

performed in undrained conditions ($\Delta\epsilon_v = 0$), are used for analysis. The adopted model parameters are similar to the parameters used for simulation of Nevada Sand [23, 24]. These are listed in Table IV.

$K_0 = 31.4$MPa	$M_c = 1.1$	$k_b = 4.0$	$A_0 = 2.64$
$G_0 = 31.4$MPa	$\lambda = 0.025$	$k_c = 4.2$	$A_z^{max} = 100$
	$e_r = 0.93$	$C_\alpha = 1200$	$C_z = 100$

Table IV. Model parameters adopted for analysis of efficiency, stability and accuracy.

First, the efficiency and accuracy of the integration scheme (Table II) is investigated. The analysis is based on simulations of monotonic and cyclic tests. The monotonic test simulates a loose sample with the initial confining stress $p = 100$kPa and void ratio $e_0 = 0.82$ while the cyclic test simulates a medium-dense sample with the initial confining stress $p = 150$kPa and void ratio $e_0 = 0.65$. The cyclic test is simulated with a constant shear stress offset ($q = 35 \pm 25$kPa) in order to avoid stability problems when $p \to 0$. The simulations are illustrated in Figure 13.

The accuracy of the return mapping method is evaluated in terms of an error measure

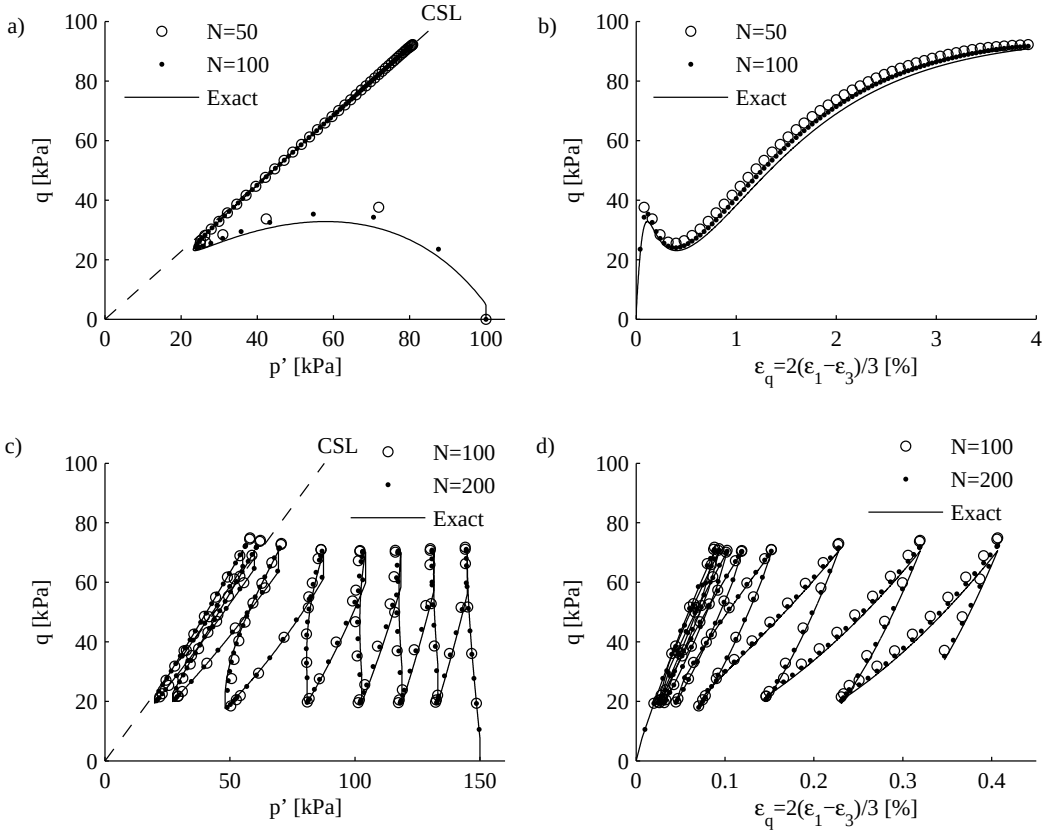

Figure 13. Illustration of simulations used to investigate the accuracy and efficency of the integration scheme. a-b) Monotonic loading. c-d) Cyclic loading

defined by

$$error = \frac{1}{p_{\text{ref}}} \left(\frac{1}{N} \sum_{i=1}^{N} |\boldsymbol{\sigma}_i - \boldsymbol{\sigma}_{i,exact}| \right) \tag{34}$$

where N is the number of steps and $\boldsymbol{\sigma}_{exact}$ refers to the exact solution approximated by simulations having a very small step size. The reference pressure is chosen as $p_{\text{ref}} = 100$kPa. The accuracy is investigated as a function of the imposed strain increments $\Delta\epsilon$ and the resulting step size is quantified in terms of the ratio $\Delta(q/p)_1$ of the initial step. For example, if $\Delta(q/p)_1 = 1.1 = M_{cr}$, then the critical stress ratio is reached in only one step. The results of the simulations are listed in Table V. They indicate that the computational expense, evaluated in terms of total iterations, increases proportional to N. Thus, independent of step length, approximately 2 iterations are on average required at each step. The error decreases potentially with N, see Figure 14a, and proportional to the ratio $\Delta(q/p)_1$, see Figure 14b. The results suggest that a reasonable accuracy, say $error < 2-3\%$, is obtained when the step size is chosen so that $\Delta(q/p)_1 < 0.1$. The tolerance criteria ϵ_f has an influence on efficiency

No.	Loading type	N	$\Delta\varepsilon_1$	$\Delta(q/p)_1$	Iterations	error [%]
1	Monotonic	50	8×10^{-4}	0.52	103	6.2
2	Monotonic	100	4×10^{-4}	0.27	207	3.1
3	Monotonic	200	2×10^{-4}	0.14	413	1.6
4	Monotonic	500	1×10^{-4}	0.066	1023	0.63
5	Monotonic	1000	4×10^{-5}	0.038	2027	0.31
6	Monotonic	5000	8×10^{-6}	0.0075	9794	0.057
7	Cyclic	100	2×10^{-4}	0.13	241	3.2
8	Cyclic	200	1×10^{-4}	0.071	465	1.4
9	Cyclic	500	4×10^{-5}	0.031	1089	0.57
10	Cyclic	1000	2×10^{-5}	0.015	2059	0.28
11	Cyclic	2000	1×10^{-5}	0.0077	3910	0.14
12	Cyclic	5000	4×10^{-6}	0.0031	9439	0.05

Table V. Analysis of accuracy and efficiency as function of step size. ($\epsilon_f = 10^{-4}$)

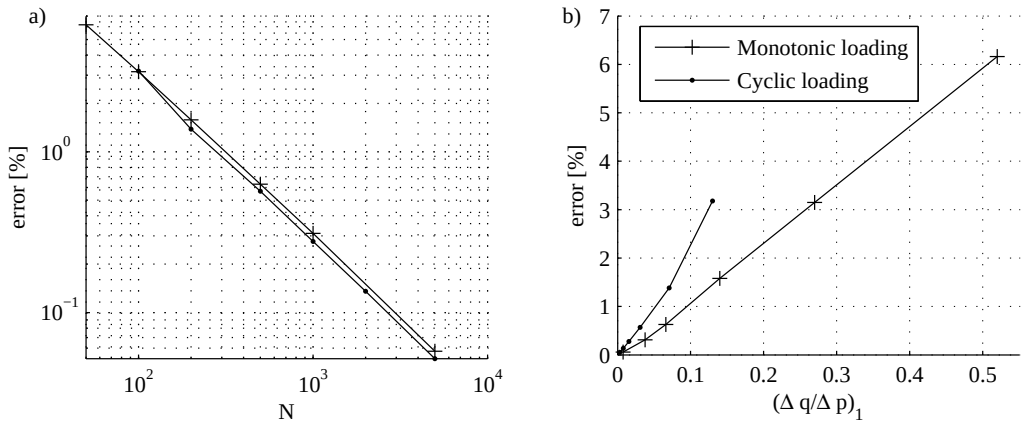

Figure 14. Error of return mapping algorithm as function of N and $\Delta(q/p)_1$.

and accuracy. Table VI lists the results of simulations performed in order to investigate the influence of ϵ_f. The results suggest that a value of $\epsilon_f = 10^{-4}$ is appropriate to optimize

No.	Loading type	ϵ_f	Iterations	ϵ [%]
1	Cyclic	10^{-8}	2725	0.33
1	Cyclic	10^{-6}	2374	0.33
2	Cyclic	10^{-5}	2259	0.33
3	Cyclic	10^{-4}	2059	0.33
4	Cyclic	10^{-3}	1850	0.42
5	Cyclic	10^{-2}	1691	3.3

Table VI. Influence of the tolerance criteria ϵ_f on efficiency and accuracy. The simulations are performed with N=1000 and $\Delta\varepsilon_1 = 2.5 \times 10^{-5}$

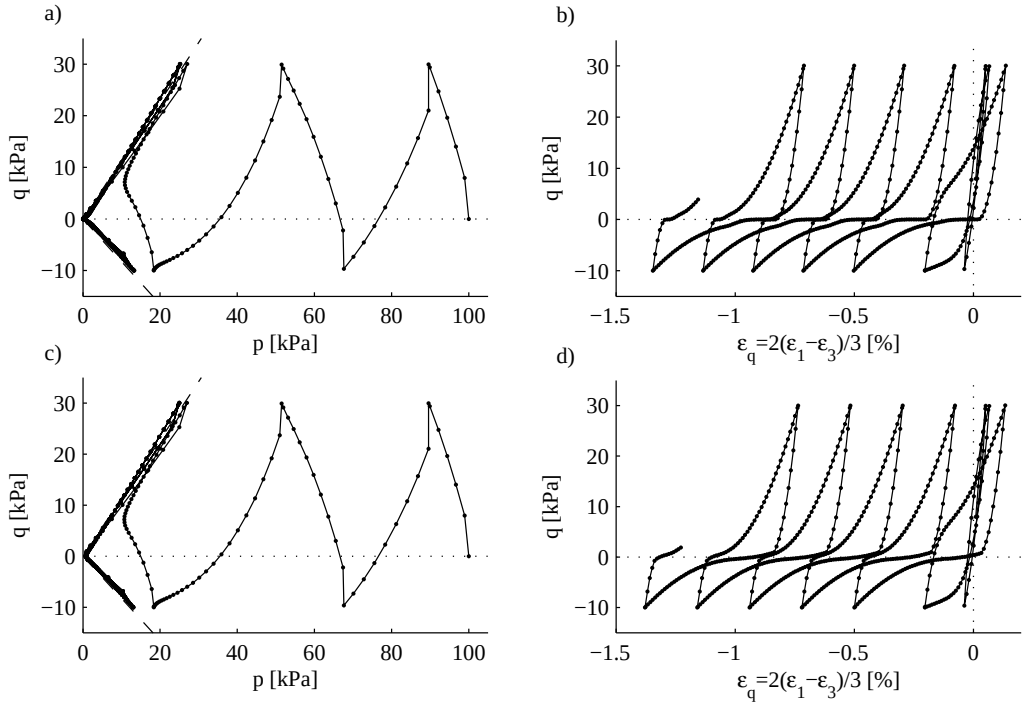

Figure 15. Simulation used in stability analysis. a-b) Simulation no. 6, c-d) Simulation no. 10

efficiency without loosing accuracy.

The stability of the integration scheme and implementation strategy (Table II and III) was tested by simulation of loose and dense samples subjected to a wide range of load histories. Here, an undrained cyclic triaxial test performed on a medium-loose sample ($e_0 = 0.75$) subjected to cyclic loading ($q = 10 \pm 20$kPa) is considered, see Figure 15a and 15b. The cyclic loading causes cyclic liquefaction, which is harsh from a numerical point of view, since $p \to 0$. The value of C_z is set to $C_z = 500$ in order to cause strong contraction during unloading and thereby challenging the stability of the algorithm. Series of simulations are performed to investigate the effect of N, ϵ_e and ϵ_m on stability. The results are listed in Table VII. The simulations 1-3 suggest that reducing the step-length is inappropriate to avoid numerical instability. Even a dramatic decrease in step-size does not ensure convergence. The simulations 4-8 show that the strain-controlled sub-stepping is sufficient in order to avoid numerical instability if the tolerance is chosen so that $\epsilon_{\mathrm{e}} \leq 0.3$. However, the stability is obtained at a relatively high computational cost (minimum 24856 iterations).

The computational costs may be significantly reduced if the stress correction for $p \to 0$ is adopted, ie. $\epsilon_{\mathrm{m}} > 0$. For example, if $\epsilon_{\mathrm{m}} = 0.01$, then the computational costs are reduced to only $3033/24856 = 12\%$. Thus, it may be desirable to adopt this correction strategy if cyclic liquefaction is expected to evolve over a large domain. The correction alters the model response as $p \to 0$, however only slightly. Figure 15c and 15d illustrate a simulation performed with $\epsilon_{\mathrm{m}} = 0.01$ which may be compared with the simulation in Figure 15a 15b performed without

No.	N	$\Delta\varepsilon_1$	ϵ_{e}	ϵ_{m}	Iterations
1	600	10^{-4}	-	-	*
2	6000	10^{-5}	-	-	*
3	60000	10^{-6}	-	-	*
4	600	10^{-4}	0.8	-	*
5	600	10^{-4}	0.5	-	*
6	600	10^{-4}	0.3	-	24856
7	600	10^{-4}	0.2	-	32289
8	600	10^{-4}	0.1	-	61453
9	600	10^{-4}	0.3	10^{-1}	1501
10	600	10^{-4}	0.3	10^{-2}	3033
11	600	10^{-4}	0.3	10^{-3}	5769
12	600	10^{-4}	0.3	10^{-4}	8281
13	600	10^{-4}	0.3	10^{-5}	15761
* No convergence					

Table VII. Results of stability analysis. ($\epsilon_f = 10^{-4}$)

correction for $p \to 0$.

To summarize, a sufficient accuracy of the return mapping method may be obtained if the step-size is chosen such that $\Delta(q/p)_1 < 0.1$ while a combination of $\epsilon_e = 0.3$ and $\epsilon_m = 10^{-2}$ may be a good compromise to ensure both efficiency and stability.

10. CONCLUSION

This paper provides comprehensive background information and documentation for the implementation of the modified critical state two-surface plasticity model as a user-subroutine in the commercial finite difference, FLAC3D by Itasca. The plasticity model is equal to the model by Manzari et al. but uses an alternative multi-dimensional surface formulation. The model parameters are discussed and suggestions for parameter reductions are made. A fast and accurate time-stepping integration scheme suitable for an explicit global solver is presented. The integration scheme is based on the general return mapping method, which is only conditionally stable. Convergence problems are addressed by adopting a suitable implementation strategy consisting of increment controlled sub-stepping. Other correction strategies are introduced, including a correction introduced to increase the efficiency as $p \to 0$. Finally, simulations are made to investigate the performance of the integration scheme and appropriate tolerance criteria are suggested to obtain sufficient efficiency, stability and accuracy. Thus, this paper provides complete information for the implementation of a robust user-defined constitutive model, capable of simulating the response of non-cohesive sands or silts, in a commercial finite element or finite difference code.

REFERENCES

1. Been K, Jefferies MG. A state parameter for sands. *Géotechnique* 1985; **35**(2):99-112
2. Casagrande, A. Characteristics of cohesionless soil affecting the stability of slopes and earth fills. *Journal of Boston Society of Civil Engineering* 1936; **23**(1):13-32
3. Crouch RS, Wolf J, Dafalias Y. Unified critical state bounding surface plasticity model for soil. *Journal of Engineering Mechanics* 1994; **120**(11):2251-2270
4. Dafalias YF, Popov EP. Plastic internal variable formalism of cyclic plasticity. *Journal of Applied Mechanics* 1976; **98**(4):645-650
5. Dafalias YF, Manzari MT. Modeling of fabric effect on the cyclic loading response of granular soils. *Proceedings of ASCE 13th Engineering Mechanics Conference*, Baltimore, Maryland, 13-16 June 1999
6. Dafalias YF, Manzari MT, Papadimitriou AG. SANICLAY: simple anisotropic clay plasticity model. *International Journal for Numerical and Analytical Methods in Geomechanics* 2006; **30**(12):1231-1257
7. Gajo A, Wood DM. A kinematic hardening constitutive model for sands: the multiaxial formulation. *International Journal for Numerical and Analytical Methods in Geomechanics* 1999; **23**(9):925-965
8. Gens, A. Stress-strain and strength of a low plasticity clay. *Ph.D. Thesis* Imperial College, London. 1982
9. De Groot MB, Bolton MD, Foray P, Meijers P, Palmer AC, Sandven R, Sawicki A, Teh TC. Physics of liquefaction phenomena around marine structures. *Journal of Waterway, Port, Coastal and Ocean Engineering* 2006; **132**(4):227-243.
10. Imam SMR, Morgenstern NR, Robertson PK, Chan DH. A critical-state constitutive model for liquefiable sand. *Canadian Geotechnical Journal* 2005; **42**(3):830-855.
11. Lade PV. Elasto-plastic stress-strain theory for cohesionless soil with curved yield surfaces. *International Journal of Solids and Structures* 1977. **13**:1019-1035
12. Lade PV, Ibsen LB. A study of the phase transformation and the characteristic lines of sand behaviour. *Deformation and progressive failure in Geomechanics.* IS-NAGOYA, 1997. Pergamon Press, 353-358
13. Li XS, Dafalias, YF. Dilatancy for cohesionless soils. *Géotechnique* 2000. **50**(4):449-460
14. Matsuoka H, Nakai T. Relationship among Tresca, Mohr-Coulomb and Matsuoka-Nakai failure criteria.*Soils and Foundations* 1985. **25**:123-128
15. Ibsen LB, Lade PV. The role of the characteristic line in static soil behavior. *4" Workshop on localisation and bifurcation theory for soils and rocks.* A.A.Balkema, 1998.
16. Ibsen LB. The mechanism controlling static liquefaction and cyclic strength of sand. *Workshop on the physics and mechanics of soil liquefaction.* A.A.Balkema, 1999.
17. Ibsen LB, Praastrup U. The danish rigid boundary true triaxial apparatus for soil testing. *Geotechnical testing journal* 2002; **25**(3):1-12.
18. Ishihara K, Tatsuoka F, Yasuda, S. Undrained deformation and liquefaction of sand under cyclic stresses. *Soils and Foundations* 1975; **15**(1):29-44.
19. Jefferies, M. G. Nor-Sand: a simple critical state model for sand. *Géotechnique* 1993; **43**(1):91-103.
20. Krenk S. Family of Invariant Stress Surfaces. *Journal of Engineering Mechanics - Proceedings of the ASCE* 1996; **122**(3):201-208.
21. Krenk S. Characteristic state plasticity for granular materials : Part I: Basic theory. *International Journal of Solids and Structures* 2000; **37**(43):6343-6360.
22. Luong MP. Stress-strain aspects of cohesionless soils under cyclic and transient loading. *International symposium on soil under cyclic and transient loading.* A.A.Balkema, 1982.
23. Manzari MT, Dafalias YF. Critical state two-surface plasticity model for sands *Géotechnique* 1997; **47**(2):255-272
24. Manzari MT, Prachathananukit R. On integration of a cyclic soil plasticity model *International Journal for Numerical and Analytical Methods in Geomechanics* 2001; **25**(6):525-549
25. Pestana JM. A unified constitutive model for clays and sands. *Ph.D. Thesis* MIT, Cambridge, Mass. 2000.
26. Praastrup, U. Three dimentional stress-strain behavior of soils tested in the danish rigid boundary true triaxial apparatus. *Ph.D. Thesis, Geotechnical engineering group, Aalborg University.* Aalborg University, 2000.
27. Roscoe KH, Schofield AN, Wroth CP. On yielding of soils *Géotechnique* 1958; **8**(1):22-53.
28. Schofield AN, Wroth CP. *Critical State Soil Mechanics* McGraw-Hill, London, 1968.
29. Simo JC, Ortiz M. A unified approach to finite deformation elastoplastic analysis based on the use of hyperelastic constitutive equations. *Computer Methods in Applied Mechanics and Engineering* 1985; **49**(2):221-245
30. Taiebat M, Shahir H, Pak A. Study of pore pressure variation during liquefaction using two constitutive models for sand. *Soil Dynamics and Earthquake Engineering* 2006; **27**(1):60-72
31. Wan RG, Guo, PJ. A simple constitutive model for granular soils: modified stress-dilatancy approach. *Computers and Geotechnics* 1998; **22**(2):109-133

32. Wood DM, Belkheir K, Liu DF. Strain softening and state parameters for sand modelling *Géotechnique* 1994; **44**(2):335-339
33. Wroth CP, Randolph MF, Houlsby GT, Fahey M. A review of the engineering properties of soils woth particular reference to the shear modulus. *Tech. Report CUED/D-SOILS TR75*, University of Cambridge, 1979
34. Wroth CP, Houlsby MF. Soil mechanics: property characterisation and analysis procedures. *Proc. 11th Int. Conf. Soil Mech. Found. Engng.*, San Francisco, May 1985, pp. 1-50

PAPER IV

LeBlanc, C. & Randolph, M. F.

Interpretation of piezocones in silt, using cavity expansion and critical state methods

Proceedings of the 12th International Conference of International Association for Computer Methods and Advances in Geomechanics (IACMAG), 1st - 6th October 2008, Goa, India. 822-829.

Silt from Horns Rev 2 Offshore Wind Farm

The 12th International Conference of
International Association for Computer Methods and Advances in Geomechanics (IACMAG)
1-6 October, 2008
Goa, India

Interpretation of Piezocones in Silt, using Cavity Expansion and Critical State Methods

C. LeBlanc
Offshore Technology, D.O.N.G. Energy & Dept. of Civil Engineering, Aalborg University, Aalborg, Denmark

M. F. Randolph
Centre for Offshore Foundation Systems, University of Western Australia, Perth, Australia

Keywords: piezocone, silt, cavity expansion, state parameter

ABSTRACT: Silt sediments are frequently encountered in the coastal areas of the North Sea. Evaluation of the silt behaviour must ideally rely on in-situ tests, in particular the piezocone test. However, interpretation of piezocone data in silt sediments is problematic and derived parameters can seem to differ significantly from those obtained by investigating intact samples in the triaxial apparatus. Use of the state parameter ψ in conjunction with the critical state line provides a precise definition for the state of silt, and thereby important aspects, such as resistance to cyclic liquefaction. The objective of this paper is to provide a site-specific correlation between the dimensionless group of piezocone parameters $(q_t-u_2)/p'$ and the in-situ state parameter ψ_0, while accounting for partial drainage during penetration. Silt from the North Sea was used as a case study. The process of penetration was simulated using cylindrical cavity expansion in conjunction with a plasticity model formulated within the framework of critical state soil mechanics. The results readily explain the low cone tip resistance measured in silt sediments; this is a derived effect of the silt having a large slope of the critical state line, resulting in rather weak and compressible behaviour at high mean effective stresses.

1 Introduction

Wind power currently offers a very competitive source of renewable energy, and therefore the market for onshore and offshore wind farms is projected to expand rapidly within the next decade. There are strong political and industrial forces, especially in northern Europe, supporting the development of offshore wind farms to reduce the reliance on fossil fuels and control greenhouse gas emissions. Most current foundations for offshore wind turbines (OWTs) are “monopiles”, which are stiff piles with large diameters, typically 4 - 6 m, as illustrated in Figure 1. It is characteristic for offshore wind turbines that the sub-structure is subjected to strong cyclic loading, originating from wind and wave loads.

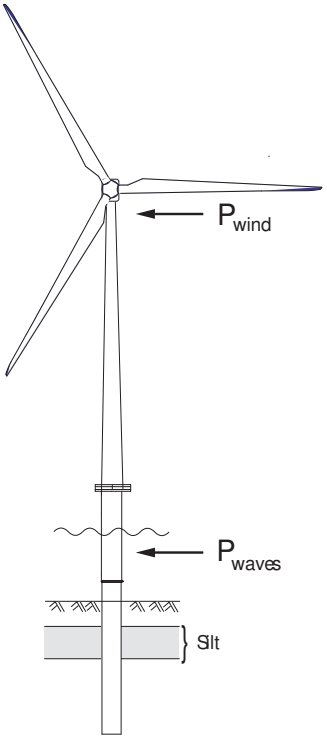

Figure 1 . Offshore wind turbine on monopile foundation.

The geotechnical investigations for future offshore wind farms are generally performed in the pre-investment stage and are thus kept to a minimum. The most widely used in-situ investigation device for the estimation of soil classification and geotechnical parameters is the piezocone (CPTu). A piezocone is pushed into the ground at a constant rate, while the cone resistance, sleeve friction and pore pressures are measured. Typically, a single piezocone test is performed at each wind turbine location and it is supplemented with few scattered borings throughout the site. Silt sediments are frequently encountered in the coastal areas of the North Sea, typically at depths 5 - 15 m. Generally, the geotechnical properties of silt are less understood and more difficult to measure than those of sand and clay. Though the shear strength properties of silt are comparable to those of sand, and the volumetric compression properties are comparable to those of clay, large variations occur in silt due to its general composition, with varying fines content and permeability.

Interpretation of piezocone data in silt layers is difficult due to the complex deformation of the soil around the cone during penetration combined with the effect of drainage conditions in saturated soil. In practice, methods for piezocone interpretation in sands and clay are primarily based on empirical

correlations between soil properties and the piezocone quantities q_t, f_s and u_2, the corrected cone tip resistance, the sleeve friction and the dynamic pore pressure measured at the cone shoulder, respectively (Lunne et al., 1997). During cone penetration, it is generally assumed that the response of clean sand is governed by fully drained conditions, whereas clay is governed by fully undrained conditions. A soil consisting of silt represents an intermediate soil, between sand and clay, in which cone penetration takes place under partially drained conditions at a standard rate of penetration (20 mm/s). Under partially drained conditions, the soil behaviour is affected by the degree of pore pressure dissipation during cone penetration. When almost undrained conditions govern cone penetration, it is most obvious to interpret the soil strength in terms of the undrained shear strength. However, an effective strength approach for silt is often more applicable for design application, as drainage occurs over long time scales. Obtaining effective strength parameters from an almost undrained cone penetration is conceptually difficult; therefore methods for interpretation of piezocone tests in silt are limited and not well established.

The primary design drivers for OWT foundations are those of deformation and stiffness rather than ultimate capacity. Modern OWTs are designed as "soft-stiff" structures, meaning that the 1st natural frequency is in the range between the excitation frequency bands, 1*P* and 3*P*, in order to avoid resonance. 1*P* and 3*P* denote the frequency bands of the rotor rotation and the blade passing, respectively. Any significant change in stiffness may result in interference between the 1st natural frequency and the excitation frequency, 1*P* or 3*P*, which can be highly problematic. The design of an OWT foundation must therefore be undertaken carefully in order to obtain a foundation stiffness within a specified stiffness range, prescribed by both an upper and lower bound. A conservative design may not be an option, and it is therefore important to determine the in-situ soil conditions accurately. In silt layers, it is necessary to develop a site-specific piezocone correlation to interpret the piezocone data. However, parameters derived from piezocone data in silt sediments may seem to differ significantly from those obtained by investigating intact samples in the triaxial apparatus. This raises the question whether the parameters derived from triaxial tests represent the in-situ state or a disturbed state, as it can be difficult to obtain and subsequently establish a silt sample in a triaxial apparatus without disturbing the in-situ conditions.

The presence of loose silt is particularly problematic as it imposes the risk of cyclic liquefaction or mobility developing in response to cyclic loading originating from the wind turbine (e.g. Groot et al., 2006). An inevitable consequence is that the natural frequency of the structure decreases and perhaps coincides with the excitation frequencies of the rotor. This is not acceptable and therefore, sites with loose silt are currently avoided. Soil liquefaction is a major concern in areas exposed to earthquakes. The most commonly used technique for assessing the risk of soil liquefaction is developed on the basis of an extensive database of empirical data from SPTs and CPTs performed at sites that either had or had not experienced liquefaction due to earthquake loading. However, the correlations are not applicable to assess the risk of cyclic liquefaction induced by the cyclic loading of an OWT, as neither the type of cyclic loading, duration of loading nor drainage conditions are comparable. Thus, a more fundamental approach is required.

1.1 Critical state interpretation of silt sediments

Critical state soil mechanics (CSSM), (Roscoe et al. 1958; Schofield and Wroth, 1968), provides a broad framework for explaining the fundamental behaviour of fine-grained materials. Within CSSM, the variation of critical void ratio e_{CSL} and the mean effective stress p is assumed linear in e-ln(p) space, as defined by the critical state line (CSL):

$$e_{CSL} = \Gamma - \lambda \ln(p / p_{ref}) \quad (1)$$

in which p_{ref} = 1 kPa. The constants λ and Γ denote the line inclination and the void ratio at unit mean effective stress, respectively. An essential parameter arising from CSSM is the state parameter $\psi = e\text{-}e_{CSL}$ (Been and Jefferies, 1985). At a given void ratio and mean effective stress, the state parameter describes whether the soil is dilative or contractive at large strains, and is used to substitute the concept of relative density. The resistance to cyclic liquefaction is highly influenced by the state parameter and the lowest resistance is obtained for $\psi > 0$. Empirical evidence shows that the liquefaction resistance is also affected by the presence of fines (Seed et al., 1985). The fines may either be plastic or non-plastic and the weight percentage of fines varies. The effect of non-

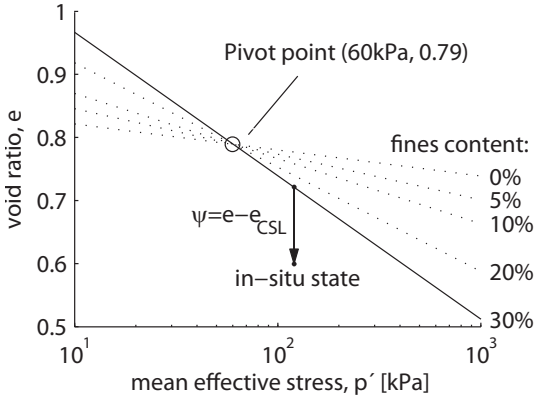

Figure 2 . Illustration of state parameter and variation of critical state line with fines content.

plastic fines content (up to at least 30% by weight) can be interpreted from CSSM as a rotation of the CSL around a fixed pivot point in e-ln(p) space (Bouckovalas et al., 2003) (Figure 2). This implies that a high content of fines increases the tendency for dilation for mean effective stresses lower than that of the pivot and decreases it for mean effective stresses higher than the pivot.

Thus, use of the state parameter ψ in conjunction with the critical state line, provides a precise definition for the state of silt. Interpretation of piezocone data should therefore rely on the CSSM parameters – in particular the state parameter – to assess the in-situ state of the silt sediments and thereby, important aspects, such as resistance to cyclic liquefaction. Been et al. (1986; 1987) proposed a method for estimating the state parameter for cone penetration tests in sand, based on the dimensionless cone penetration resistance $Q_p = (q_t-p_0)/p'_0$ in which p'_0 represents the in-situ mean effective stress level. This method provides a direct relation between Q_p and the in-situ state parameter ψ_0 by:

$$Q_p = k \exp(-m\psi_0) \tag{2}$$

in which m and k are dimensionless soil-specific parameters to be determined from the steady state line obtained from a series of triaxial tests. This appears to be a very useful approach; however, the relationship is only applicable under fully drained conditions. Houlsby (1988) suggested that $(q_t-u_2)/\sigma'_{v0} = Q(1-B_q)+1$ represents a fundamental dimensionless group for interpretation of undrained penetration. However, the group $Q(1-B_q)+1$ is normalized with respect to σ'_{v0} and therefore eliminates any influence of the geostatic stress ratio K_0, and thereby the mean effective stress p'. This is problematic as ψ is a function of p'. Calibration tests have shown that the influence of K_0 becomes negligible when normalizing with respect to p' rather than σ'_{v0} (Clayton et al., 1985; Been et al., 1986). Therefore, Been et al. (1988) proposed that $Q_p(1-B_q)+1$ relates to ψ_0, analogously to Q_p in (2). This relation was confirmed using cavity expansion theory (Shuttle and Cunning, 2007). However, the definition of the group $Q_p(1-B_q)+1$ is inconsistent, as Q_p is defined in terms of p'_0, while B_q is defined in terms of σ'_{v0}. A more consistent approach, adopted in this paper, is to simply relate ψ_0 to the dimensionless group $(q_t-u_2)/p'_0$ by:

$$\frac{q_t - u_2}{p'_0} = k_u \exp(-m_u\psi_0) \tag{3}$$

in which k_u and m_u are dimensionless soil-specific parameters.

This paper presents a numerical study of piezocone penetration in silt sediments encountered in the North Sea, close to the Danish coastline. The objective is to establish a site-specific correlation between measured piezocone parameters, in terms of $(q_t-u_2)/p'$ and the in-situ state of the silt sediments, in terms of the state parameter ψ_0. The piezocone penetration is simulated, assuming axial symmetry conditions, allowing the process of cone penetration to be modelled as a cylindrical cavity expanding in a saturated two-phase soil, using the commercial finite difference code FLAC3D (Itasca, 2005). Intact samples of the silt sediments were tested in the triaxial apparatus and simulated, using the modified critical state two-surface plasticity model for sand (Manzari and Dafailas, 1997; LeBlanc et al., unpublished), implemented as a user sub-routine in FLAC3D. A series of calculations were performed to investigate piezocone penetration in drained, undrained and partially drained conditions and determine representative values of k_u and m_u.

2 Numerical simulation of piezocone using the method of cavity expansion

Several theories, with different degrees of simplifying assumptions, are available for the analysis of cone penetration. Numerical methods for simulating cone penetration include cavity expansion, steady state solution and large strain finite element methods. In a cylindrical cavity expansion approach, the process of penetration is assumed equivalent to the creation of a cavity under axial symmetry conditions. It is generally accepted, that the method of cavity extension is capable of estimating cone penetration resistance (Yu, 2000; Yu and Mitchell, 1998). In this paper, the process of penetration is modelled as a cylindrical cavity expanding in a saturated two-phase soil to simulate a standard piezocone, that is, a cone having a diameter d = 35.7 mm, tip angle $\alpha = 60^0$ and penetration velocity v = 20 mm/s. This approach is similar to that followed by Silva et al. (2006). The cavity expansion model is built in FLAC3D, using 50 zones, decreasing logarithmically in size towards the cavity. The model allows for dynamic pore-pressure generation by simulating the coupled fluid-mechanical behaviour, using Darcy's law for isotropic fluid transport (Itasca, 2005). Each simulation is conducted using 100,000 mechanical steps and the fluid flow equations were solved simultaneously using one or more sub-steps after each mechanical step. This model is schematically illustrated in Figure 3.

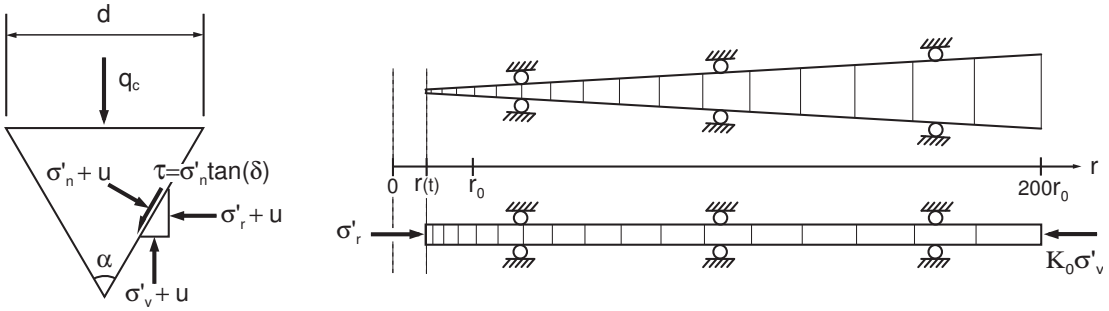

Figure 3 . Schematic illustration of stresses acting on the cone and the FLAC3D cavity expansion model.

The prescribed initial conditions are the hydrostatic pressure u_0, the vertical effective stress σ'_{v0} and the horizontal effective stress $K_0\sigma'_{v0}$. The prescribed stress acting on the outer boundary is $K_0\sigma'_{v0}$. The cavity is expanded radially from an infinitely small radius, simulated as an initial, very small radius ($r = 0.01r_0$), to the radius of the piezocone ($r_0 = d/2$). At time *t,* the radius is expanded by the magnitude $r(t) = \tan(\alpha/2)vt$, in order to simulate realistic drainage time scales. During the strain-controlled expansion, the radial stress σ'_r and pore pressure *u*, acting in the cavity, are measured as functions of the displaced distance *r*. The pore pressure acting in the cavity, when expanded to $r = r_0$, is assumed to approximate the pore pressure u_2, measured at the shoulder of the piezocone. The cone tip resistance q_t is determined from the vertical projection of all forces acting on the cone. It is assumed that the radial and vertical effective stresses, σ'_r and σ'_v, respectively, are principal stresses. Integration over *r* allows q_t to be determined from:

$$\left(\tfrac{1}{4}\pi d^2\right) q_t = 2\pi \int_0^{r_0} (\sigma'_v + u)\, r\, dr \tag{4}$$

The frictional stresses acting on the cone during penetration depend on the interface friction angle δ and the effective normal stress σ'_n. Using $\tau=\sigma'_n\tan(\delta)$, an expression for σ'_v in terms of σ'_r can be obtained by eliminating σ'_n, using the equations of horizontal and vertical force equilibrium in a point along the cone:

$$\sigma'_v = \sigma'_r \,(1+\tan(\delta)/\tan(\tfrac{\alpha}{2}))/(1-\tan(\delta)\tan(\tfrac{\alpha}{2})) \tag{5}$$

A benchmark analysis by Yu and Mitchell (1998) showed that the best agreement between a cavity expansion solution and field observations was obtained for a perfectly rough cone. This suggests that the interface friction angle δ should be chosen equal to the critical state angle of friction ϕ_{cs}, as adopted in this paper; this may be slightly conservative.

3 Constitutive modelling

A continuum-based constitutive model formulated within the framework of non-associated elasto-plasticity and CSSM, is adopted to simulate the behaviour of silt (LeBlanc et al., unpublished). The underlying model formulation is similar to the versatile and yet simple critical state two-surface plasticity model for sands by Manzari and Dafalias (1997) and Manzari and Prachathananukit (2001). The model has proved to simulate drained and undrained stress-strain behaviour of sands successfully under monotonic (and cyclic) loading, over a wide range of confining stresses and densities. The plasticity model is formulated using the CSL defined in (1) and adopts ψ as a fundamental model parameter. The elastic behaviour is based on a hypo-elastic formulation by which the bulk and shear modulus are defined by $K = K_r(p/p_a)^b$ and $G = G_r(p/p_a)^b$, respectively, in which *b* is the pressure exponent and p_a is the atmospheric pressure for which $K = K_r$ and $G = G_r$. The elastic domain is enclosed by a yield surface with a cone-type shape with the apex at the origin, defined by:

$$f = |s - \alpha p| - \sqrt{2/3}\, mp = 0 \tag{6}$$

in which *s* is the deviatoric stress and α is a back-stress tensor defining the direction of the cone. The value of *m* defines the size of the yield surface. A bounding and a characteristic surface are defined in terms of the stress ratios $M = q/p$ in triaxial compression by:

$$M_{bound} = M_{CSL} + k_b\langle -\psi \rangle \tag{7}$$

$$M_{char} = M_{CSL} + k_c\psi \tag{8}$$

in which k_b and k_c are model parameters and M_{CSL} is the critical stress ratio. This formulation ensures increased peak shear strength for densely packed sands. It is assumed that the critical state angle of friction Φ_{CSL} is approximately the same under conditions of triaxial extension and compression. This assumption is used to formulate surfaces in stress space in terms of the lode angle θ. The surfaces are used to define thresholds for the back-stress tensor rather than the stress tensor. An outline of the yield, bounding and characteristic surfaces is illustrated in Figure 4. The direction of plastic flow is defined by:

$$\frac{\partial g}{\partial \sigma} = \mathrm{n} + \frac{1}{3}\mathrm{DI} \qquad (9)$$

in which *g* denotes the plastic potential, *I* the identity matrix and *n* the deviatoric normal to the yield surface. The parameter *D* controls the isotropic flow direction and thus the volumetric behaviour of the plasticity model. The definition $D = A_0(\beta_c:n)$, in which A_0 is a model parameter, implies that the characteristic surface becomes the threshold between compressive and dilative behaviour for monotonic loading. The model adopts kinematic hardening, based on a proposition defining the evolution of α by

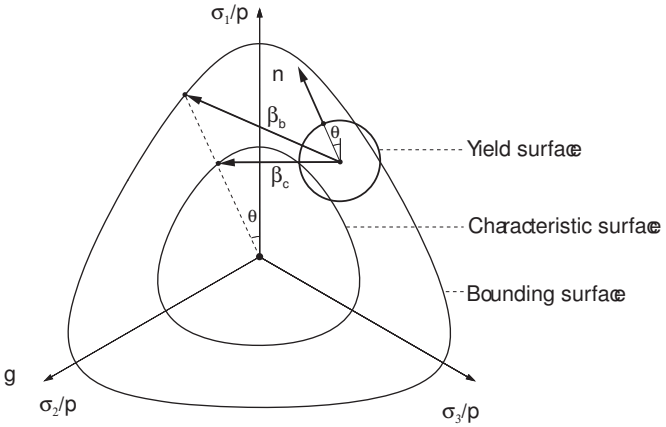

Figure 4 . Outline of surfaces in the octahedral stress plane.

$$\tilde{\alpha} = C_\alpha \left(\frac{|\beta_b : \mathrm{n}|}{b_r - |\beta_b : \mathrm{n}|} \right) \beta_b \qquad b_r = 2\sqrt{2/3}(M_{bound} - m) \qquad (10)$$

in which C_α is a positive model parameter. The model is implemented in FLAC3D as a user-defined sub-routine, using an integration scheme based on an explicit return mapping method. Suitable correction strategies are applied to make the integration scheme stable and efficient.

4 Model calibration for silt samples

The constitutive behaviour is evaluated using intact samples of silt sediments originating from Horns Rev in the North Sea at a depth of 5.2-5.6 m below seabed. The samples were obtained using a vibrocore technique and could possibly have been disturbed before testing. The samples consisted of very silty, fine sand, with a mean particle diameter, $D_{50} \approx 0.07$ mm, a water content, $w \approx 25\%$ and a non-plastic fines content, $f(\%) \approx 45\%$. The silt had a low plasticity index, $I_P \approx 5.8\%$. A total of three triaxial CD tests were undertaken on cylindrical specimens with a height of 70 mm and a diameter of 70 mm, and bounded by smooth pressure heads. The samples were tested in triaxial compression after an initial K_0-consolidation, to reach an in-situ geostatic stress ratio of $K_0 = 0.42$ and vertical effective stress levels of 50, 100 and 150 kPa. All samples exhibited a strong dilative behaviour which indicated that the tested state was denser than the critical state. Direct interpretation of triaxial data to determine the critical state parameters of dense silt is problematic. It requires a constitutive model based on the critical state assumptions (Been et al. 1992). The critical state parameters are therefore determined from model calibration. The adopted model parameters are listed in Table 1 and the triaxial data and simulations are illustrated in Figure 5.

Table 1 . Model parameters.

Elastic parameters			Critical state parameters			Dilatancy	Kinematic hardening	Others		
K_r [MPa]	G_r [MPa]	B	M_{CSL} [-]	λ [-]	Γ [-]	A_0 [-]	C_α [-]	k_b [-]	k_c [-]	m [-]
15	7.5	0.5	1.33	0.048	0.987	0.84	88	6.1	1.2	0.15

The model calibration led to an estimated state parameter for the silt sediments of $\psi_0 \approx -0.14$. The determined position of the CSL line correlated well with the postulated existence of a CSL pivot point (Bouckovalas et al. 2003).

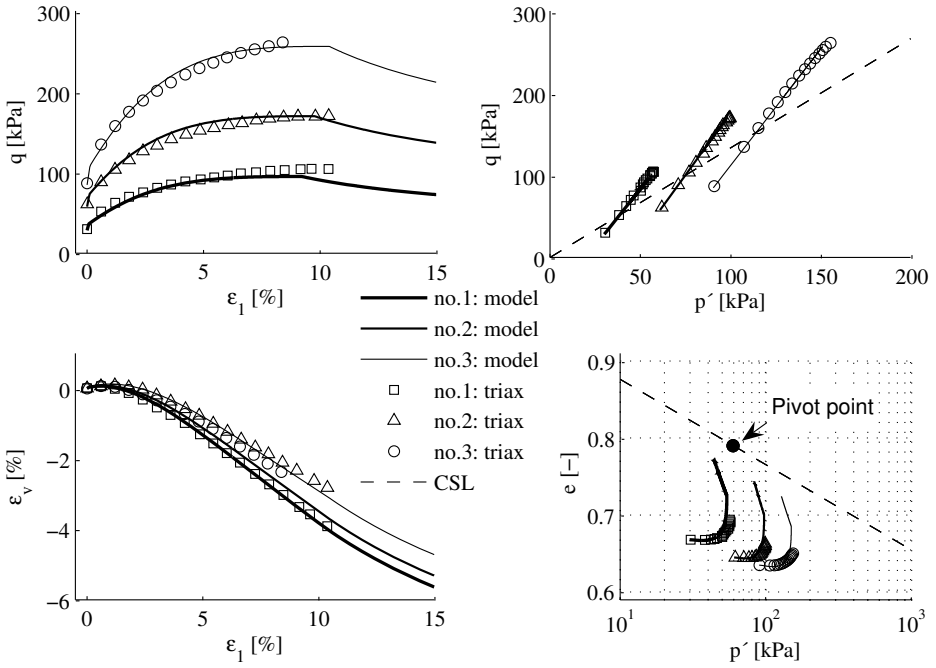

Figure 5 . Model calibration of three drained consolidated triaxial tests on Horns Rev silt.

5 Discussion

Simulations using the cavity expansion model are conducted to determine the pore pressure u_2 and the cone resistance q_t numerically in order to evaluate the dimensionless group $(q_t-u_2)/p'_0$. An example of the calculated radial stress distribution immediately after cone penetration is shown in Figure 6a for $k = 10^{-6}$ m/s, illustrating the gradual transformation from negative to positive pore pressures building up in response to the transformation from dilative to contractive behaviour. The degree of drainage during penetration can be interpreted using the non-dimensional cone penetration velocity $V=vd/c_h$, which may be used to estimate the transition from drained (V≈0.03) to undrained (V≈30) penetration (House et al., 2001; Randolph and Hope, 2004; Silva et al., 2006). The controlling parameter is the coefficient of consolidation c_h which is influenced by both permeability and soil stiffness; thereby also the mean effective stress level. Appropriate values of c_h were determined by numerical simulation of one-dimensional consolidation tests, assuming that a representative consolidation pressure is equal to the mean effective stress governing in the cavity when fully expanded ($r=r_0$). Though the permeability remains constant ($k = 10^{-6}$ m/s), there are large differences in the non-dimensional velocity (V=0.22-1.8); this is an effect of c_h dependency on both ψ_0 and the mean effective stress level.

A total of 28 simulations are performed to investigate the influence of permeability k and the state parameter ψ_0, as illustrated in Figure 6b. All simulations are conducted using the initial conditions σ'_{v0} = 100kPa and K_0 = 0.42. The results of the simulations are seen to form reasonably straight lines, confirming the expression postulated in equation (3). The slope of the undrained curve is higher compared to the drained curve. This is expected, as a dilative behaviour in undrained conditions causes negative pore pressure and thus an increased mean effective stress level in response to a volumetric expansion. This results in higher shear strength and thus higher cone resistance. The opposite effect governs for contractive behaviour in undrained conditions. For dense states ($\psi_0 \approx -0.2$), the transition from undrained to drained behaviour is found to occur in the range from $k = 10^{-5}$ m/s to $k = 10^{-8}$ m/s, corresponding to V = 0.03 and V = 13, respectively. While the permeability range is in good agreement with the empirical evidence reported by McNeilan and Bugno (1985), which suggested that partially drained conditions prevail between $k = 10^{-5}$ and $k = 10^{-8}$ m/s for cone penetration in silt, the normalised velocity of V = 13 lies somewhat below the usually accepted limit of 30 for undrained behaviour (House et al., 2001). For loose states ($\psi_0 \approx 0.1$), the transition is seen to occur at lower values of permeability in the range from $k = 10^{-4}$ m/s to $k = 10^{-7}$ m/s, corresponding to V = 0.01 and V = 19, respectively. The range of V in which partial drainage prevails, for dense and loose states, falls close the expected range of $0.03 < V < 30$.

A piezocone test was performed at the location where the tested silt samples were obtained. The measured piezocone parameters and derived values are illustrated in Figures 7a-7c. The measured cone resistance was

very low ($q_t \approx 1$ MPa) and excess pore pressures built up during penetration in the silt layers. The low cone resistance may seem contradictory to the strong dilation and high friction angle ($\Phi \approx 38^0$-39^0) measured in the triaxial apparatus. Unfortunately, no dissipation tests were performed. The permeability of the silt sediment is therefore estimated from charts (Robertson et al., 1986) to be in the range 10^{-5} m/s < k < 10^{-6} m/s. A representative value of $k = 10^{-6}$ m/s is assumed and used to determine the site-specific correlation between ψ_0 and the value of $(q_t\text{-}u_2)/p'_0$ as illustrated by the dotted line in Figure 6b. This correlation is expressed by (3), using the values $k_u = 14$ and $m_u = 12$. The correlation is applied to interpret the measured piezocone parameters and estimate the in-situ state of the silt sediments in terms of ψ_0, (Figure 7d). At a depth of 5.5 m, the in-situ state parameter is determined as $\psi_0 \approx$ -0.10, based on the ψ_0-correlation to piezocone parameters. In comparison, the state parameter determined from the triaxial tests is ψ_0 = -0.14.

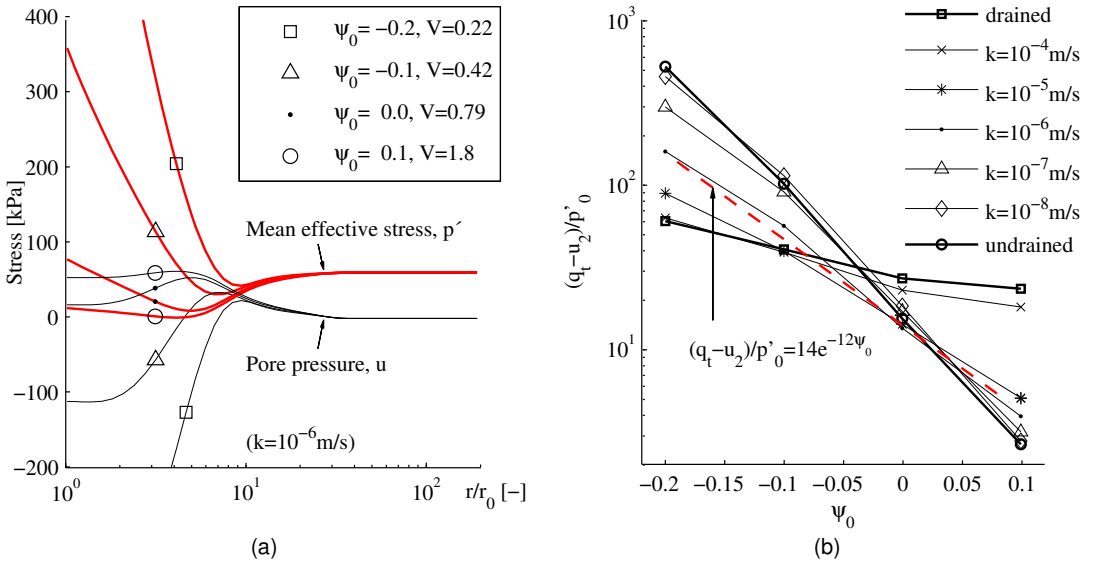

Figure 6 . (a) Radial distribution of stresses after cavity expansion in partially drained conditions ($k = 10^{-6}$ m/s). (b) Estimated value of $(q_t\text{-}u_2)/p'_0$ as a function of the in-situ state parameter ψ_0 and permeability coefficient k.

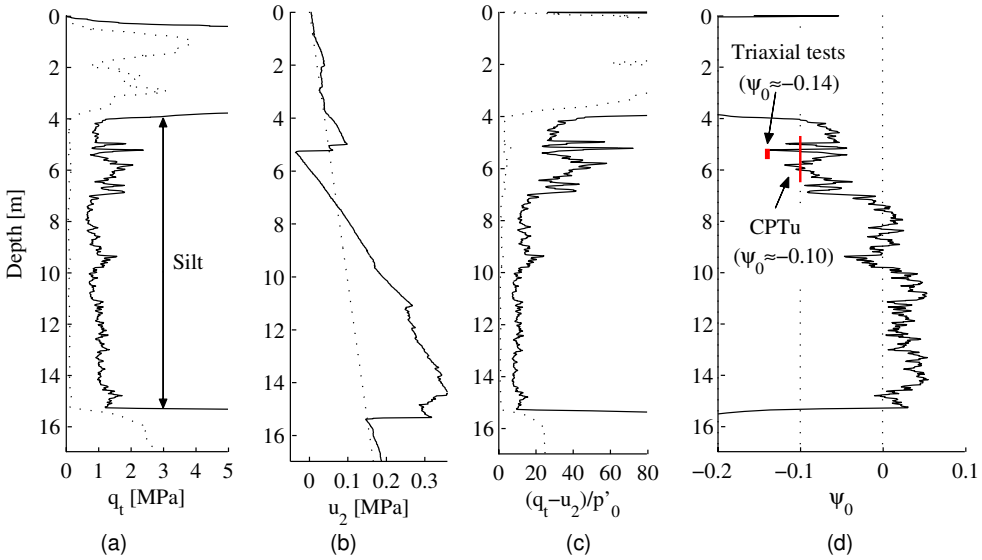

Figure 7 . a) Cone tip resistance. b) Measured and hydro-static pore pressure. c) The dimensionless group $(q_t\text{-}u_2)/p'_0$. d) Site-specific correlation between ψ_0 and piezocone parameters.

These results agree very well, in the light of the assumptions made by the cavity expansion analysis. The discrepancy can be explained by a slightly higher drainage than assumed, either due to a lower permeability or spherical drainage during penetration. The comparison suggests that the tested silt samples are representative of a lightly disturbed state. Thus, the seemingly contradictory evidence of low cone resistance and high triaxial shear strength can readily be explained by a cavity expansion analysis formulated within the framework of CSSM. The low cone resistance is a derived effect of the silt having a large slope of the CSL, resulting in rather weak and compressible behaviour at high mean effective stresses.

6 References

Been K., Jefferies M.G. 1985. A state parameter for sands, *Geotechnique*, **35**(2), 99-112.

Been K., Crooks J.H.A., Becker D.E., Jefferies M.G. 1986. The cone penetration test in sands: Part I. State parameter interpretation, *Geotechnique*, **36**(2), 239-249.

Been K., Jefferies M.G., Crooks J.H.A., Rothenburg L. 1987. The cone penetration test in sands: Part II. General inference of state, *Geotechnique*, **37**(3), 285-299.

Been K., Crooks J.H.A., Jefferies M.G. 1988. *Penetration testing in the UK: Interpretation of material state from the CPT in sands and clays*, Thomas Telford, London (UK).

Been K., Jefferies M.G., Hachey J. 1992. Discussion: The critical state of sands, *Geotechnique*, **42**(4), 655-663.

Bouckovalas G.D., Andrianopoulos K.I., Papadimitriou A.G. 2003. A critical state interpretation for the cyclic liquefaction resistance of silty sands, *Soil Dynamics and Earthquake Engineering*, **23**(2), 115-125.

Clayton C.R.I., Hababa M.B., Simons N.E. 1985. Dynamic penetration resistance and the prediction of the compressibility of a fine-grained sand – a laboratory study, *Geotechnique*, **35**(1), 19-31.

De Groot M.B., Bolton M.D., Foray P., Meijers P., Palmer A.C., Sandven R., Sawicki A., Teh T.C. 2006. Physics of liquefaction phenomena around marine structures, *Journal of Waterway, Port, Coastal and Ocean Engineering,* **132**(4), 227-243.

Houlsby G.T. 1988. *Penetration testing in the UK: Introduction to papers 14-19*, Thomas Telford, London (UK).

House A.R., Oliveria J.R.M.S., Randolph MF. 2001. Evaluating the coefficient of consolidation using penetration tests, *International Journal of Physical Modelling in Geotechnics,* **1**(3), 17-25.

Itasca. 2005. *FLAC3D - Fast lagrangian analysis of continua: Fluid-Mechanical Interaction,* Itasca Consulting Group Inc., Minneapolis (USA).

LeBlanc C., Hededal O., Ibsen L.B. A modified critical state plasticity model for sand - theory and implementation, *Submitted for publication*.

Lunne T., Robertson P.K., Powell J.J.M. 1997. *Cone penetration testing in geotechnical practice*, Blackie Academic & Professional, London (UK).

Manzari M.T., Dafalias Y.F. 1997. Critical state two-surface plasticity model for sands, *Geotechnique*, **47**(2), 255-272.

Manzari M.T., Prachathananukit R. 2001. On integration of a cyclic soil plasticity model, *International Journal for Numerical and Analytical Methods in Geomechanics*, **25**(6), 525-549.

McNeilan T.W., Bugno W.T. 1985. *Strength Testing of Marine Sediments: Laboratory and In-Situ Measurements, Cone penetration test results in offshore California silts*, ASTM, Philadelphia (USA).

Randolph M.F., Hope S.N. 2004. Effect of cone velocity on cone resistance and excess pore pressure. Proc. of the Engineering Practive and Performance of Soft Deposits, Osaka (Japan), 147-152.

Robertson, P. K. 1986. Use of piezometer cone data, Soil Classification Using the CPT, Proc. ACSE Spec. Conf. In Situ '86, Blacksburg (USA), 1263-1280.

Roscoe K.H., Schofield A.N., Wroth C.P. 1958. On Yielding of Soils, *Geotechnique*, **8**(1), 22-53.

Schofield A.N., Wroth C.P. 1968. *Critical State Soil Mechanics*, McGraw-Hill, London (UK).

Seed H.B., Tokimatsu K., Harder L.F., Chung R.M. 1985. Influence of SPT procedures in soil liquefaction resistance evaluations, *Journal of Geotechnical Engineering*, **111**(12), 1425-45.

Shuttle D.A., Cunning J. 2007. Liquefaction potential of silts from CPTu, *Canadian Geotechnical Journal*, **44**(1), 1-19.

Silva M.F, White J.W., Bolton M.D. 2006. An analytical study of the effect of penetration rate on piezocone tests in clay, *International Journal for Numerical and Analytical Methods in Geomechanics*, **30**(6), 501-527.

Yu H.S. 2000. *Cavity expansion methods in geomechanics*, Kluwer Academic Publishers, Dordrecht (NL).

Yu H.S., Mitchell J.K. 1998. Analysis of cone resistance: Review of methods, *Journal of Geotechnical and Geoenvironmental Engineering*, **124**(2), 140-149.

PAPER V

LeBlanc, C., Ibsen, L. B. & Liingaard, M.

Buckling of large diameter bucket foundations during installation in sand

Submitted for publication.

The first monopod bucket foundation, the Mobile Met Mast, to be installed offshore, Denmark, 2009

Buckling of large diameter bucket foundations during installation in sand

Christian LeBlanc[1], Lars B. Ibsen[2], Morten Liingaard[3]

1) Ph.D. research student, Dept. of Civil Engineering, Aalborg University & Dept. of Offshore Technology, DONG Energy, A. C. Meyers Vænge 9, DK 2450 Copenhagen SV, Denmark. Phone: (+45) 9955 2558. E-mail: chrle@dongenergy.dk
2) Professor, Dept. of Civil Engineering, Aalborg University, Sohngårdsholmsvej 57, DK 9000 Aalborg, Denmark
3) Geotechnical Engineer, Dept. of Offshore Technology, DONG Energy, A. C. Meyers Vænge 9, DK 2450 Copenhagen SV, Denmark

Date written: 16.03.2009

Date revised: -

Number of words: 4926

Number of pages: 26

Number of figures: 18

Number of tables: 2

Abstract

The bucket foundation may be a cost-effective support structure for future offshore wind farms. The bucket foundation is a thin shell structure and is therefore particularly exposed to structural buckling, due predominantly to the hydrostatic loading during suction installation. This paper addresses the hydrostatic buckling pressure of large diameter bucket foundations during installation in sand. The results presented are derived from three-dimensional, non-linear finite element analyses, taking into account material plasticity, residual stresses, geometric imperfections, embedment depth and derived effects of adding suction, such as the presence of hydraulic gradients in the soil. Guidelines for determining appropriate boundary conditions are suggested, based on the numerical findings. The guidelines were confirmed by observations from a full-scale bucket foundation, which failed due to buckling in 2005. The results and conclusions presented were used successfully to design the first bucket foundation, the Mobile Met Mast, which was installed offshore in Denmark in 2009.

Number of words: 150

Keywords: Buckling strength, Geometric imperfections, Foundation installation, Suction caisson, Sand, Offshore installation

1. Introduction

Wind power currently offers a very competitive source of renewable energy, and therefore the market for offshore wind farms is projected to expand rapidly within the next decade. Several foundation concepts for offshore wind turbines exist. Offshore wind turbine foundations are moment resistant structures, primarily governed by large moments at seabed level, and comparably small horizontal and vertical loads. The most current offshore wind turbine foundations are "monopiles" which are stiff piles with large diameters, 4-6 m, driven 15-30 m into the seabed. The monopile belongs to the family of monopod foundations; foundations having a single interface to the soil.

The bucket foundation, also referred to as "suction caisson", is a large cylindrical monopod foundation, typically made of steel (Fig. 1). Depending on the skirt length and diameter, the bucket foundation has a moment resistance equivalent to a monopile, a gravity foundation or in between. The bucket foundation has the potential to be a cost-effective option in certain soil conditions. A bucket foundation typically requires less steel compared to a monopile, but fabrication costs are slightly higher due to the complicated lid structure. However, the total cost, steel and fabrication, of a bucket foundation is likely to be less than that of a monopile. A bucket foundation can be installed using suction assisted penetration whereby suction is applied within the bucket subsequent to an initial self-weight penetration. The suction creates a pressure differential across the bucket lid, effectively increasing the downward force on the bucket while reducing the skirt tip resistance. Suction assisted penetration has the potential to reduce installation costs significantly, as large jack-ups, driving and drilling equipment are avoided. Natural obstructions, such as cobbles or boulders may prevent

suction installation, thus the bucket foundation is applicable only in certain soil conditions, such as fine sands and clay materials. Presently, a single wind turbine has been installed on a bucket foundation in Frederikshavn, Denmark [1].

The suction installation technology was originally introduced by Shell [2] and is currently widely used for suction anchor piles and skirted foundations within the offshore oil and gas industry. The suction installation technology has been successfully applied to different types of structures installed in a variety of soils, for example the Europipe and Sleipner jackets which were the first major structures using suction caissons to be installed in sand [3,4]. Compared to oil and gas jackets, bucket foundations offer less self-weight to assist penetration and installation sites are predominantly in shallow waters, <30 m. Failure during suction assisted installation results from the formation of local piping channels, which occurs when the applied suction increases and causes an upward flow, reducing the effective stresses within the caisson, and eventually liquefying parts of the internal soil matrix. Local piping channels break down the hydraulic seal, thus preventing further installation. Simplified equations addressing the suction limits, with respect to piping in homogeneous soil are given by Houlsby at al. [5,6].

The cost efficiency of a bucket foundation is significantly improved by increasing the ratio of skirt length L over diameter D to approximately $L/D \approx 1$, while the wall thickness t_S is kept at a minimum. The dimensions are defined in Fig. 2a. The geometry of bucket foundation falls into the category of thin shell structures, as the aspect ratio between the bucket diameter and wall thickness is very large ($D/t_s > 500$). The

structure is therefore particularly exposed to structural buckling due predominantly to the hydrostatic loading during installation. Buckling is therefore a major design consideration. The buckling failure loads are influenced by several factors, such as residual stresses, material plasticity and lid stiffness, and in particular geometric imperfections of the bucket skirt. During installation the bucket skirt becomes partly embedded. The lateral restraints offered by the sand to the embedded skirt may increase the buckling loads significantly, however, the degree of restraint is difficult to determine.

A crucial case of buckling occurred in Wilhelmshaven, Germany, in 2005. A large bucket foundation, with a skirt length of 15 m and a diameter of 16 m, was constructed to support a 6 MW Enercon OWT. The bucket foundation was attempted to be installed offshore, using a combination of suction and skirt tip injection. However, due to a horizontal impact from the installation vessel as the skirt had penetrated 6.8 m into the soil, the bucket foundation buckled and the installation failed completely. Post-failure images of the bucket foundation are shown in Fig. 3. This failure clearly underlines the exposure of bucket foundations to buckling and the importance of detailed analyses of buckling in the design phase.

Structural buckling is significant risk of failure during installation and should be addressed. In this paper, the risk of structural buckling is addressed using numerical methods to determine the hydrostatic buckling pressures of large diameter bucket foundations during installation in sand. The results presented were derived from three-dimensional, non-linear finite element analysis. Theoretically, if all features of a bucket

foundation are incorporated in a finite element model, it should be possible to numerically determine the buckling pressure with a high accuracy. However, this is probably an unrealistic goal, as uncertainties arise due to inadequate knowledge of the as-built features of a bucket foundation. If the most important features are incorporated in a finite element analysis, lower thresholds for buckling pressures may be numerically determined with a reasonable accuracy. In this paper, true representations of the as-built structure, as far as the measured data allow, were included in the finite element analysis. The results of the finite element analysis are compared with theoretical expressions and current standards for evaluating buckling loads and a simple method to predict the buckling loads of bucket foundations during embedment in sand is proposed. The validity of the method is supported by observations from a full-scale bucket foundation, which failed due to buckling during installation.

All results presented in this paper are based on two steel bucket foundations, A and B, with geometries comparable to full-scale bucket foundations supporting offshore wind turbines in the range 2-3 MW. Thus, the validity of the presented results is limited to bucket foundations with dimensions comparable to those of buckets A and B, listed in Table 1.

2. Elastic buckling of perfect cylindrical shells

Buckling of cylindrical shells due to hydrostatic pressure is highly dependent on the applied boundary conditions at both ends. The boundary conditions may be described as free (F), pinned (P) or clamped (C). A pinned boundary has the lateral and

circumferential displacement components constrained, that is, $v = w = 0$ (Fig. 2b). A clamped boundary has all displacement and rotational components constrained.

The hydrostatic buckling pressure of a perfect pinned-pinned (PP) cylinder, a cylinder having a pinned support at each end of the skirt, may be evaluated by the classic expression:

$$P_{PP}^{0} = \frac{\pi^2 E_c t_s^3}{12(1-\nu_c^2)L^2 R} P_{PP}^{*} \tag{1}$$

in which R is the radius of the caisson, E_c is the modulus of elasticity and ν_c is the Poisson's ratio [7]. The load P_{PP}^{*} refers to the non-dimensional buckling pressure and may for intermediate length cylindrical shells, such as bucket foundations, be evaluated using:

$$P_{PP}^{*} = 2\sqrt{\frac{8Z}{3\pi^2}} \tag{2}$$

in which the parameter Z refers to the Batdorf parameter, conveniently used to classify the geometry of a cylindrical shell:

$$Z = \frac{L^2}{R t_s}\sqrt{1-\nu_c^2} \tag{3}$$

The boundary conditions (F), (P) and (C) may occur in various combinations, depending on the restraint at each end of the skirt. In elastic buckling, the buckling pressures for each combination of boundary conditions may be evaluated in terms of the PP buckling pressure by $P^0 = \alpha_b P_{PP}^0$, in which α_b is a multiplier [7]. Values of α_b for various combinations of boundary conditions and their corresponding buckling modes are shown in Fig. 4.

3. Current methodology

It is not uncommon that the experimental buckling loads are as low as 30% of the theoretical value for cylindrical shells. The reason for this discrepancy can be attributed to load eccentricities, residual stresses in the fabricated structures and geometric imperfections. Over the last decades, much research has been carried out to investigate the imperfection sensitivity of shell buckling. A comprehensive review of advances and trends within the theory of thin-shell buckling is provided by Teng [8].

The methods recommended by currents standards are considered as semi-empirical due to the lack of agreement between theoretical and experimental buckling loads. The recommendations by DNV [9] employ a methodology equivalent to Eq. 1 and Eq. 2 for cylinders with PP boundary conditions and material yielding is also taken into account. Furthermore, a semi-empirical multiplier is introduced to reduce the buckling loads according to empirical observations. The recommendations are based on an assumed level of imperfections, thus it may be beneficial to perform more refined analyses, taking into account the real boundary conditions and actual geometric imperfections.

4. Analysis with idealized boundary conditions

Although the main objective of this work was to determine the buckling pressure of bucket foundations during installation in sand, series of generic finite element analysis of buckets with idealized boundary conditions were carried out to understand and quantify the effects of various factors.

4.1 Finite element model

The results were derived from three-dimensional, non-linear, finite element analysis conducted using the commercial finite element package, ABAQUS, which provides flexibility in terms of mesh generation, elements types, material models and non-linear solvers [10]. The bucket foundations were modelled using 8-node second-order shell elements with the properties, $E_c = 210$ GPa, $v_c = 0.29$, $\sigma_y = 235$ MPa, and initial convergence studies were conducted to determine the required refinement of the bucket mesh. In each simulation, a uniformly distributed hydrostatic pressure was applied to the bucket foundation and a non-linear incremental post-buckling analysis was performed using the modified Rik's method, capable of predicting the unstable, geometrically nonlinear collapse of structures. The hydrostatic buckling pressure was determined as the point where either a) yielding occurred in the steel or b) instability occurred and the bucket collapsed elastically.

4.2 Geometric imperfections

The fabrication process of a bucket foundation causes significant geometric imperfections of the bucket skirt due to the welding and plate bending. The geometric imperfections of the bucket skirt reduce the buckling load significantly. The imperfections may vary in both geometry and size. The magnitude of the imperfections may be measured in fractions of skirt thickness, that is, the imperfection $w^* = 1$ corresponds to diameter fluctuations in the order of the skirt thickness, t_s, as defined in Fig. 2c. The magnitude of the imperfections may range realistically from $w^* \approx 1$, near the lid, to severe imperfections in the order of $w^* \approx 5$, near the free skirt.

The effect of geometric skirt imperfections was investigated numerically by distorting the perfectly shaped bucket-mesh prior to performing the non-linear incremental buckling analysis. The applied geometric imperfections were generated on the basis of the deformation pattern obtained from either a) measurements of a full-scale bucket foundation or b) the lowest pre-buckling eigenmode, obtained by solving the corresponding linear eigenvalue buckling problem. For hydrostatically loaded shells, initial geometric imperfections in the form of the lowest pre-buckling eigenmode were found to provide the greatest reduction in buckling load [11]. Therefore, in the following, "eigenmode imperfections" refer to the geometric imperfections generated from the deformation pattern of the lowest pre-buckling eigenmode.

Results illustrating the sensitivity to eigenmode imperfections are shown in Fig. 5. The results are normalized with respect to the theoretical buckling pressure of perfect cylinders (Eq. 1), 123 kPa and 169 kPa for bucket A and B, respectively. The buckling pressures decay rapidly as the magnitude of imperfections increases. The buckling pressure may be expressed by:

$$P_{PP}^{w^*} = \alpha_i P_{PP}^0 \tag{4}$$

in which α_i is a multiplier, accounting for imperfections. For both buckets, the recommendations by DNV [9] are equivalent to $\alpha_i \approx 0.4$, corresponding to imperfections in the order of $w^* \approx 3.5$. For higher degrees of imperfections, the recommendations may be non-conservative. It should be noted that other factors affecting the hydrostatic buckling pressure, such as residual stresses, are also included in the recommendations by DNV [9].

The geometry of realistic imperfections may differ significantly from the eigenmode imperfections. A bucket foundation, referred to as the "Mobile Met Mast", was designed as a support structure for a met mast and constructed in 2008 in Aalborg, Denmark. The dimensions of the bucket foundation were equivalent to bucket A. After construction, the actual geometry of the bucket foundation was measured precisely by means of laser scanning to obtain a three-dimensional point cloud as illustrated in Fig. 6. The magnitudes of the geometric skirt imperfections were evaluated from the three-dimensional point cloud (Fig. 7). The largest imperfections were found near the weldings, with increasing magnitude towards the bottom of the skirt. The average and maximum imperfections were $w^* = 0.7$ and $w^* = 5.6$, respectively.

The hydrostatic buckling pressure of the bucket foundation was determined numerically and compared to results obtained for eigenmode imperfections (Fig. 8). The results indicate that the severity of the measured imperfections are comparable to eigenmode imperfections in the order of $w^* \approx 0.5$. Thus, it seems very conservative to determine the buckling pressure using Fig. 5 in conjunction with the maximum measured imperfection, $w^* = 5.6$. It seems more appropriate to use the average size of imperfections, $w^* = 0.7$, however, this may not hold true for other bucket foundations. For example, if the weldings are located near the ripples formed by the lowest eigenmode, then the geometric imperfections are likely to be more severe. It is recommended that the number and position of weldings be considered in the design phase in order to avoid geometric imperfections which are close to the eigenmode imperfections.

4.3 Residual stresses

Whereas geometric imperfections are known to have a profound effect on the buckling pressure, residual stresses may also have a significant effect. The process of fabricating the bucket skirt, by rolling and welding, results in permanent plastic deformations of some of the material. This causes a pattern of residual stresses to be locked in the bucket skirt plates which affects the subsequent response of the structure. The residual stresses, however, are difficult to measure but may be approximated numerically [12]. In either case, true representations of the as-built structures in a finite element model are not possible.

In this paper, the effect of residual stresses is estimated roughly. Assuming that the magnitudes of the initial residual stresses are $0.33 \times \sigma_y$, the effect of residual stresses may be approximated by determining the hydrostatic buckling pressure as the point when either a) the von Mises stress $(1 - 0.33) \times \sigma_y$ is reached in the steel or b) instability occurs. In analyses in which eigenmode imperfections were used to define the geometry, the residual stresses were found to reduce the buckling pressure by 0.5% for $w^* = 0.25$ and 16% for $w^* = 2$. If the measured imperfections were used in the analysis, the residual stresses were found to reduce the buckling pressure by 10%.

The buckling pressure of bucket A was determined as 86 kPa, taking into account the measured imperfections and the assumed level of residual stresses. For comparison, DNV [9] recommends a buckling pressure of 49 kPa which, in comparison to 86 kPa, is conservatively lower. This suggests that a safety factor of up to 1.75 may be included in

DNV's recommendations and that it may be appropriate to perform refined analyses and testing to determine the buckling pressure of bucket foundations more accurately.

In the following analyses, residual stresses are not taken into account and the applied imperfections are generated using eigenmode imperfections with the magnitude $w^* = 2$.

4.4 Lid stiffness

The lid of a bucket foundation is typically constructed as a large braced steel structure, capable of transferring moments from pile to skirt. The lid provides a boundary support to the skirt, ranging between pinned and clamped. The change in boundary conditions, from PP to CP, provides a 22% increase in buckling pressures for elastic buckling (from PF to CF, the increase is much higher). This increase is lower if geometric imperfections and material plasticity are taken into account. Fig. 9 illustrates the buckling pressure as a function of the thickness of a homogenous lid plate. The results indicate that a clamped support yields an increase in buckling loads of 9-11% and the transition from PP to CP support occurs gradually over the range $t_L/t_S = 10 - 25$. For bucket B, a clamped support of the skirt from the lid requires a stiffness equivalent to a massive 0.75 m lid plate. Thus, the stiffness of a typical braced lid is most likely not sufficient to ensure a clamped support of the skirt.

Buckling loads less than $P_{PP}^{w^*=2}$ were found for $t_L/t_S < 10$, indicating that the lid support was weaker than a pinned boundary condition. The low buckling pressure resulted from large downward displacements in the centre of the lid, causing plastic

deformations and lateral displacements ($w \neq 0$) at the skirt/lid intersection. However, this type of lid bending would not occur if a braced lid structure was modelled.

In general, it may be recommended that the degree of support offered by the lid of a bucket foundation is considered pinned until refined analyses, incorporating the actual lid geometry, are performed. If a clamped support is desired, then the lid stiffness is increased optimally by adding steel along the circumference of the lid, as the lid deformations occur near the skirt in the PP mode (Fig. 10).

5. Analysis of buckling during embedment in sand

While installing a bucket foundation, the skirt becomes partly embedded into the seabed. The seabed soil provides lateral restraints to the embedded skirt, causing the buckling pressure of the bucket to increase. The effect of lateral restraints offered by clay soils on buckling loads was investigated by [13,14]. In general, they suggest that lateral soil restraint be neglected. In this paper, the effect of the lateral restraint offered by sands on the hydrostatic buckling pressures is analysed.

The skirts of bucket A and B were embedded in a circular soil domain modelled using 20-node second-order solid elements (Fig. 11). The strength of the sand was assumed to be governed by effective stresses. As the duration of buckling is short, undrained behaviour of the soil may prevail, thus an effective stress approach is conservative for dilatant sands as lack of drainage increases the soil strength. However, in very loose sands, that is sands showing compressible behaviour, this approach is non-conservative. The constitutive behaviour of the sand was modelled linearly elastic in combination

with a Mohr-Coulumb yield surface. The interface between the bucket skirt and the soil was modelled as Coulomb sliding, with an angle of friction of 20^0. The initial stress conditions were determined from the effective unit weight γ' and the geostatic stress ratio $K_0 = 0.5$. Two types of sand, representative of a loose and a dense sand, were used in the analyses. The sand parameters, chosen conservatively, are listed in Table 2.

In some numerical simulations, the application of hydrostatic pressure caused the bucket to penetrate further into the soil rather than buckle. Therefore, in order to determine the buckling pressure, it was necessary to apply a distributed vertical load along the edge of the embedded skirt to counter-balance the downward force acting on the bucket foundation.

5.1 Critical geometric imperfections during embedment

The deformation pattern of the lowest pre-buckling eigenmode, determined by solving the corresponding linear eigenvalue buckling problem, does not provide the most critical geometric imperfections if the bucket foundation is embedded in sand. Geometric imperfections that are more critical can be calculated using the reduced soil stiffness modulus, E_{evp}, in the linear eigenvalue buckling problem. Geometric imperfections for $E_{evp} < E$ have deformation patterns stretching deeper into the soil. Fig. 12 illustrates the buckling pressure of bucket A, embedded 3 m in loose sand, calculated using different eigenmode imperfections, with magnitude $w^* = 2$, obtained for various values of E_{evp}. The greatest reduction of buckling pressure, 10%, was obtained for $E_{evp} = 0.1 \times E$. In all further analyses, the critical geometric imperfections were generated using a reduced soil stiffness modulus in the linear eigenvalue problem.

The sensitivity of an embedded bucket foundation to geometric imperfections was evaluated and compared to the sensitivity of a bucket with PP boundary conditions. The results are shown in Fig. 13. The almost coinciding curves indicate that the buckets were equally exposed to geometric imperfections, and a sensitivity analysis of imperfections may be based on the simple PP boundary case.

5.2 Equivalent pinned embedment depth

During installation of a bucket foundation, the degree of skirt fixation increases. The degree of skirt fixation may be evaluated in terms of the equivalent pinned embedment depth, h_{PP}, the depth below seabed where the support from the embedded skirt equilibrates a pinned boundary in respect to buckling (Fig. 14). The introduction of L_{PP} allows the hydrostatic buckling pressure as a function of embedment depth to be determined using Eq. 1-4 if h_{PP} and an appropriate value of α_i are known.

In this paper, representative values of h_{PP} are predicted numerically. Firstly, the hydrostatic buckling pressure $P_{cr}^{w^*}$ of bucket A and B was determined at the embedment depths h/L, of 0.25, 0.50 and 0.75. Secondly, the corresponding values of L_{PP} were determined from Eq. 1, using the condition $P_{PP}^{w^*} = P_{cr}^{w^*}$. Finally, h_{PP} was calculated from L_{PP} and h. Fig. 15 shows the normalized values of h_{PP} predicted in the analyses.

The results show that the value of h_{PP} depends on both sand properties and embedment depth. For bucket A and B, the value of h_{PP} was determined to be in the ranges $0.6 - 1.3$ m and $0.8 - 3.7$ m, respectively, and when the bucket foundation was

installed in loose sand rather than dense sand, the value of h_{PP} increased by $0.3 - 1.1$ m. The equivalent pinned embedment depth may be approximated conveniently by the linear expression $h_{PP} = c \times h + 0.1 \times L$, in which c is in the range $0.1 - 0.23$ for buckets installed in dense sand, and $0.23 - 0.33$ for buckets installed in loose sand.

5.3 Derived effects of adding suction

Applied suction inside the bucket causes a steady-state flow field to evolve in the sand. This yields a constant influx of water which must be pumped out to maintain a constant level of suction within the bucket. If the excess pore pressure applied in the bucket is s, then the excess pore pressure at the skirt tip is as, with the constant, a in the range $0.0 - 1.0$. The value of a depends on the flow field geometry and can be approximated numerically [5]. As the level of suction increases, a limit is reached whereby the upward hydraulic gradient in the bucket exceeds the gravitational force acting on the sand particles. At this limit, the effective stresses vanish and local piping channels are formed. The average vertical pore pressure gradient along the internal bucket skirt may be evaluated by $(1 - a)s/h$, thus the critical level of suction, s_{cr} causing piping may be approximated using:

$$s_{cr} = \frac{h\gamma_0^{'}}{1 - a} \tag{5}$$

in which $\gamma_0^{'}$ is the submerged unit weight of the sand. For suction less than critical, the effective unit weight of the sand, γ' inside the bucket may be approximated using:

$$\gamma' = \gamma_0^{'}\left(1 - \frac{s}{s_{cr}}\right) \tag{6}$$

The reduction of $\gamma^{'}$ will significantly decreases the lateral restraints provided to the embedded skirt by the sand. The effect of suction on buckling pressures was analyzed

numerically by reducing γ' of the soil matrix within the buckets A and B. The results, evaluated in terms of h_{PP}, are shown in Fig. 16. For both loose and dense sand, the effect of suction increased the equivalent pinned embedment depth, by approximately 0.4 m m, i.e. $\Delta h_{PP}^{s} = h_{pp}(s/s_{cr} = 1) - h_{pp}(s/s_{cr} = 0)$ = 0.4 m. This increase may be approximated by a linear function of s/s_{cr}.

5.4 Calculation of P_{cr} during suction installation

On the basis of the numerical findings, it is suggested that bucket foundations with dimensions comparable to buckets A and B may be designed to withstand hydrostatic loading, using Eq. 1-4 and appropriate values of α_i and L_{PP}. The value of L_{PP} is determined by:

$$L_{PP} = L - h + h_{PP} \tag{7}$$

in which h_{PP} may be approximated by:

$$h_{PP} = c \times h + 0.1 \times L + \Delta h_{PP}^{s} \tag{8}$$

to account for the applied suction and embedment depth. c is a dimensionless multiplier introduced to account for the sand properties at the site of installation. Appropriate values of c follows from Fig. 15 and the effect of adding suction may be accounted for by setting $\Delta h_{PP}^{s} = 0.4$ m. It is important to note that these values are only applicable if the bucket dimensions are similar to those of buckets A and B or more slender buckets.

5.5 Comparison to full-scale observations

Observations of the buckling deformation pattern of the bucket foundation in Wilhelmshaven may be used for verification. The buckling of the skirt occurred as the bucket had penetrated 6.8 m in the sand, corresponding to the normalized penetration

depth $h/L = 0.45$. From Fig. 3, it can be seen that the buckling deformation pattern stretched 2.1 m below the seabed. This indicates that the pinned embedment depth was approximately $h_{PP} = 2.1$ m.

Bucket B may be compared to the bucket from Wilhelmshaven, as their dimensions are in the same order of magnitude. At the normalized penetration depth $h/L = 0.45$, the value of h_{PP} for bucket B, using Fig. 15, is predicted to be 2.0 m and 2.8 m for loose and dense sand, respectively. In comparison, the observed value of $h_{PP} = 2.1$ m is within this range. Thus, the structural buckling that occurred in Wilhelmshaven supports the validity of the numerical findings.

5.6 Design and installation of the Mobile Met Mast

The guidelines presented in this paper were used for design of the Mobile Met Mast. Buckling design curves were calculated on the basis of DNV [9] for a cylinder with PP-boundary conditions. Thereby, it was implicitly assumed that the lid support was equivalent to a pinned support. The equivalent pinned skirt length during embedment, L_{PP}, was calculated from Eq. 7 and 8 for loose ($c = 0.23$) and dense sand ($c = 0.1$). The value $h_{PP}^{s} = 0.4$ m was used in Eq. 8 since the critical level of suction causing piping was predicted to be close to the buckling design curve. Fig. 17 illustrates the buckling design curves for loose and dens sand. The buckling curve for $L = L_{PP}$ is added for comparison. The Mobile Met Mast was designed such that the expected range of required suction was less than the buckling design limit for installation in both loose and dense sand. On basis of the buckling analyses presented in Section 4.3, it was expected that the buckling design curves included a safety factor of up to 1.75.

The Mobile Met Mast was successfully installed at Horns Rev 2 Offshore Wind Farm, Denmark in February 2009, as shown in Fig. 18. During installation, the bucket skirt penetrated both loose and dense sand. The suction required for installation was within the expected range of suction. There were no indications of structural buckling.

6. Conclusions

This paper addresses the risk of hydrostatic buckling of large diameter, thin-walled bucket foundations (suction caissons) during installation in sand. Results were obtained using three-dimensional, non-linear finite element analyses. The results and conclusions presented in this paper were successfully used to design of the first bucket foundation, the Mobile Met Mast, which was installed offshore in Denmark, 2009.

The main conclusions are summarized below:

Geometric imperfections:

- The recommendations by DNV [9] appear to provide a conservative estimate of the buckling pressure for cylinders with PP boundaries and geometric imperfections less than $w^* \approx 3$.
- A three-dimensional laser scanning of a full-scale bucket foundation showed that the largest skirt imperfections were located near the weldings, with increasing magnitude towards the bottom of the skirt. The average and maximum imperfections were $w^* = 0.7$ and $w^* = 5.6$, respectively. It is recommended that the number and position of weldings be considered in the

design phase in order to avoid geometric imperfections which are close to the deformation pattern of the eigenmode imperfections.

- Realistic imperfections can be significantly less severe than eigenmode generated imperfections. Thus, it may be appropriate to measure the as-built imperfections and perform refined numerical analyses to determine the hydrostatic buckling pressure of bucket foundations.

Residual stresses

- Initial residual stresses, one-third of the yield stress reduced the buckling pressure by approximately 10%.

Skirt support from the bucket lid

- It is recommended that the skirt support from the lid of the bucket foundation is assumed pinned unless refined analyses, incorporating the actual lid geometry, are performed. A clamped lid support increased the buckling pressure by approximately 10%.

Skirt support from sand during embedment

- The lateral support provided to an embedded bucket skirt by sand is significant with respect to structural buckling of the skirt. The degree of fixation depends on the bucket properties, sand properties, embedment depth and degree of applied suction. The degree of skirt fixation was expressed in terms of the equivalent pinned embedment depth h_{PP} and appropriate values of h_{PP} were determined numerically. Observations from a bucket foundation in Wilhelmshaven, which failed due to buckling, confirmed the numerical findings.
- The equivalent pinned embedment depth is a function of the applied suction. The effect of adding suction increased the equivalent pinned embedment depth

by up to 0.4 m. This reduction can be approximated by a linear function of s/s_{cr}.

The validity of the guidelines presented is limited to bucket foundations with dimensions comparable to those used in the numerical analyses. Further research should aim at developing design guidelines which are valid for arbitrary bucket dimensions and attempt to verify the main conclusions by physical testing. Furthermore, future research should address the effect of horizontal loading on buckling pressure; when a bucket foundation is installed, an initial seabed footprint is drawn by the free end of the bucket skirt. This footprint is not perfectly circular due to geometric imperfections. During the process of installation, this footprint is forced to alter shape towards the circular shape of the bucket lid. Thus, active soil pressure builds up, resulting in local horizontal loading on the bucket skirt. Horizontal loading may also arise from a vessel impact or from wave and currents.

References

[1] Ibsen LB. Implementation of a new foundation concept for Offshore Wind farms. In: Proc 15th Nordic Geotechnical Meeting. Norway, 2008. p. 19-33.

[2] Senepere D, Auvergne GA. Suction anchor piles – a proven alternative to driving or drilling. In: Proc 14th Offshore Technology Conf. Texas, 1982. p. 483-493.

[3] Tjelta TI. Geotechnical experience from the installation of the Europipe jacket with bucket foundations. In: Proc 27th Offshore Technology Conf. Texas, 1995. p. 897-908.

[4] Erbrich CT, Tjelta TI. Installation of bucket foundations and suction caissons in sand: geotechnical performance. In: Proc Offshore Technology Conf. Texas, 1999. Paper 10990.

[5] Houlsby GT, Byrne BW. Calculation procedures for installation of suction caissons in sand. Proc ICE - Geotechnical Engineering 2005:158(3), 135-144.

[6] Houlsby GT, Kelly RB, Byrne BW. The tensile capacity of suction caissons in sand under rapid loading. In: Proc Int Symp on Frontiers in Offshore Geotechnics. Australia, 2005. p. 405-410.

[7] Pinna R, Ronalds BF. Hydrostatic buckling of shells with various boundary conditions. Jour of Constructional Steel Research 2000;56(1):1-16.

[8] Teng JG. Buckling of thin shells: Recent advances and trends. Applied Mechanics Reviews 1996;49(4):263-274.

[9] DNV-RP-C202 Recommended practice: Buckling strength of shells. Det Norske Veritas. Norway, 2002.

[10] ABAQUS Version 6.7 documentation. Dassault Systèmes. France, 2007.

[11] Guggenberger W. Buckling and post-buckling of imperfect cylindrical shells under external pressure. Thin-Walled Structures 1995;23(1-4):351-366.

[12] Graham D. Predicting the collapse of externally pressurised ring-stiffened cylinders using finite element analysis. Mar Struct 2007;20(4):202–217

[13] Ronalds BF, Pinna R. Eigen buckling of cylindrical shells in offshore structures: Influence of geometry, loading and end conditions. In: Proc Inst of Civ Eng: Structures and Buildings 2003;156(2):183-191.

[14] Pinna R, Martin CM, Ronalds BF. Guidance for design of suction caissons against buckling during installation in clay soils. In: Proc 11th Int Offshore and Polar Engineering Conf. Norway, 2001. p. 662-668.

Notation

The following symbols are used in this paper:

a	dimensionless constant (-);
c	dimensionless multiplier (-);
D	bucket diameter (m);
E	Modulus of elasticity (sand) (kPa);
E_{evp}	Modulus of elasticity (sand) used to solve the linear eigenvalue problem (kPa);
E_c	modulus of elasticity, caisson (kPa);
h	penetration depth (m);
h_{pp}	equivalent pinned embedment depth (m);
L	skirt length (m);
L_{PP}	equivalent pinned skirt length (m);
p	hydrostatic pressure (kPa);
p_{cr}, p^0	hydrostatic buckling pressure (kPa);
$p_{cr}^{w^*}$	hydrostatic buckling pressure for imperfections of magnitude w^* (kPa);
P_{PP}^0	hydrostatic buckling pressure of a perfect and elastic cylinder with PP boundary conditions (kPa);
P_{PP}^*	non-dimensional hydrostatic buckling pressure (-);
$p_{PP}^{w^*}$	hydrostatic buckling pressure of a cylinder with PP boundary conditions and imperfections of magnitude w^* (kPa);

P_{wind}, P_{waves}	environmental loads (kPa);
R	bucket radius (m);
s	applied suction (kPa);
s_{cr}	critical suction (kPa);
t_L	lid thickness (mm);
t_s	skirt thickness (mm);
u	vertical displacement component (-);
w	lateral displacement component (-);
w^*	imperfection parameter (-);
v	circumferential displacement component (-);
Z	Batdorf parameter (-);
α_b, α_i	dimensionless multipliers (-);
$\gamma_0^{'}$	submerged unit weight ($\mathrm{kN/m^3}$);
γ'	effective unit weight ($\mathrm{kN/m^3}$);
ν	Poisson's ratio, sand (-);
ν_c	Poisson's ratio, caisson (-);
ϕ	angle of friction (0);
ψ	angle of dilation (0);
σ_y	von Mises yield stress (kPa);

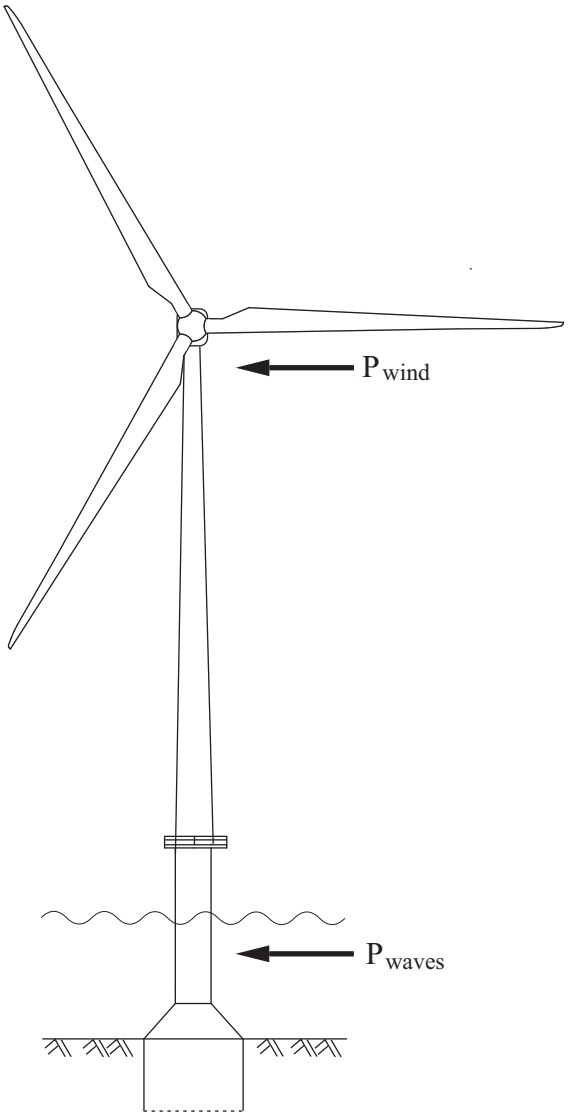

Fig. 1. Offshore wind turbine installed on a bucket foundation.

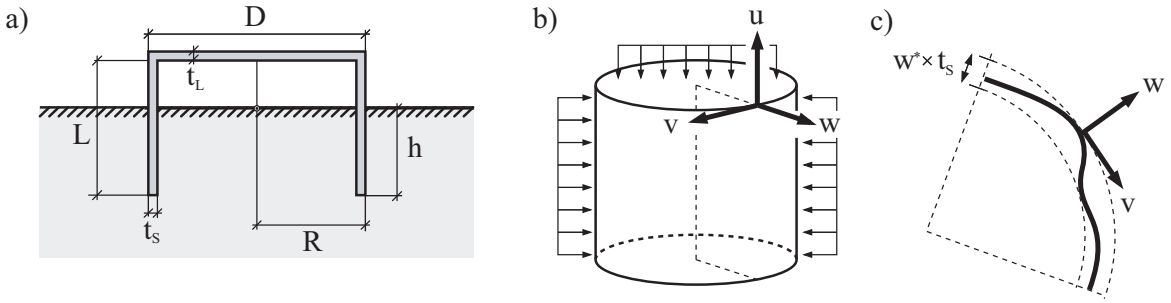

Fig. 2. a) Definition of bucket dimensions. b) Applied load and cylindrical coordinates.

c) Definition of imperfections in terms of $\boldsymbol{w}^*$.

Fig. 3. Buckling failure caused by a vessel impact, Wilhelmshaven, 2005.

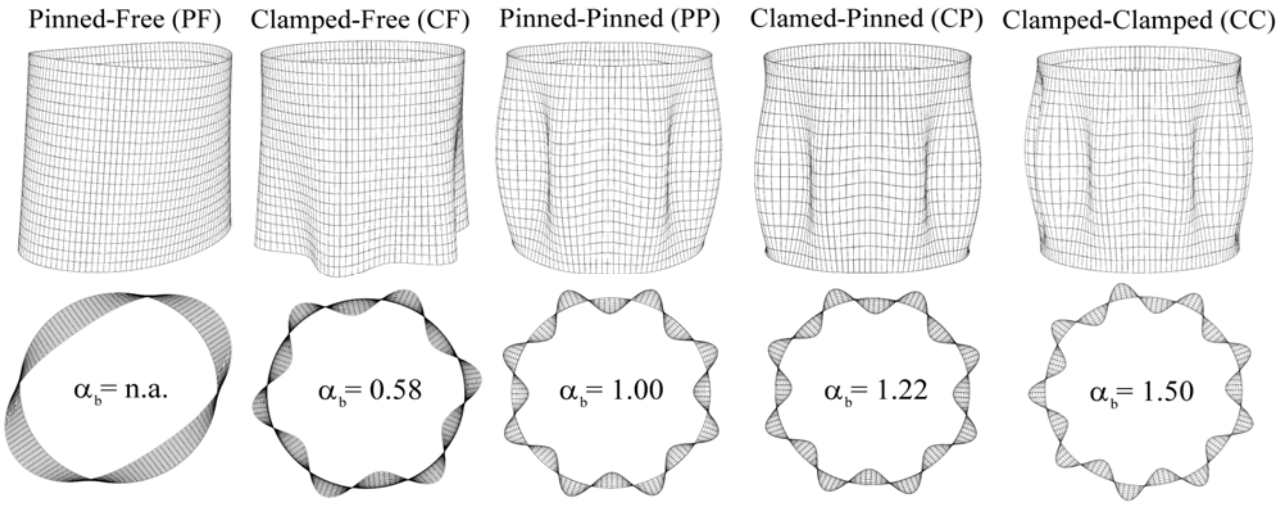

Fig. 4. Buckling modes of cylinders with idealized boundary conditions.

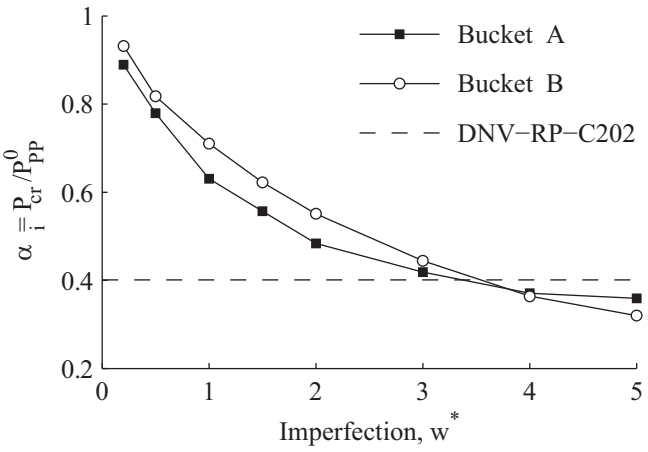

Fig. 5. Buckling pressure as a function of the magnitude of skirt imperfections.

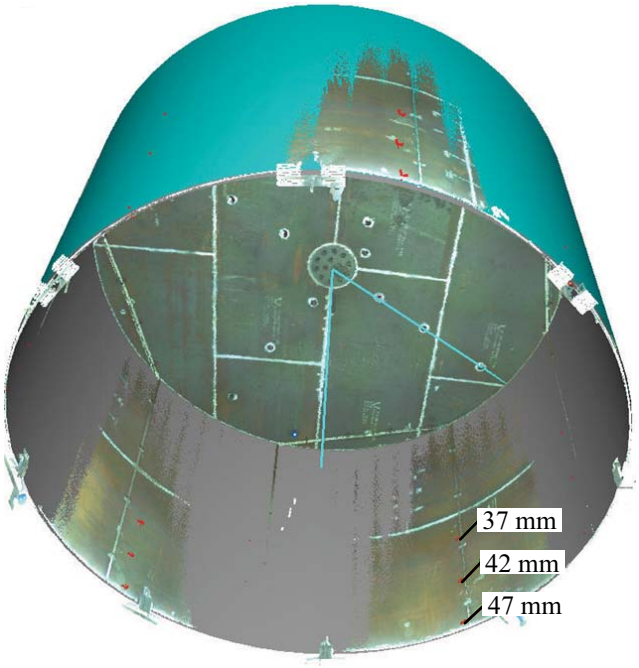

Fig. 6. Visualization of the three-dimensional point cloud obtained by laser scanning of the Mobile Met Mast. Areas of small skirt imperfections ($w^* < 3 \times t_s$) are shaded.

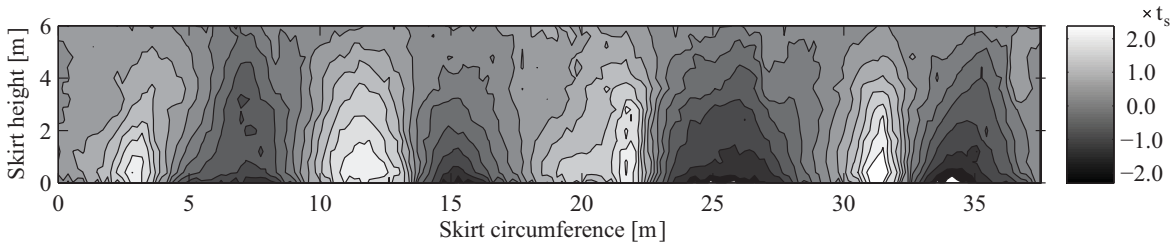

Fig. 7. Skirt imperfections in terms of the wall thickness t_s of the Mobile Met Mast.

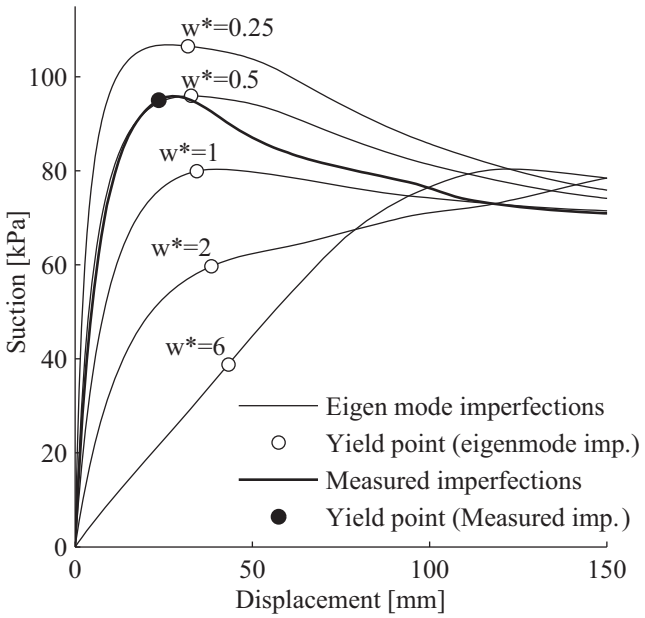

Fig. 8. Skirt deflection as a function of applied suction;

measured imperfections and eigenmode generated imperfections.

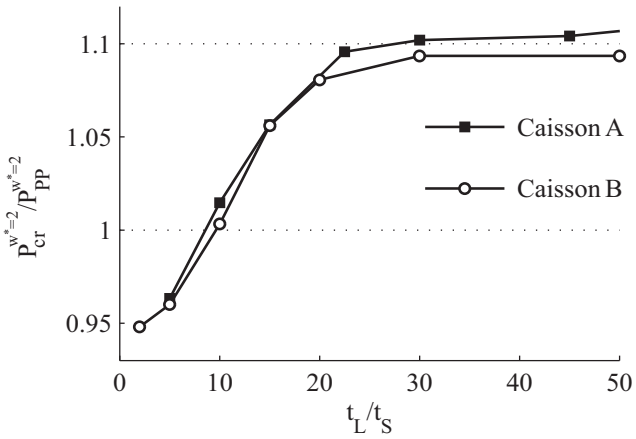

Fig. 9. Buckling pressure as a function of lid thickness.

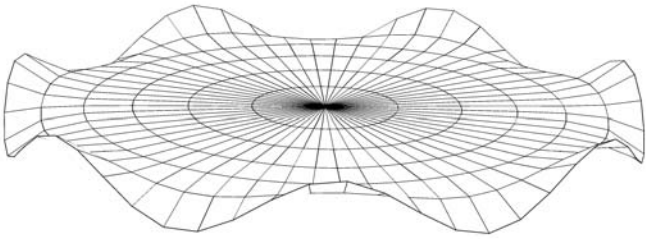

Fig. 10. Lid deformations in the pinned-pinned (PP) mode.

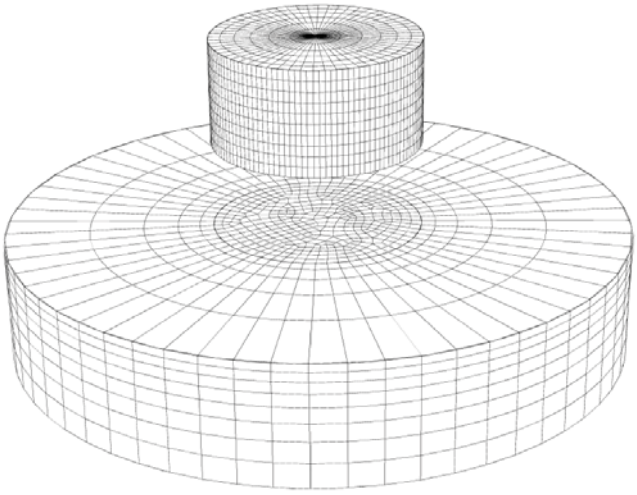

Fig. 11. Mesh of soil and bucket A.

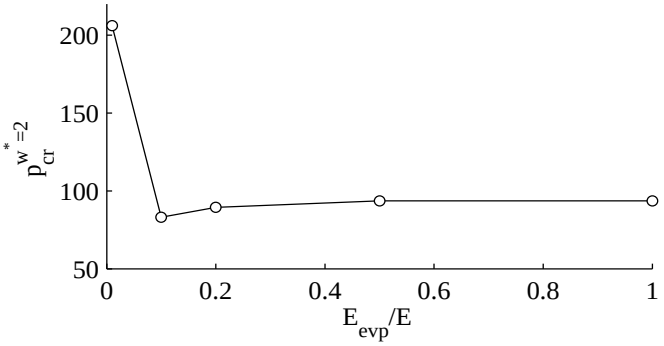

Fig. 12. Buckling pressure of bucket A embedded 3 m in loose sand, calculated using different eigenmode imperfections, magnitude $w^* = 2$.

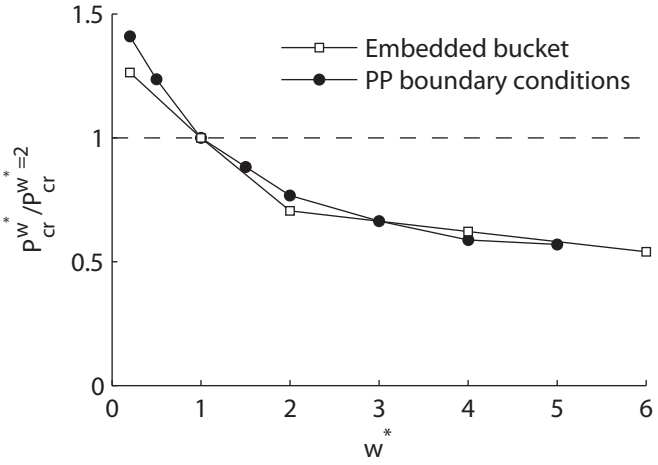

Fig. 13. Sensitivity of buckling pressure to geometric imperfections for

a) 3 m embedment in loose sand, b) PP boundary conditions.

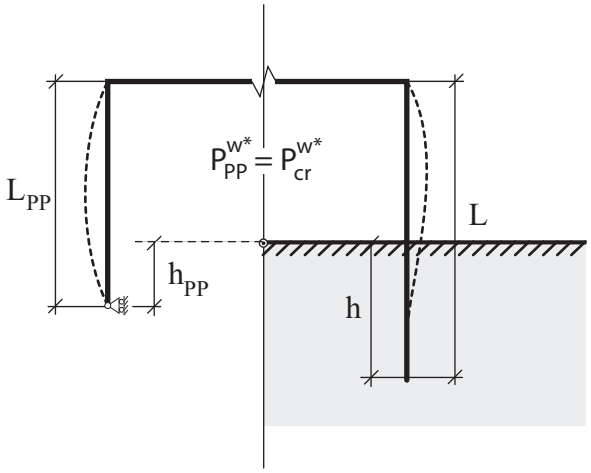

Fig. 14. Illustration of equivalent pinned embedment depth h_{PP} and equivalent pinned skirt length L_{PP}.

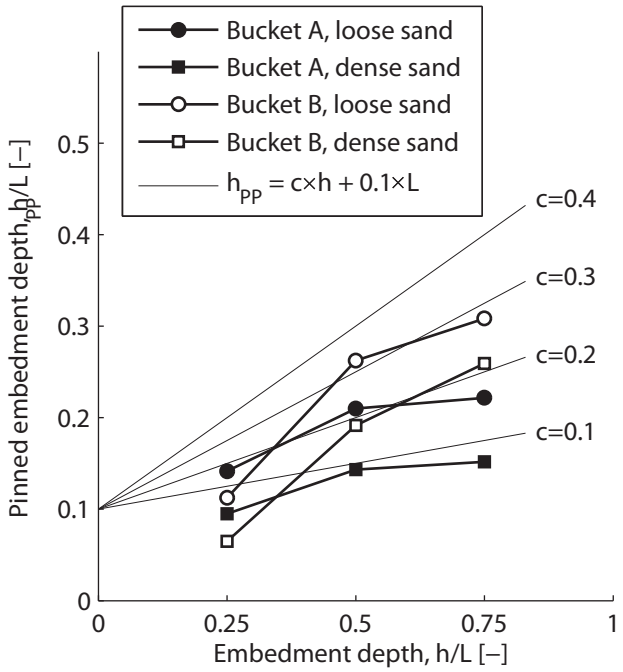

Fig. 15. Pinned embedment depth h_{PP} as a function of embedment depth h, normalised with respect to the skirt length L.

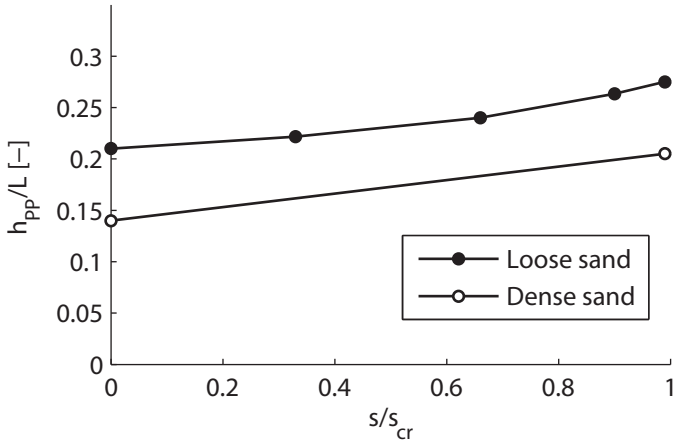

Fig. 16. Pinned embedment depth of bucket A as a function of the suction *s*.

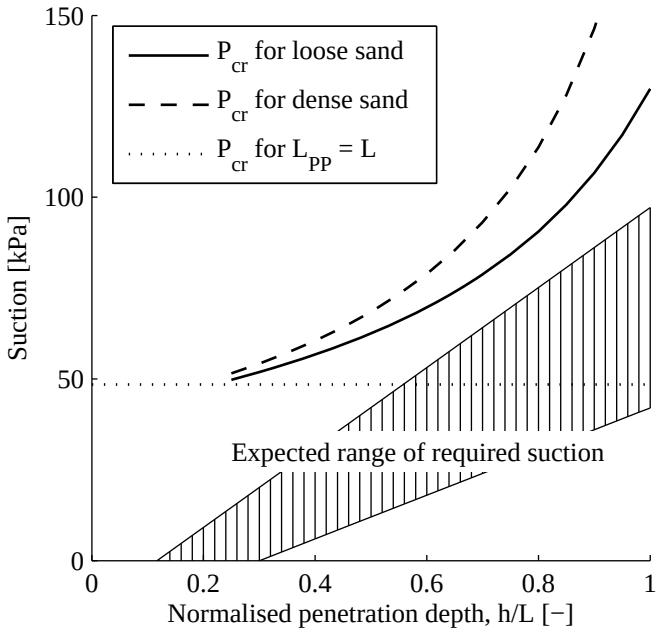

Fig. 17. Buckling design curves for the Mobile Met Mast.

Fig. 18. Successful installation of the Mobile Met Mast

at Horns Rev 2 Offshore Wind Farm, Denmark in 2009.

	L [m]	D [m]	t_s [mm]	t_L [mm]	Z	P_{PP}^0 [kPa]
Bucket A	6	12	20	200	287	123
Bucket B	12	12	30	300	766	169

Table 1. Bucket specifications

	Friction angle ϕ	Elasticity E [MPa]	Dilation angle ψ	Submerged weight $\gamma_0^{'}$ [kN/m^3]
Loose sand	30^0	10	0^0	10
Dense sand	40^0	50	10^0	10

Table 2. Sand parameters